Electro-Thermal Mechanical Modeling of Microbolometer for Reliability Analysis

by

Effa Dawit

A thesis
presented to the University of Waterloo
in fulfilment of the
thesis requirement for the degree of
Master of Applied Science
in
Mechanical Engineering

Waterloo, Ontario, Canada, 2010

I hereby declare that I am the sole author of this thesis. This is a true copy of the thesis, including any required final revisions, as accepted by my examiners.

I understand that my thesis may be made electronically available to the public.

Abstract

Infrared (IR) imaging is a key technology in a variety of military and civilian applications, especially for night vision and remote sensing. Compared with cryogenically cooled IR sensors, uncooled infrared imaging devices have the advantages of being low cost, light weight, and superior reliability. The electro-thermal analysis of a microbolometer pixel is critical to determine both device performance and reliability. To date, most microbolometer analysis research has focused on performance optimization and computation of thermal conductance directly from the geometry. However, modeling of the thermal distribution across the microbolometer pixel is critical for the comprehensive analysis of system performance and reliability. Therefore, this thesis investigates the electro-thermo-mechanical characteristics of a microbolometer pixel considering the effects of joule heating and incoming IR energy.

The contributions of the present research include the electro-thermal models for microbolometer and methods of validating thermal distribution using experimental results. The electro-thermal models explain the effect of microbolometer material properties and geometry on device performance and reliability. The research also contributes methods of estimating the thermal conductivity of microbolometer, which take into account different heat transfer mechanisms, including radiation and convection. Previous approaches for estimating the thermal conductance of uncooled microbolometer consider heat conduction via legs from the geometry of the pixel structure and material properties [2]. This approach assumes linear temperature distribution in the pixel legs structure. It also leaves out the various electro-thermal effects existing for multilayer structures. In the present research, a different approach is used to develop the thermal conductance of microbolometer pixel structure. The temperature distribution in the pixel is computed from an electro-thermal model. Then, the average temperature in the pixel microplate and the total heat energy generated by joule heating is utilized to compute the thermal conductance of the structure.

The thesis discusses electro-thermal and thermo-mechanical modeling, simulation and testing of Polysilicon Multi-User MEMS Process (PolyMUMPs®) test devices as the groundwork for the

investigation of microbolometer performance and reliability in space applications. An electro-thermal analytical and numerical model was developed to predict the temperature distribution across the microbolometer pixel by solving the second order differential heat equation. To provide a qualitative insight of the effect of different parameters in the thermal distribution, including material properties and device geometry, first an explicit formulation for the solution of the electro-thermal coupling is obtained using the analytical method. In addition, the electro-thermal model, which accounts for the effect of IR energy and radiation heat transfer, spreading resistance and transient conditions, was studied using numerical methods.

In addition, an analytical model has been developed to compute the IR absorption coefficient of a Thin Single Stage (TSS) microbolometer pixel. The simulation result of this model was used to compute absorbed IR energy for the numerical model. Subsequently, the temperature distribution calculated from the analytical model is used to obtain the deflections that the structure undergoes, which will be fundamental for the reliability analysis of the device. Finite element analysis (FEA) has been simulated for the selected device using commercial software, ANSYS® multiphysics. Finite element simulation shows that the electro-thermal models predict the temperature distribution across a microbolometer pixel at steady-state conditions within 2.3% difference from the analytical model. The analytical and numerical models are also simulated and results for a temperature distribution within 1.6% difference. In addition, to validate the analytical and numerical electro-thermal and thermo-mechanical models, a PolyMUMPs® test device has been used. The test results showed a close agreement with the FEM simulation deflection of the test device.

Acknowledgements

First, I would like to express my sincere appreciation to my advisor Prof. Patricia Nieva for her advice and support throughout my MASc study. Her introducing me to MEMS and microsystems, the experience and the knowledge she passed on to me goes well beyond this thesis. It was always a pleasure for me to be a member of the Sensors and Integrated Microsystems Laboratory (SIMSLAB) under her supervision. I would also like to thank Dr. Nezih Topaloglu for allowing me to spend time with him on a range of projects related to this thesis and for developing the design prototypes.

I thank my colleagues in the SIMSLAB for their help and companionship. I would also like to thank Canadian Space Agency (CSA) members for supporting this work and providing us with the necessary material and feedback for this work.

I would like to express my gratitude to Page Burton and Mr. Andrew Zwart for their invaluable help with the editing of this Thesis. I would also like to thank Prof. Richard Culham and Prof. Eihab Abdel-Rahman for accepting being the readers of my Thesis.

Last but not least, I would like to very specially thank my wife, Seble Effa, for her patience, support, help and encouragement during the course of my work.

Table of Contents

Chapter Three

Chapter Four

Chapter Five

Chapter Six

List of Tables

List of Figures

Nomenclature

Symbol	Unit	Quantity Description
A_c	m^2	Total microbolometer leg cross-sectional area
A_s	m^2	Element Type equation here.surface area
A_{VOx}	m^2	Cross-sectional area of vanadium oxide (VO_x) layers
A_{Si3N4}	m^2	Cross-sectional area of silicon nitride (Si_3N_4) layers
B_i	-	Biot number
C	J/kg . K	Specific heat capacity
C_{total}	J/kg	Total pixel thermal capacitance
E		Emittance
E	MPa	Young's modulus
E_{em}	J	Electromagnetic Energy
F	-	F-number
F_i	N	Applied Force
F_{no}	-	Number of optics
G	m/s^2	Gravitational acceleration
G	W/K	Thermal conductance
$G_{conduction}$	W/K	Thermal conductance of the microbolometer due to conduction via the legs
$G_{radiation}$	W/K	Thermal conductance of the microbolometer due to radiation
$G_{air\_conductio}$	W/K	Thermal conductance of the microbolometer due to conduction via air
$G_{convection}$	W/K	Thermal conductance of the microbolometer due to convection
G_{total}	W/K	Total pixel thermal conductance
h	W/ m^2 . K	Convective heat coefficient
h_c	W/ m^2 . K	Contact conductance
I	W/m^2	Intensity
I_{app}	A	Applied electric current
j	A/m^2	Current density
j_V	A/m^2	Current density in vanadium layer
j_{VOx}	A/m^2	Current density in vanadium oxide layer
j_{Si3N4}	A/m^2	Current density in silicon nitride layer

k	W/K. m	Thermal conductivity
k_{air}	W/K. m	Thermal conductivity of air
k_{Al}	W/K. m	Thermal conductivity of Aluminums
k_S	W/K. m	Thermal conductivity of substrate (silicon)
k_{bottom}	W/K. m	Effective thermal conductivity between the microplate and substrate
k_{eff}		Effective thermal conductivity of the multilayered structure
k_i	-	Propagation constant
L_c	μm	Microbolometer microplate length
L_l	μm	Microbolometer leg length
m	Kg	Mass
M	W/m^2	Exitance
M_i	N. m	Applied moment
NA	-	Numerical Aperture
P_{abs}	W/m^3	Absorbed IR radiation power per unit volume
P_{Signal}	W/m^3	The incident IR power per unit volume
P_o	W/m^3	The incident peak IR power per unit volume
Q_{IR}	W	Total IR energy absorbed in the element
q_{JH}	W/m^3	Rate of joule heating energy generated per volume
Q_{JH}	W	Rate of joule heating energy generated in the element
Q_{St}	W	Rate of energy change (stored/removed) within a control volume
Q_{cond_leg}	W	Rate of energy transfer via microbolometer leg
Q_{cond_air}	W	Conduction of heat energy via air to the substrate
Q_{cov}	W	Free convection of heat energy to the surrounding atmosphere
Q_{rad}	W	Rate of heat energy radiation from the control volume to the surrounding atmosphere
Q_{Si3N4}	W	Heat energy conducted via silicon nitride layer
Q_{total}	W	Total heat generated or absorbed in the element
Q_{VOx}	W	Heat energy conducted via vanadium oxide layer
R_s	K / W	Spreading resistance
R_{eff}	m. K/W	Thermal resistivity of the multilayer structure
R_{Si3N4}	m. K/W	Thermal resistivity of silicon nitride
R_{vox}	m. K/W	Thermal resistivity of vanadium oxide

S	M	Shape factor for two dimensional conduction
t	S	Time
t_c	-	Transmission coefficient
t_{Al}	μm	Aluminum thickness
t_{air}	μm	Air gap between the microplate and substrate
t_p	μm	Microplate thickness
t_s	μm	Substrate thickness
T	K	Temperature
$T_{ambient}$	K	Environment temperature
T_{avg}	K	Area-averaged microplate temperature change at steady-state
T_s	K	Substrate temperature
T_{Sur}	K	Microbolometer surface temperature
V_{app}	V	Bias voltage
V_{ele}	μm^3	Volume of the differential elements
V_f	V	1/f Noise Voltage
V_j	V	Johnson Noise Voltage
V_n	V	Noise Voltage
w_p	μm	Microplate width
w_l	μm	Leg width
w_{Si3N4}	μm	Width of the silicon nitride
w_{VOx}	μm	Width of the vanadium oxide

List of Symbols

Symbol	Unit	Quantity
α_{VOx}	K^{-1}	Temperature coefficient of resistance (TCR) of vanadium oxide
α_T	m^2/sec	Thermal diffusivity
α_i	K^{-1}	Coefficient of thermal expansion
β	-	Pixel fill-factor
γ	-	Transmittance
ε_{IR}	F/m	Permittivity
ε_o	-	Relative permittivity
μ_0	-	Relative permeability
$\Re$	V/W	Responsivity
δ	μm	Deflection at free end of the cantilever
η	-	Coupling efficiency
ρ	kg/m^3	Density
ρ_r	μm	Radius of curvature
τ	sec	Thermal time constant
υ	-	Poisson's ratio
ω	rad/sec	Frequency of the incoming IR signal
ω_m	rad/sec	Modulation frequency
$\varphi(T)$	Ohm/m	Electrical resistivity of the material as a function of temperature
φ_o	Ohm/m	Electrical resistivity of the material at reference temperature

List of Acronyms

Acronym	Description
AC	Alternating Current
CMOS	Complementary Metal-Oxide Semiconductor
CMP	Chemical-Mechanical Polishing
CSA	Canadian Space Agency
CTE	Coefficient of Thermal Expansion
CVD	Chemical Vapour Deposition
DC	Direct Current
DRIE	Deep Reactive Ion Etching
FDM	Finite Difference Method
FEM	Finite Element Method
FPA	Focal Planar Array
FVM	Finite Volume Method
GUI	Graphical User Interface
IR	Infrared
LWIR	Long Wavelength Infrared
MEMS	Micro Electro Mechanical Systems
MWIR	Medium Wavelength Infrared
NEP	Noise Equivalent Power
NETD	Noise Equivalent Temperature Difference
NIR	Near Infrared
PECVD	Plasma Enhanced Chemical Vapor Deposition
PolyMUMPs	Polysilicon Multi-User MEMS Process
PSG	Phosphosilicate Glass
PSI	Phase Shifting Interferometry
PVD	Physical Vapour Deposition
RIE	Reactive Ion Etching
SEM	Scanning Electron Microscope
TCR	Temperature Coefficient of Resistance
TEM	Transverse Electromagnetic

TSS	Thin Single Stage
VOx	Vanadium Oxide
VSI	Vertical Scanning Interferometry

List of Constants

Constant	Symbol	Value and Unit
Far Infrared	FIR	15 μm − 1000 μm
Long wavelength Infrared	LWIR	8 μm − 15 μm
Short Wavelength Infrared	SWIR	1.4 μm − 3 μm
Medium Wavelength Infrared	MWIR	3 μm − 8 μm
Near Infrared	NIR	0.7 μm − 1.4 μm
Planck Constant	H	6.62607×10^{-34} J/s
Speed of Light in Vacuum	C	2.9979×10^{8} m/s
Stefan-Boltzmann Constant	σ	5.6704×10^{-8} $W/K^4.m^2$

Chapter One

Introduction

Micro Electro Mechanical Systems (MEMS) are extremely appealing for reducing the size, cost and power consumption of sensors and actuators used in a range of applications without sacrificing performance and functionality. MEMS have facilitated the invention of entirely new devices and enabled a raft of new applications across a broad range of industries. In fact, MEMS are currently being considered for integration in a number of aerospace applications, either to enhance existing technologies with lighter, more cost efficient replacement parts or as the basis for innovative new systems [1]. Issues currently impeding widespread adoption of MEMS in many areas, particularly within the space industry, include a limited understanding of the operating performance and reliability of MEMS technologies in harsh environments, such as the volatile and remote conditions of space [2].

Long-term reliability of MEMS devices can quickly be evaluated if they are made to operate under conditions that are more severe than normal, so as to accelerate factors that contribute to system failures. However, determining qualification tests for MEMS built to operate in harsh environments also requires a comprehensive understanding of the failure modes. If the modes are not properly identified and understood, the device might pass stringent qualification tests only to fail later. The challenge is that while certain aspects for MEMS are well understood (e.g. fatigue and plastic deformation), others are still difficult to predict (e.g., stiction, thermal cycling, and radiation).

The performance, reliability, and yield analyses of MEMS devices highly depend on the investigation of their thermal effects [1-2]. Therefore, thermal analysis has become a pivotal component of the MEMS design process. There are numerous heat-transfer based applications in MEMS, such as uncooled infrared sensing [2], thermal actuation [4–10], and chip cooling [26]. In recent years, the use of order reduction techniques to generate MEMS heat-transfer models has received a great deal of attention [7]. The technique is used to predict the thermal

characteristics of MEMS devices with various boundary conditions to reflect actual operating conditions. In this regard, electro-thermal modeling results generate a temperature distribution of the device which is critical for the reliability and performance analysis.

Electro-thermal models are particularly important for MEMS microbolometer pixels, which must be capable of very precise temperature detection. Typically, simplified models are developed using a lumped element method. To extract the lumped elements of the system, the device is divided into heat-transfer sub-systems of simpler geometric shapes. Then the heat capacity of each sub-system can be approximated as a lumped constant heat capacity (C_{total}), and the energy transportation mechanisms of each sub-system, such as conduction, convection and radiation effects, can be approximated as lumped heat conductance (G_{total}). Once extracted, the thermal lumped elements can be either derived analytically or extracted using numerical simulations. The applicability of lumped mass modeling will be discussed for the selected microbolometer device in chapter three.

This thesis mainly discusses the electro-thermal modeling of a microbolometer as background research for space applications. Specifically, using electro-thermal and thermo-mechanical models, both the performance and reliability characteristics of a Thin Single Stage microbolometer designed by the Canadian Space Agency (CSA) were analyzed. The geometric features and materials used to fabricate this device are presented in chapter two. An electro-thermal model suitable for the prediction of reliability and the performance of an uncooled microbolometer was developed. Analytical and numerical method was devised for solving the general electro-thermal differential equations. Much can be learned from analytical and numerical solutions regarding the quantitative and qualitative behaviour of uncooled MEMS microbolometer devices. For the case of analytical model, by solving the second order differential heat equation, an explicit formula for the solution of the electro-thermal coupling problem in microbolometer pixels was found. This qualitative insight is also useful in understanding the effect of different parameters, including material properties and device geometry, on the thermal distribution.

However, electro-thermal modeling for a Thin Single Stage microbolometer which accounts for the effects of infrared (IR) energy, radiation heat transfer, spreading resistance between the plates, as well as transient conditions, complicates the non-linear problem. In order to study these effects, a solution has been developed using a numerical model for the non-linear heat equation. We implemented the Finite Difference Method (FDM) explicit algorithm to create heat-transfer models from complex two-dimensional (2D) models and demonstrate the applications of the technique on the MEMS microbolometer pixel with various heat-transfer boundary conditions. The general goal of the numerical model is to provide a complete and accurate heat-transfer model which is compatible with actual operating conditions of the device. The numerical model can also be adapted to other system-level simulators of arbitrarily shaped MEMS devices. By contrast with the analytical approach, the numerical model is capable of capturing the geometric characteristics of the device because it is reduced from the 2D solid model of the system.

Both the analytical and numerical models provide a full link between the input electrical signal and the temperature distribution across the device, which is critical information for evaluating both thermal performance and reliability, and ultimately for predicting lifetime durability. The temperature distribution computed from analytical and FEM models is used to obtain the deflections and stresses that the structure undergoes, which is fundamental for the reliability analysis of the device. Model simulations have also been conducted to account for both ambient air and vacuum boundary conditions at steady-state.

1.1 Motivation of the Study

Designing MEMS poses some unique challenges with regard to reliability and robustness. The present research was motivated by the fact that the electro-thermal models introduced in the literature to study the characteristics of uncooled MEMS microbolometer pixels merely provide a simplified average temperature value for the microbolometer in the microplate area without accounting for the effects of radiation and convection heat transfer mechanisms [2, 13]. However, microbolometer responses, such as time constant and responsivity, are very sensitive to these heat transfer mechanisms as well as the spreading heat resistance that takes place at the contact point between the legs and microplate. Existing electro-thermal models have limited

output for the thermal distribution across the device, which is needed to improve the performance and reliability of the device [6]. In addition, the thermo-mechanical effects of uncooled microbolometers have yet to be established. The lack of complete electro-thermal analytical and/or numerical models limits a deep understanding of the behaviour of uncooled MEMS microbolometer. Therefore, the present study was undertaken to address some of the constraints present in existing models and to develop new methods to address electro-thermal analysis of multilayered structures.

1.2 Objective of the Study

The main objective of this research is to develop analytical and numerical models for the prediction of the thermal distribution and mechanical behaviour of an uncooled microbolometer pixel. The thermal distribution of the device will dictate the performance and reliability of the microbolometer. The models have been developed to account for operating conditions in air and vacuum environments. The objectives of the thesis can be summarized as follows:

a. To study the electro-thermal and mechanical characteristics of a multilayered microbolometer pixel at steady-state using analytical, numerical and finite element models while taking into account the effects of joule heating, an incoming IR energy source and various heat transfer mechanisms depending on the operating environment.
b. To develop an IR absorption model for the Thin Single Stage microbolometer pixel in order to estimate the IR energy absorbed for electro-thermal modeling.
c. To validate these models with experimental methods using a PolyMUMPs® test device.
d. To develop methods for estimating the performance of a microbolometer based on its geometry and material properties.
e. To identify the key parameters of microbolometer performance and reliability in order to achieve an improved device design.

1.3 Scope and Methodology of the Thesis

A number of factors determine microbolometer performance and reliability, especially for the case in which the device is intended for space applications [1]. This research primarily focuses on determining how electro-thermal and thermo-mechanical factors affect device performance and reliability. The electro-thermal models include the effects of joule heating and an incoming IR heat energy source as well as the different mechanisms involved on heat energy dissipation. Although the numerical model developed in this thesis is capable of handling temperature dependent material properties, throughout the present study we used constant material properties as a function of temperature. However, the thermal coefficients of resistance (TCR) for both vanadium oxide and polysilicon have been used in the models. To set the context within which the analysis has been performed, Chapters three and four are provided on the subjects of heat transfer, the Boltzmann transport equation, and key concepts of uncooled MEMS microbolometer performance.

Matlab® software has been used to simulate the electro-thermal analytical and numerical models of the different heat source and heat transfer mechanisms. A graphical user interface (GUI) was developed to generate the results for different load, geometric, and environmental conditions. The GUI provides a convenient environment for the assessment of device performance across various conditions. In addition, finite element analysis (FEA) has been used to solve the coupled electro-thermal and mechanical governing equations for temperature distribution, deformation, and stress at steady-state. The numerical and FEA models (using ANSYS®) are also used to study the transient response of electrical, thermal and mechanical properties in the resistive microbolometer, which are subjected to a DC current bias and IR radiation loads. This analysis provides the insight necessary to understand the optimum design and practical operating requirements of 2D uncooled MEMS microbolometer arrays.

1.4 Limitations and Basic Assumptions

The primary limitations and assumptions of the analytical and numerical electro-thermal models and thermo-mechanical analytical model presented in this thesis include:

i. The models use material properties from the literature as well as from the experimental evaluation of existing uncooled microbolometer prototypes provided by the Canadian Space Agency (CSA).
ii. Physical parameters such as the coefficient of thermal expansion, thermal conductivity, and Young's modulus are temperature dependent. However, in this study, these values are assumed to be constant. This is a reasonable assumption because, for silicon material, these properties only change by 1% across the temperatures of interest (200K to 350K) [11]. Both the analytical and numerical model include the thermal effect of electrical resistivity (TCR) values
iii. The physical properties of the materials used in the models are assumed to be isotropic.
iv. A DC current bias has been used as the main source of thermal energy for the analytical and numerical models. The numerical model accounts for the IR energy source in addition to joule heating.

1.5 Contributions of This Research

By taking into account joule heating and incoming IR energy sources, this research has contributed significantly to electro-thermal modeling methods of thermal distribution estimation for MEMS microbolometers. Previous modeling approaches have computed the thermal conductance of uncooled microbolometers directly from the geometry of the pixel structure [2]. In doing so, these models assume a linear temperature distribution in the pixel leg, only taking into account the effect of conduction via the legs. The thermal conductance is then used to compute the average pixel temperature. However, in this study a non-linear thermal distribution of the microbolometer is computed and then used to compute the thermal conductance. Furthermore, the models provided in this thesis can be used for other MEMS devices, including microactuators. This work also includes the use of geometric constraints, material properties, and various heat transfer mechanisms, such as joule heating and IR energy sources, to develop a robust model that can be used as part of the background work needed for the analysis of microbolometer performance and reliability. Lastly, this research also includes the experimental validation the analytical and numerical models using PolyMUMPs® test device.

1.6 Outline of the Thesis

The present chapter provides the introduction, study objectives, and outline of the thesis. Chapter two presents a literature review of electro-thermal modeling for thermal actuators and microbolometer pixels, with a focus on MEMS technology. It includes devices that have been used for previous work on electro-thermal modeling, including thermal microactuators and other MEMS devices. Chapter two also discusses the fabrication method used for the manufacturing of PolyMUMPs® test devices and an investigation of relevant material properties. Chapter three is the central part of the thesis and details the electro-thermal and mechanical modeling activities. In addition, this chapter discusses the specific theory behind heat transfer and the coupling between the electrical and thermal domains for MEMS devices. Chapter four includes a description of the microbolometer pixels studied in this thesis, as well as figures of merit and reliability considerations in the design process. The fundamental theory for the IR absorption model is also covered. Chapter five describes the analytical, numerical and FEM simulations results and provides a discussion of the different models developed in the previous chapter. This chapter also presents the experimental setup used for the testing of the PolyMUMPs® test device and the comparison of the theoretical and experimental results. Finally, chapter six provides the conclusions and recommendations.

Chapter Two

Background and Literature Review

The ability to observe and identify objects under adverse environmental conditions, such as darkness and fog, is always a highly desired capability for both military and civilian applications. Most consumer night-vision products are image intensification devices. Such image intensifier still relies on natural visible or near-infrared light, and cannot function in total darkness or in a misty environment. Far-infrared (8-14 μm wavelength range) imaging devices have drawn significant interest because they are not dependent on ambient illumination, but rather dependent on the temperature difference between the target and background. Electromagnetic waves at such a wavelength range can transmit through the atmosphere without much attenuation.

The use of uncooled microbolometer in space instruments such as infrared radiometers and earth sensors has received considerable attention in recent years [2]. However, military applications are still the most common for infrared technology, and are also the major driving force of the research and development in infrared imaging devices. Infrared sensors have been widely used in missile defence for target detection, tracking, and discrimination. Along with the development of uncooled microbolometer infrared sensors, the high performance, low cost thermal weapon sight device is available for foot soldiers to perform in starless night [13, 17].

Most of the research work in microbolometer found in the literature has been primarily focused on the optimization of their performance and the reduction of their cost [2, 13]. A number of research efforts have been made in developing electro-thermal models focusing on increasing the thermal conductance of the microbolometer to enhance its performance. However, there has been very little work on the electro-thermal modeling of microbolometer with the aim at studying their thermal distribution and reliability, in particular for the harsh and remote environments of space [2].

As a part of the Canadian Space Agency (CSA) investigation of reliability and performance for different designs of microbolometer, in this thesis, an electro-thermal model has been developed to characterize a microbolometer performance and reliability. The lifetime of the sensor to be selected must be known and compatible with the duration of the mission. At present there is no proven methodology that can be used to reliably assess the lifetime of a microbolometer prior to launching. Emphasis will be placed on the effects of different heat transfer mechanisms joule heating and IR energy on the microbolometer performance under nominal operating conditions.

Early research in electro-thermal modeling and simulation of MEMS devices was focused mainly on the area of thermal actuators [5-12], thermal gas sensors [14] and micro-mirrors [15]. These devices are usually designed to optimize the effects of the joule heating in a controlled manner in order to improve the transduction efficiency and hence, their thermal modeling is aimed at optimizing joule heating. In addition, a major difficulty in predicting the electro-thermal behaviour of electro-thermally operated structures is that the temperature distribution across these devices is nonlinear [4]. Moreover, their material properties such as electrical resistance and thermal conductivity are usually temperature dependent [10]. Although predicting the electro-thermal behaviour of microbolometer requires somewhat similar analysis, the effect of joule heating in this case is "parasitic". Furthermore, microbolometer is a multilayer structure and deal with IR energy source in addition to joule heating. Therefore, a model appropriated to account this effect is required to predict their temperature distribution for a given electrical input aimed at suppressing joule heating. This section discusses previous research conducted to model the joule heating effect in a range of MEMS devices and at the same time, aims to extend their application to uncooled microbolometer.

2.1 Thermal Modeling of Thermal Actuators and Micromirror

Extensive modeling that describes the electro-thermal and mechanical behaviour of MEMS devices such as thermal actuator and micromirror has been previously reported [4-12]. For example, Lin and Chiao studied the electro-thermal response of line-shaped microstructures [6]; Liew *et al*. modeled the thermal actuation in a bulk micromachined CMOS micromirror [7]; and Huang, Lee analyzed polysilicon thermal flexure actuators [8]. In all these cases, the electro-

thermal analysis involves a simplified one-dimensional thermal model. In addition, the thermo-mechanical problem is solved using a force method and the principle of virtual work. However, all these studies only considered conduction heat transfer to the substrate via the legs to account for the joule heating effect and assume constant material properties as a function of temperature. Furthermore, the proposed models only analyze single layer structures with simplified assumptions.

The majority of research conducted on multilayered structures is focused on the thermo-mechanical behaviour of the device. Multilayered beams have been used frequently in MEMS devices as electro-thermal actuators [4-12] and micromirror [15]. For example, Villacareu [12] formulated the displacement of a multilayered structure with response to a temperature change. While these models offer accurate solutions for structural physics, they can only be used for multilayered structures with uniform temperature distribution. Therefore, they are not suitable for the case of a multilayered device affected by joule heating. Another limitation of such models is that they cannot calculate the temperature distribution upon electrical actuation of the device.

Liew *et al*. [7] developed a coupled thermo-mechanical model for a multilayered micro-mirror. The model extracts the temperature distribution using FEM simulations and applies it to the mechanical domain which determines the displacement in terms of temperature. However, this model does not have a closed form expression that relates the input electrical signal and the output temperature in its formulation, and the temperature data is extracted from a finite element analysis. Lammel *et al*. [9] introduced a thermal model that calculates the temperature distribution of a multilayered micromirror with electrical resistance. The model considers a uniform power distribution in the actuator, and includes heat dissipation by conduction to the substrate as well as convection to the ambient environment. This formulation does not consider the temperature dependence of the actuator electrical resistance and does not link the results of the thermal model to the mechanical domain to obtain the displacement.

Yan *et al*. [5] developed an electro-thermo-mechanical model that describes the behaviour of a vertical thermal actuator. This model includes conduction through the air under the beam as a source of heat dissipation as well as the temperature dependence of the electrical resistance. The

model separately solves the electro-thermal and mechanical domains. The total mechanical displacement due to thermal load is determined by integrating the displacement across the length of the actuator over the temperature change. A linear approximation for the inverse of temperature dependent electrical resistance is used to solve the heat transport equation. In this method, the parameter that affects the mechanical displacement of the actuator is the average temperature. The model does not include the temperature dependency of the materials thermal conductivity.

Lott *et al*. [4] and Baker *et al.* [10] introduced a comprehensive electro-thermo-mechanical model that describes the behaviour of a thermo-mechanical in-plane micro-actuator (TIM). This model considers thermal conduction through the beams as well as through the air to the substrate. The temperature dependence of the electrical resistance and the effect of thermal conductivity on temperature are included in the heat transfer equations. The models separately solve the governing equations of electro-thermal and mechanical physics. The electro-thermal domain is studied by solving the one dimensional heat transfer equation. Lott *et al*. [4] also used a shape factor to account for heat conduction via air to the substrate, by employing the equations reported by Lin. [6]. Finally, for non-steady state conditions, both groups proposed a finite-difference model that takes into account the transient solution of the model; hence predicting the temperature distribution for each node at each instant until steady-state condition is reached.

It is worth noting that in general, the electro-thermal models for multilayered structures introduced in the literature up to date have only considered the joule heating effect. However, for normal operation, the Seebeck and Peltier effects in multilayered structures are usually neglected. Fundamental research is needed to determine the importance of the Seebeck and Peltier effects in the lifetime and reliability of electro-thermal MEMS devices.

2.2 Thermal Modeling of Uncooled Microbolometer

Electro-thermal modeling of microbolometer has usually been developed to optimize the devices (e.g. pixel size) and improve their performance (e.g. responsivity). Most of the modeling has focused on improving the geometry of the different structures and increasing their thermal

conductance which at the same time enhances the device performance [3, 18]. These models usually use the average temperature of the suspended plate area to optimize the design [8] and to find this average temperature, the joule heating effect is accounted by computing the power dissipated in the plate area [30]. For example, Ge Li *et al*. [11] developed an electro-thermal model, which is basically a finite element analysis tool that calculates the thermal parameters of a microbolometer. However, the model does not consider conduction through the air under the beam and the temperature dependence of the electrical resistance. Other research groups use a simplified analysis of the device performance by including the conduction via legs as the only heat transfer mechanism in the system. Then they use the average temperature on the IR absorber plate, a linear temperature distribution along the legs and constant material properties. By examining the experimental results of the above-mentioned studies, we can conclude that these assumptions may lead to inevitable inaccuracies in the models [17]. On the other hand, many researchers use finite element software to obtain the temperature distribution of the device. Finite element techniques can provide accurate results if a fine mesh size is used in the mode. However, they cannot provide analytical expressions that relate different parameters. Moreover, larger numbers of elements drastically increase the computational time, which is a decisive factor for parametric studies, sensitivity analysis, and design optimization. Such design tools are crucially important in the development of MEMS devices and in assessing their performance and reliability.

2.3 Infrared Detector Type

Two different types of infrared detectors can be identified, photon and thermal detectors. Photodetectors make use of the effects of the interaction of light with matter. In fact, this interaction occurs via the photoelectric effect, which in most cases is the primary step in the photon detection process. Photon detectors directly convert incoming photons into photocurrents. The energy of a photon having wavelength λ is

$$E_{em} = \frac{hC}{\lambda} \tag{2.1}$$

where E_{em} is the energy of the electromagnetic wave

C is the speed of light in vacuum and

λ is the wave length

h is Planck Constant

The spectral response of a photon detector depends both on the wavelength and on the power of the radiation striking it. Cryogenic cooling is normally required to prevent the thermal generation of charge carriers. These cooling requirements have made the IR systems expensive and bulky in nature [8].

In a thermal detector, when the infrared radiation strikes the surface of the device, an increase in temperature occurs which determines the change in the output signals. The output signal is generated by temperature-dependent mechanisms such as the thermoelectric effect, resistance and pyroelectric effect. The spectral response of a thermal detector is wavelength independent whereas a photon detector is dependent on the wavelength. There are a range of thermal IR detectors but the most common is the microbolometer.

2.4 Microbolometer General Background

Uncooled microbolometer detection technology has increased the interest in infrared (IR) sensors since the requirement of compact, low-cost and reliable sensors can be met using this technology [9]. A typical microbolometer structure, shown schematically in Figure 2.1, includes an IR absorber microplate connected to the substrate via legs, a reflector, a readout circuit on the substrate, and a quarter-wave resonant cavity between the microplate and the reflector. The legs serve to mechanically support the free-standing microplate and to electrically connect it with the readout circuit. The IR absorber is a stack of thin film layers and includes an IR sensitive layer whose resistance is highly dependent on its temperature. The temperature of the microplate increases when incident IR radiation is absorbed by the IR sensitive film. This increment is then detected by measuring the resistance change in the IR sensitive material. Many metals, semiconductors and superconductors are candidates for the IR sensitive material.

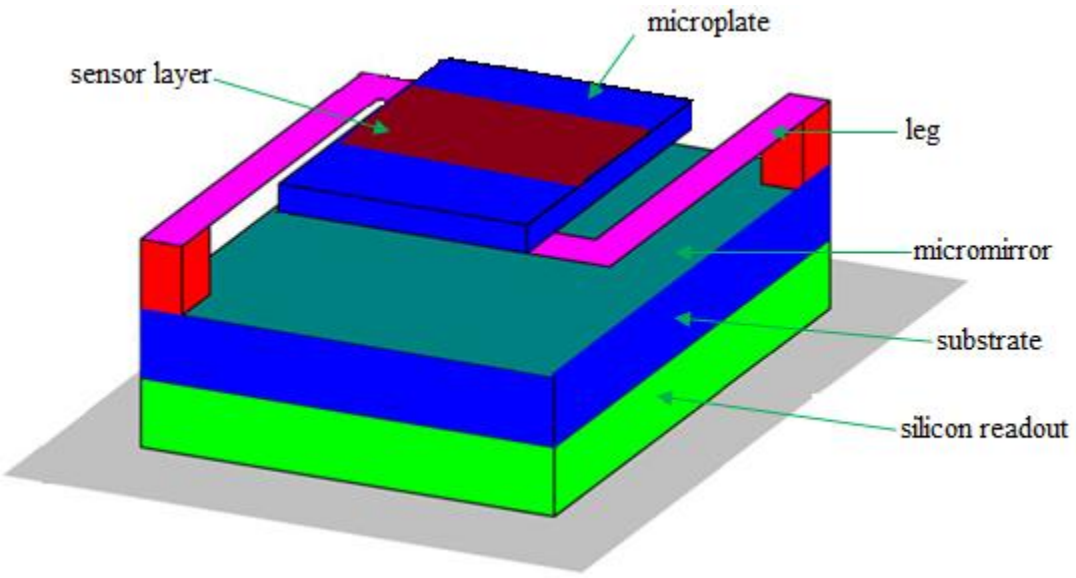

Figure 2.1: Schematic of a typical microbolometer structure

One of the most commonly used materials is vanadium oxide (VO_x), which is desirable for microbolometer with high temperature coefficient of resistance (TCR), low thermal conductance and low noise. The fraction of the absorbed infrared radiation (also called coupling efficiency, η) depends on the wavelength of the radiation; the material properties and thickness of the thin films constituting the microbolometer; and the resonant cavity between the IR absorber and the reflector.

A microbolometer requires a pulsed DC bias current to read the change in resistance due to the absorbed thermal energy. The use of large DC bias current results in high responsivity, but it also results in a significant amount of heat generated due to joule heating. To reduce the joule heating effect, the readout circuit is designed so that a large pulsed bias current is applied to a particular microbolometer pixel only at instants [11]. In this case, the noise equivalent temperature difference (NETD) can be decreased by increasing the pulse width. However, characterizing the thermal behaviour of a given microbolometer is very important to understand the device performance and reliability, even if the effect of joule heating is minimized. Hence, determining the temperature distribution for different loads and working conditions is the first major task in the design process. The temperature distribution across the microbolometer depends on a number

of factors including the geometry of the device and the thermal, electrical and optical properties of the materials.

The thermal characteristic of the device itself also changes the physical properties of the multilayered structure which in turn affects the performance and lifetime of the microbolometer [14]. As mentioned before, since uncooled microbolometers are biased by a DC current, they are subjected to an inevitable Joule-heating effect. This joule heating can be a major source of thermal energy which will affect the characteristics and the performance parameters of the device such as its thermal conductance, responsivity and NETD. It could also affect the operation of the readout circuit. Therefore, good knowledge of the heat transfer mechanisms in the microbolometer is crucial as it determines the microbolometer temperature as well as the temperature gradient taking place in the plane of the connecting legs to the substrate. For an accurate prediction of the microbolometer performance, reliability and yield, a comprehensive investigation of the electro-thermal effects is essential.

2.5 Thin Single Stage Microbolometer

To increase the thermal conductivity and performance, microbolometer pixel design has a complex geometrical feature to model. The thermal sensitive material, conductor or electrode, the IR absorber and structural layers designed with different shapes, levels (single or double) and size. Therefore in this research, to reduce computational time and resource, the actual Thin Single Stage microbolometer pixel design, obtained from Canadian Space Agency (CSA) has been modified as shown in Figure 2.2. The conductor layout in the microplate of the actual design of the pixel structure, Figure 2.2 (a), has been made straight as shown in Figure 2.2 (b). Other features including the thickness and legs arrangement remain unchanged. The Thin Single Stage microbolometer is comprised of a microplate (made of three layers of different materials) and two legs [1] as shown in Figure 2.2 (b). The three layers of material composing the microplate are a silicon nitride layer for structural support, a vanadium (V) conductor layer and a vanadium oxide (VO_x) sensor layer.

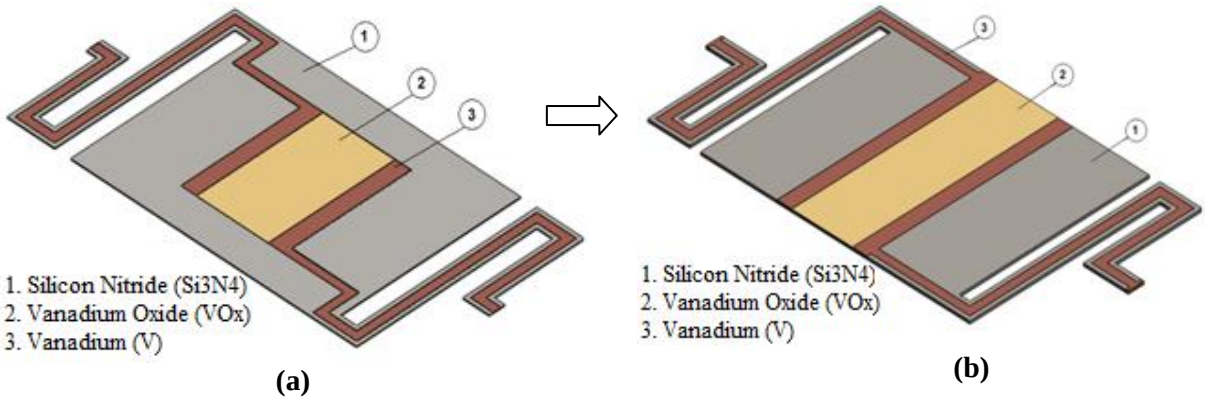

(a) **(b)**

Figure 2.2: (a) actual Thin Single Stage microbolometer design and (b) the modified Thin Single Stage microbolometer used to developed the electro-thermal and IR absorption models

The plate is supported by two folded-flexure legs made of silicon nitride (Si_3N_4) with a 3 μm width. The silicon nitride legs provide the thermal isolation between the microbolometer and the heat-sink readout substrate and support the conductive films for electrical connection. The end of the legs is fixed to the post which is anchored to the substrate (not shown in the above Figure). The microplate structure is separated from the underlying aluminum reflector with an air cavity of λ/4 (2.5 μm), where λ is the intended wavelength to be measured. The infrared radiation that is incident on the surface of the sensor (vanadium oxide) is partly absorbed by the Si_3N_4. The absorbed IR radiation heats the plate, and changes the sensor layer resistance. The resistance change is then read out by a bias current. The a more detail design parameters of the Thin Single Stage microbolometer used in the model are shown in Figure 2.3 and correspond to a Thin Single Stage microbolometer with 70 μm long legs, a plate length of 46 μm, and a width of 39 μm.

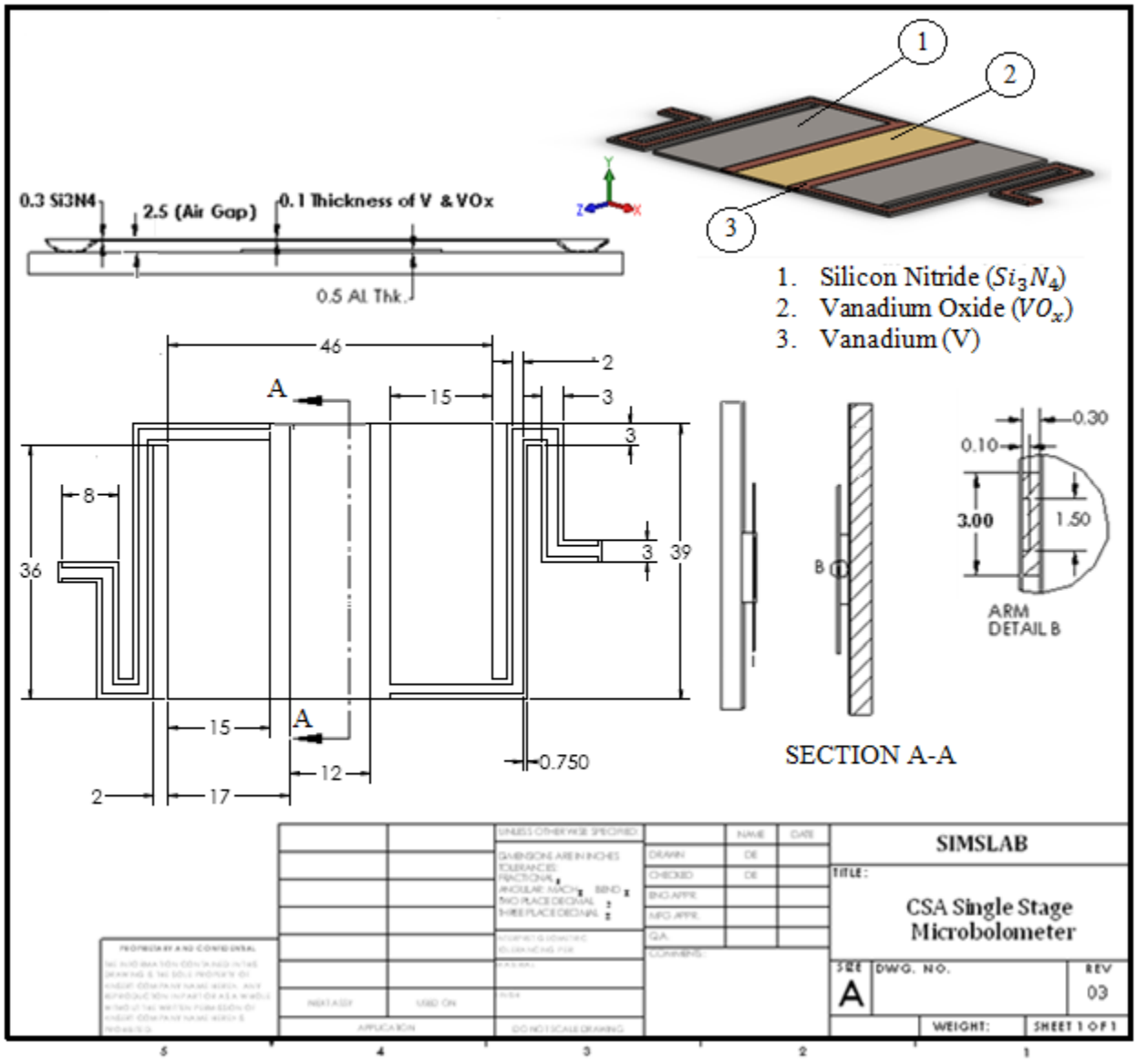

Figure 2.3: Basic geometric design dimensions (μm) for the Thin Single Stage bolometer structure

The thickness of the silicon nitride is 100 nm below the sensor material and 200 nm above with a total of 300nm. The sensor material film, vanadium oxide, on top of the microplate has a thickness of 100 nm and width of 12µm. The thin vanadium film deposited on top of the legs is 1.5 µm wide and 100 nm thick. These optimized dimensions for Thin Single Stage are used from CSA original design. The design has been done based on the device IR absorption performance and pixel design structural requirements.

Table 2.1: Thin Single stage main future dimensions [1]

Thin Single Stage Feature	Dimension
Overall Legs length	70 µm
Overall length of the microplate	46 µm
Overall width of the microplate	39 µm
Legs width	Si_3N_4 3 µm, V 1.5 µm
Thickness of Si_3N_4 below	100 nm below, 200 nm above
Thickness of VOx film	100nm
Thickness of V film	100nm
Width of V film on the bridge	2 µm
Width of VOx film on the bridge	12 µm

2.6 Test Device Used for Electro-Thermal Modeling

In the subsequent chapters, we derive comprehensive analytical and numerical electro-thermal models for Thin Single Stage microbolometer that describe the steady-state thermal distribution. To verify the analytical and numerical models test device developed in previous related research using PolyMUMPs® (Polysilicon Multi-User MEMS Process) has been used [2]. The test device mainly differs from a Thin Single Stage microbolometer with the material used for fabrication. Therefore, this section will introduce the Thin Single Stage (TSS) microbolometer and the test device. Geometrical features and material properties for both the Thin Single Stage microbolometer and the test device structure are presented.

2.7 PolyMUMPs® Design and Fabrication of a Test Device

In order to validate the analytical and numerical electro-thermal model with experimental methods, several test structures need to be fabricated. PolyMUMPs® has been selected mainly for its convenience to design a test device with a surface micro-fabrication process similar to the Thin Single Stage microbolometer [2]. PolyMUMPs® is a surface micromachining technology, composed of three structural polysilicon (Poly 0, Poly 1 and Poly 2) layers, two sacrificial

(Oxide 1 and Oxide 2) layers and one metal (gold) layer on an insulating silicon nitride layer. The nominal thicknesses of these layers are given in Table 2.2 [3].

Table 2.2: Thicknesses of the material layers used in the PolyMUMPs® process [3]

Layer Name	Thickness (um)
Silicon nitride	0.6
Poly 0	0.5
Oxide 1	2.0
Poly 1	2.0
Oxide 2	0.75
Poly 2	1.5
Metal	0.5

The first polysilicon layer is 0.5 μm thick and cannot be released from the substrate. This layer is commonly used to function as electrodes and local wiring. The second and third polysilicon layers are both releasable and are 2.0 μm and 1.5 μm thick, respectively. These layers are released to form mechanical structures. Following the deposition of each polysilicon layer, a high temperature anneal is used to alleviate residual stresses in the deposited polysilicon. An oxide layer of 2.0 μm is deposited between the first and second polysilicon layers, while an oxide layer of 0.75 μm is deposited between the second and third polysilicon layers. Finally, a 0.5 μm thick layer of gold is deposited on the third polysilicon layer [2].

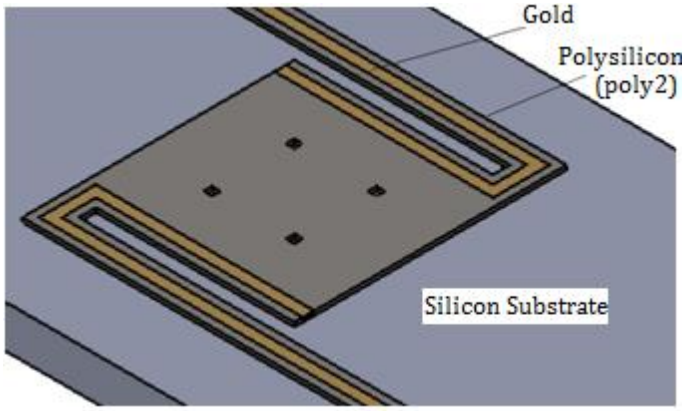

Figure 2.4: PolyMUMPs® test device structure

The 3D solid model of the PolyMUMPs® test device is shown in Figure 2.4. The detail dimensions of this device are shown in Figure 2.5. The test device has similar leg structure as the

Thin Single Stage microbolometer. The overall lengths of these two arms are 140µm. The microplate width and length of this design is 80 µm.

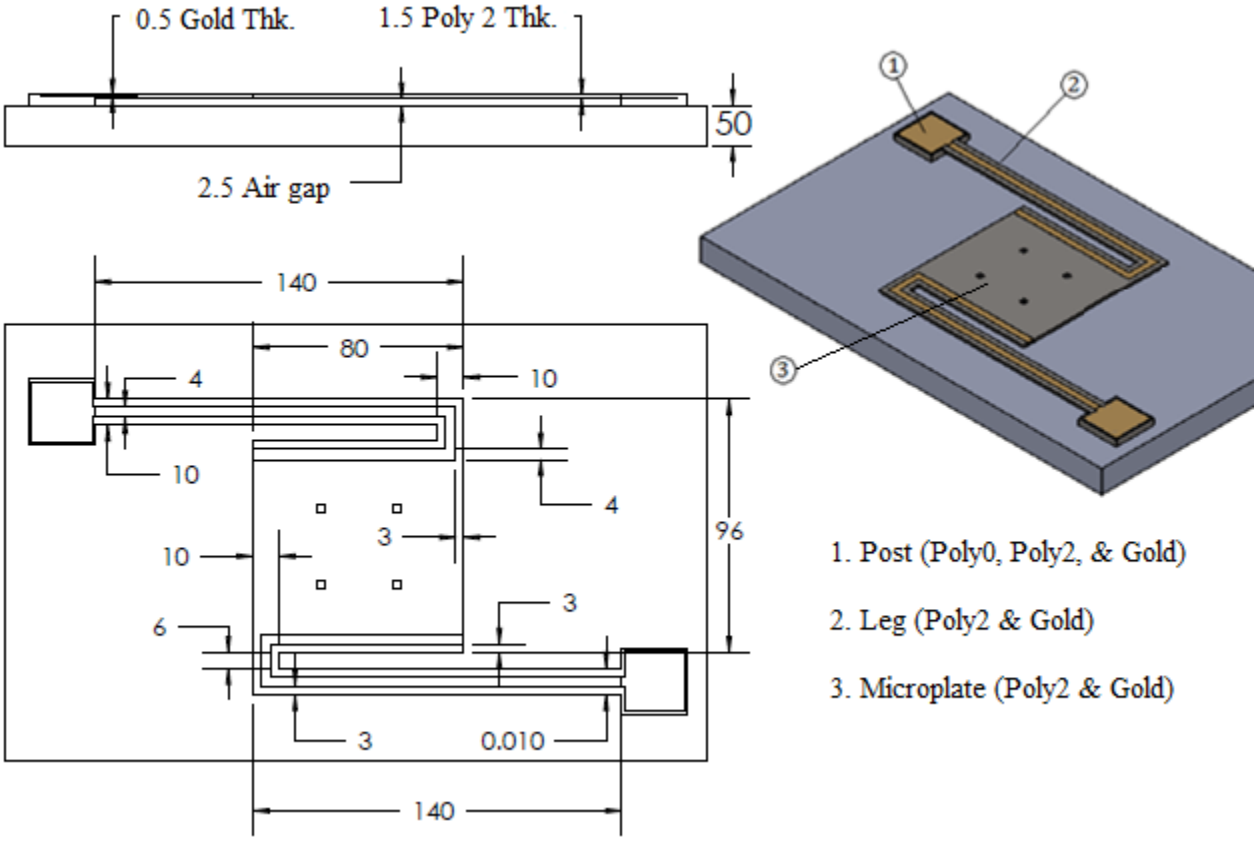

Figure 2.5: Basic geometric dimensions for PolyMUMPs® test device structure

2.7.1 PolyMUMPs® Design Limitations

The PolyMUMPs® foundry service is designed for general-purpose surface micromachining fabrication. For this reason, material, layer thickness and line widths are not optimized for the test device used in Thin Single Stage design. A general rule of thumb with PolyMUMPs® is to make all minimum geometries greater than or equal to 5 µm. This is primarily due to alignment issues between masks and the resolution of the lithography system used. Because the test device's legs can be etched with one mask, alignment is not a concern for the microbolometer, and most legs were created with a width of the nominal recommended minimum geometry size of 3µm.

2.7.2 Test Device Fabrication

The process flow for the test devices is shown schematically in Figure 2.6. The process begins with an n-type (100) silicon wafer. First, a 600 nm low-stress LPCVD (low pressure chemical vapour deposition) silicon nitride layer is deposited on top of the silicon wafer (Figure 2.6). This silicon nitride layer serves as an electrical isolation between device structural components and the silicon substrate. Following the deposition of silicon nitride, a 500 nm LPCVD polysilicon layer (Poly 0) is deposited. Poly 0 is patterned by photolithography, a process including coating the wafer with photoresist, exposure of the photoresist with the appropriate mask, and developing the exposed photoresist for patterning. After patterning, Poly 0 is etched in an RIE (Reactive Ion Etch) system. The 0.5 μm polysilicon layer (Poly0) is used as the bottom layer of the contact pads (Figure 2.6).

A 2.0 μm phosphosilicate glass (PSG) is then deposited by LPCVD and annealed at 1050^{o}C for one hour in Argon. This layer, known as Oxide 1 (or the First Oxide), is the first sacrificial layer. During the process, the PSG sacrificial layers are patterned and etched to form the substrate connection of the microbolometer through the support arms. The polysilicon structural layer (Poly2) is used, to form the microbolometer support and plate (Figure 2.6). The patterning of Poly 2 includes forming the etch holes using the HOLE2 mask, which reduces the stiction during the final release of the structure.

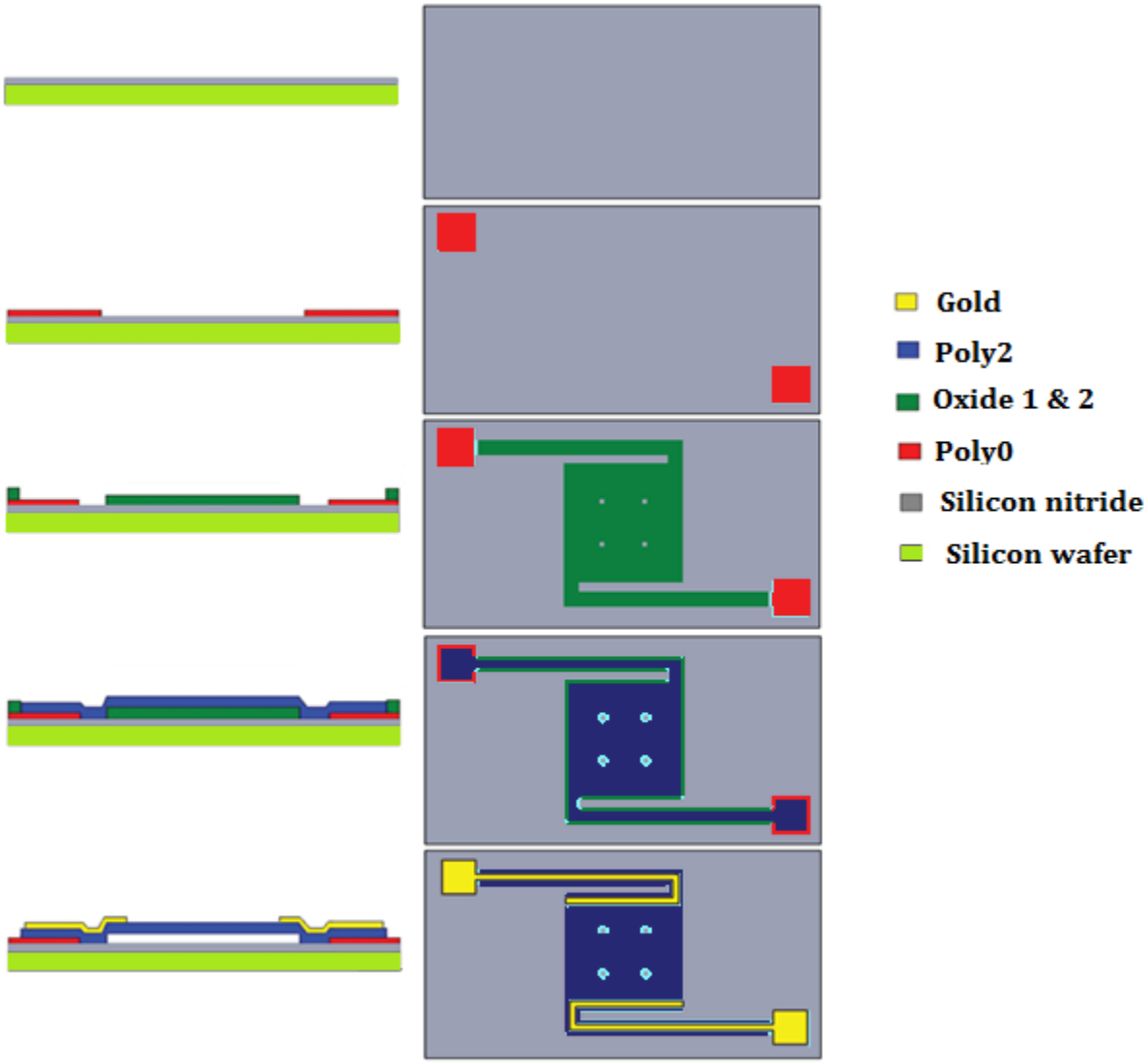

Figure 2.6: The fabrication process for the test device

The final deposited layer is a 0.5 μm thick gold layer. This layer, also known as the metal layer, is patterned to form the electrical connections, the gold coatings at the arms and the electrodes at the microplate. The 0.5 μm thick gold layer is used to form the 100 μm × 100 μm contact pads and the electrical connections which connect the contact pads to the plate. Coating the arms with gold increase the thermal conductivity and reduce the electrical resistance of the arms. This way, the resistive heating takes place mainly on the microplate. The two gold lines located close to the two edges of the microplate are used as electrodes. They increase the uniformity of the electrical

current, resulting in more uniform resistive heating within the microplate. The Poly2 layer that forms the arm encloses a 4μm width gold layer line for better conduction.

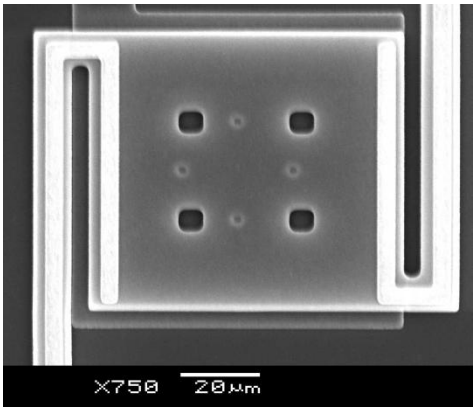

Figure 2.7: The SEM images of the fabricated test structures

The test devices were released by immersing them in a 49 % HF solution followed by CO_2 critical point drying to avoid stiction. The Scanning Electron Microscope (SEM) photo included in Figure 2.7 shows the fabricated test device.

2.8 Review of Important Material Properties

Microbolometers are constructed out of a multitude of materials, each of which has unique performance and reliability implications. In chapter three, numerical modeling of the microbolometer is described that allows for updates of the material properties to occur as time advances and the simulated temperatures change in response to an applied current. This permits a more complete and accurate model of the microbolometer response so long as there exist a good knowledge of the material's characteristics with respect to temperature variations. This section will review the present understanding of parameters important to the modeling of a microbolometer. This section offers a brief overview of the materials properties used for Test device and Thin Single Stage microbolometer. The material properties of silicon nitride, vanadium oxide and vanadium used for the analysis are listed in Table 2.3.

Table 2.3: Material properties used in the subsequent models [1, 22-24]

Material Properties	Unit	Silicon nitride (Si_3N_4)	Vanadium oxide (VOx)	Vanadium (V)
Coefficient of thermal expansion (CTE)	K^{-1}	3.3×10^{-6}	2.9×10^{-6}	2.9×10^{-6}
Young's Modulus	MPa	300×10^{3}	155×10^{3}	128×10^{3}
Poisson's ratio	-	0.27	0.42	0.37
Thermal conductivity	W / m. K	1	1	15
Electrical resistivity	Ω. m	1e13	3e-8	3e-13
Density	kg / m^3	2340	4340	6100
Specific Heat	J / kg. K	710	460	500
Temperature Coefficient of Resistance (TCR)	K^{-1}	-	- 2%	- 0.2%

Generally Isotropic material properties have been assumed for analytical, numerical (FDA) models and FEM simulations developed in this study. One of the main constraints in this research is most of these material properties are not well known as a function of temperature. Particularly, effect of temperature for thermal conductivity, thermal expansion and electrical resistive is critical in the electro-thermal models results. Therefore, all the material properties listed in Table 2.3, with the exception of electrical resistivity, are assumed to be constant as a function of temperature in the simulations.

The test device is fabricated using PolyMUMPs® process with polysilicon structural layer and Gold as conductor. Complete lists of the material properties for these materials are given in Table 2.4. Preliminary FEM models predict thermal conductivity and electrical resistance of the material in particular affect the significantly the MEMS device electro-thermal models. Therefore, these critical material properties of polysilicon, such as the thermal conductivity and electrical resistivity, for the test device have been discussed in the following section. In chapter three and simulation results will presents the significance of thermal conductivity and electrical resistivity for the electro-thermal models in particular.

Table 2.4: Material properties of polysilicon and gold used for the subsequent models [3]

Material Properties	Unit	Polysilicon	Gold
Coefficient of thermal expansion (CTE)	K^{-1}	3.3×10^{-6}	2.9×10^{-6}
Young's Modulus	MPa	300×10^{3}	155×10^{3}
Poisson's ratio	-	0.27	0.42
Thermal conductivity	W / m. K	41	320
Electrical resistivity	Ω. m	1.5e-5	3e-8
Density	kg / m^3	2330	19300
Specific Heat	J / kg. K	753	129
Temperature Coefficient of Resistance (TCR)	K^{-1}	-0.0058	

The performance of microbolometer is highly affected by their material properties. This section provides some basic material property information that can be used for the modeling and analysis of microbolometer, with an emphasis on devices constructed of test device with polycrystalline silicon. The thermal conductivity and electrical resistivity are the two most critical material properties are investigated in the determination of the electro-thermal model of the structure.

2.8.1 Thermal Conductivity

In the modern view of materials, a solid may be comprised of free electrons and of atoms bound in a periodic arrangement called the lattice. Accordingly, the transport of thermal energy is due to two effects: the movement of free electrons, and vibration waves of the lattice. These two effects are additive so that the total thermal conductivity k of a material is the sum of the electrical component k_e and the component from the lattice k_l. With crystalline materials, the regularity of the lattice arrangement results in higher thermal conductivities than amorphous materials like glass. Moreover, the effects of temperature on crystalline materials can be significant. The thermal conductivity of crystalline silicon has been consistently reported to drop from approximately 150 to 22 W/m K between room temperature (298 K) and the melting point of silicon (1685 K). The variation in thin-film polysilicon, however, has been reported with less consistency. This is most likely due to variations in impurity concentration and grain size from different fabrication processes. The thermal conductivity of polysilicon films produced in CMOS

IC technology has been measured in the temperature range from 80 to 400 K. Electronic and lattice thermal conductivity were determined using electrical and galvanomagnetic data obtained from the same film. This study found little variation with temperature above room temperature and reported 29 W/m/K for the thermal conductivity with an electronic content, ke, of less than three percent.

2.8.2 Resistivity and TCR

The resistivity of polysilicon is much greater than that of similarly doped, single-crystal, epitaxial silicon. Resistivity changes slowly at low dopant concentrations, but decreases rapidly at intermediate dopant concentrations. At high dopant concentrations (1020 atoms/cm^3), it approaches the resistivity of single-crystal silicon for similar dopant levels, suggesting a resistivity-limiting point at the solid solubility of the particular dopant in silicon. For prototype polysilicon, setting room temperature resistivity by controlling doping levels is an issue that is well studied; the doping process is used extensively in the IC industry and allows the actuator to operate at voltages and currents compatible with standard integrated circuitry (CMOS).

However, at high temperatures (beyond 750 to 800 ^oC) the resistivity is less predictable and not well understood because of self-annealing and irreversible changes in the polysilicon structure that occur. The resistivity of polysilicon (φ), is usually related to temperature with a linear relationship controlled by a temperature coefficient of resistance, α a relationship for the resistivity that is linear with temperature is

$$\varphi(T) = \varphi_o\big(1 + \alpha(T(x) - T_o)\big) \tag{2.2}$$

where $T(x)$ is the operating temperature, T_o is the reference temperature, and $\varphi_o$defines the resistivity at the reference temperature. This expression has been used by many to model the temperature dependence of resistivity in sensor applications and microactuators with polysilicon and other materials.

Chapter Three

Electro-Thermo Mechanical Modeling

Thermal analysis has become a crucial component of a MEMS design process. The performance, reliability and yield analysis of MEMS devices highly depend on the investigation of thermal effects. In Microsystems with electrical input such as microbolometers, the electro-thermal analysis is a major step in the prediction of the temperature distribution. The temperature distribution in the pixel structure is critical information for predicating the performance and reliability of the device. Canadian Space Agency (CSA) has been investigating the performance and reliability of a microbolometer. This thesis is a part of this study with significant support from CSA including geometrical design of the microbolometer pixel design and some material properties related to the device studied [1].

A major objective of this research is to develop electro-thermal models in order to determine the temperature field in microbolometer pixel structure resulting from various heat sources and heat transfers mechanisms imposed on its boundaries. Basically, we are interest to know the temperature distribution, which represents how temperatures various with position in the medium. Once this distribution is known, the heat flux at any point in the medium or on its surface may be computed from Fourier's law. Using the thermal distribution, other important quantities of interest, such as pixel conductance and device performance can also be determined. Furthermore, for microbolometer knowledge of the temperature distribution could be used to ascertain structural integrity by simulating of thermal stresses, expansions, and deflections. The temperature distribution could also be used to optimize the various layers thickness used to fabricate the device and select appropriate materials properties and packaging environment for the required performance.

The most important electro-thermal effects in multilayered MEMS devices are given in Table 3.1. The modeling of electro-thermal effects (e.g. joule heating, Seebeck effect, Peltier effect, etc.), becomes increasingly important during MEMS product design process [21].

Table 3.1 Electro-thermal effects in multilayered MEMS devices

	Thermal	Electrical
Thermal	***Heat conduction***	***Thermoresistance*** Seebeck effect Pyroelectricity
Electrical	***Joule heating*** Peltier effect Thomson effect	***Electrical conduction***

Due to limitation of the material properties availability for Peltier coefficients and Seebeck constant for Thin Single Stage material, these effects are not included in the analysis of the device. Joule heating is the dominant source of heat generation and it is caused by the electrical current passing through the material. Joule heating is defined by Joule's law, which for an ohmic conductor has the form [5]:

$$q_{JH} = j^2 \varphi(T) \tag{3.1}$$

where q_{JH} is the joule heat generated per unit volume in.

j is the current density vector in

$\varphi(T)$ is the resistivity of the material as a function of temperature

This chapter presents a unified approach for the solution of the coupled electro-thermal partial differential equations for multilayered MEMS devices, in particular microbolometer, under the effect of joule heating and IR energy source.

3.1 Fundamental Heat Transfer Equations

The general approach to determine the temperature distribution is to apply the energy conservation requirement for a selected control volume. In order to apply conservation of energy, we first define an infinitesimally small control volume, dx.dy.dz for Thin Single Stage microbolometer as shown in Figure 3.1. Joule heating and IR are the main source of heat energy

for the microbolometer pixel structure. Depending on the operating environment different heat transfers mechanisms will be used to introduce the appropriate energy balance equations for the control volume. The result is a differential equation whose solution, for a given boundary conditions, provides the temperature distribution in the medium. The most general expression for heat transfer in a control volume is given by Eq. (3.2). It describes the heat exchange between heat carriers, which are energy quanta of lattice vibrations, and the lattice [18]. For the case in which the heat carrier mean free path is comparable with the characteristic dimensions at micro scale, the Boltzmann transport equation is given by,

$$\nabla \cdot \left(k(x,y,z)\nabla T(x,y,z,t) + Q_{total}(x,y,z,t)\right) - \rho(x,y,z)c\frac{\partial T}{\partial t} = 0 \tag{3.2}$$

where $\kappa(x,y,z)$ is the thermal conductivity of the material

c is the specific heat capacity

$\rho\,(x,y,z)$ is the density

$T\,(x, y, z, t)$ is the temperature distribution and

$Q_{total}\,(x, y, z, t)$ is the heat generation or absorbed by the control volume

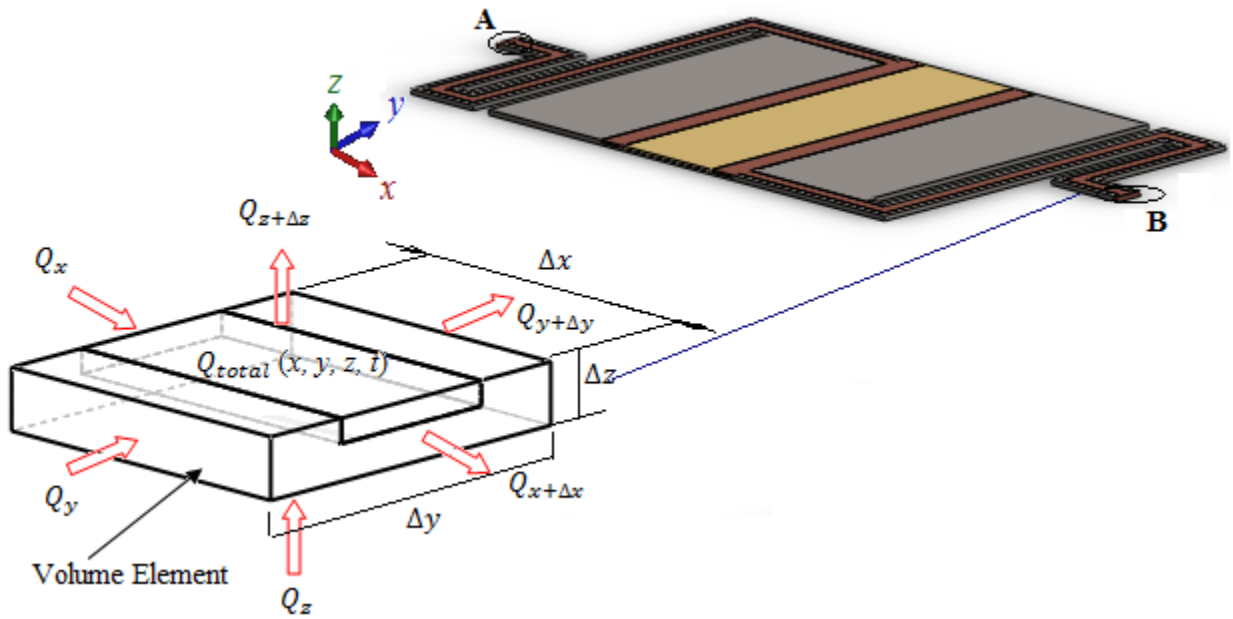

Figure 3.1: Three-dimensional heat conduction computational domain for a rectangular volume element

Equation (3.2) states that the temperature profile within a body depends on the rate of its internally heat generated or absorbed, its capacity to store energy and the rate of thermal conduction to its boundaries (where the heat is transferred to the surrounding environment). Assuming a homogeneous medium within which there is no bulk motions and the temperature distribution $T(x, y, z, t)$ is expressed in Cartesian coordinates. This parabolic heat transfer equation specifies the complete spatial and time profile of the temperature distribution within the computational domain, as shown in Figure 3.1.

The solution of Eq. (3.2) requires the determination of the initial and boundary conditions for the domain. Assuming the initial temperature distribution at $t = 0$ is the substrate temperature, T_s, the initial boundary condition is given by,

$$T(x, y, z, 0) = T_s \tag{3.3}$$

This boundary condition states that the temperature of the microbolometer pixel structure will have the substrate temperature before heat generation or abortions. The substrate size is relative much larger than the pixel structure, therefore, we can reasonable assume the substrate temperature to remain constant, transferring most of the heat to the packaging components and to the environment. The substrate temperature is assumed to be the environmental temperature in the subsequent simulations. The temperature distribution at the boundary, which is at contact between the legs, point A and B in Figure 3.1, and the substrate, can be modeled by the Dirichlet boundary condition as follows [19]:

$$T(x, y, z, t) = T_s(x, y, z, t) \tag{3.4}$$

This boundary condition provides that the temperature of the contact point will have the substrate temperature all time. The boundary conditions assume that the substrate is used as a prefect heat sink. The heat flux through the body boundaries q_t can be modeled by the Neumann boundary condition which is given by:

$$Q_{total}(x, y, z, t) = Q_{JH}(x, y, z, t) + Q_{IR}(x, y, z, t) \tag{3.5}$$

where $Q_{JH}(x, y, z, t)$ is the total heat energy generated from joule heating

$Q_{IR}(x, y, z, t)$ is the total heat energy absorbed form the infrared radiation

Convection heat transfer takes place when sub-volumes of fluid move from one place at a certain temperature to another at a different temperature. This condition assumes that the normal heat flux through the boundary is proportional to the temperature difference between the boundary and the ambient temperature of the adjacent fluid [19]. Hence,

$$Q_c(x, y, z, t) = h(T(x, y, z, t) - T_{ambient}) \tag{3.6}$$

where $Q_c(x, y, z, t)$ is the amount of heat energy transferred by convection

$T_{ambient}$ is the environment temperature

In Eq. (3.6), h is the heat transfer coefficient which characterizes the thermal flow as well as the thermal contact between the conducting solid. The substrate temperature assumed to be equal to the ambient temperature in the subsequent models. The substrate temperature is also considered as a perfect heat sink. The heat transfer by radiation can be modeled with radiation boundary condition which is given by [19],

$$Q_{rad}(x, y, z, t) = \epsilon.\sigma.A_s\left(T^4_{surface}(x, y, z, t) - T^4_{ambient}\right) \tag{3.7}$$

where $Q_{rad}(x, y, z, t)$ is the radiation heat transfer rate

ϵ is the surface emissivity,

σ is the Stefan-Boltzmann constant

A_s is the surface area of the differential elements in which the heat is radiating

3.2 Solving the Heat Transfer Partial Differential Equation

In the following section, we will use a discretized computational domain in space which will lead to a set of ordinary differential equations defining the heat transfer.

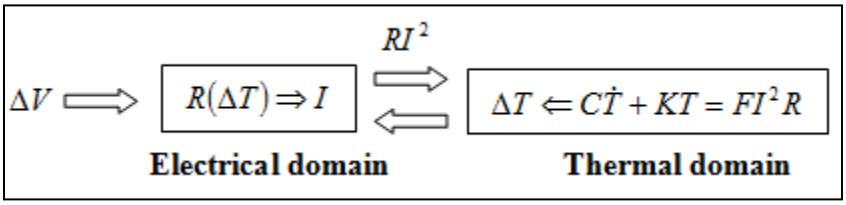

Figure 3.2: Coupled electro-thermal simulations at system level for the joule heating. The heat generation is assumed to be homogeneous.

The electro-thermal coupling at the system level, assuming a homogeneous heat generation within a lumped heater, for the special case of joule heating in a Microsystem is presented in Figure 3.2. The coupling will be more complicated if the temperature dependency of semiconductor devices is taken into account [37]. For our case, the thermal system is given by,

$$C\dot{T} = KT = F_i Q_i \tag{3.8}$$

where K and C are the system matrices, $\mathbf{T}$ is a vector of unknown temperatures at nodes made during the discretization, $\mathbf{F}_i$ is a load vector corresponding to the i-th heat source, and Q_i is an input function, that is how the i-th heat power changes in time. Using the method of separation of variables, we can define the temperature distribution as the infinite series expansion,

$$T(x, y, z, t) = \sum_{i=0}^{\infty} a_i(t)\, f_i(x, y, z) \tag{3.9}$$

Equation (3.9) gives a full form to solve both steady and transient conditions for the heat distribution of a given problem. To solve the heat transfer equation, we start with a set of functions in the computational domain $f_i\,(x, y, z)$ and then proceed systematically to determine the unknown coefficients $a_i\,(t)$ within the series.

When a DC current bias is applied to the system, the temperature along the structure will increase due to joule heating until it reaches a steady state. Because of its small thickness (compared to its length), the steady state electro-thermal response of the microbolometer leg is generally simplified to a one-dimensional heat transfer problem [19]. The effect of the two dimensional heat flowing from the microplate to the leg is considered by calculating the contact

resistance between the legs and the plate. The microbolometer structure is decomposed into a series of interconnected beams and plates [19]. The heat dissipation to the substrate is modeled as conduction through air and a conduction shape factor that accounts for conduction from the sides of the legs to the substrate and the environment [18].

3.2.1 Criteria for Lumped System Analysis

During a heat transfer process analysis, some bodies are observed to have a uniform interior temperature at all times. The temperature of such bodies can be taken to be a function of time only, T (t). Heat transfer analysis that utilizes this idealization is known as lumped system analysis**,** which provides great simplification in certain classes of heat transfer problems without much sacrifice from accuracy [15]. The lumped system analysis certainly provides great convenience in heat transfer analysis, and naturally we would like to know if it is appropriate to use for Thin Single Stage microbolometer. The first step in establishing a criterion for the applicability of the lumped system analysis is to define a characteristic length as

$$t_p = \frac{Volume}{Area} = \frac{V_m}{A_s} \tag{3.10}$$

where t_p is the microplate thickness, the smallest feature dimension in microbolometer pixel design

V_m is the microplate Volume,

A_s surfer area

The Biot number B_i defined as

$$B_i = \frac{ht_p}{k} \tag{3.11}$$

where *k* is the thermal conductivity of the material

The Biot number is the ratio of the internal resistance of a body to heat conduction to its external resistance to heat convection. Therefore, a small Biot number represents small resistance to heat conduction, and thus small temperature gradients within the body.

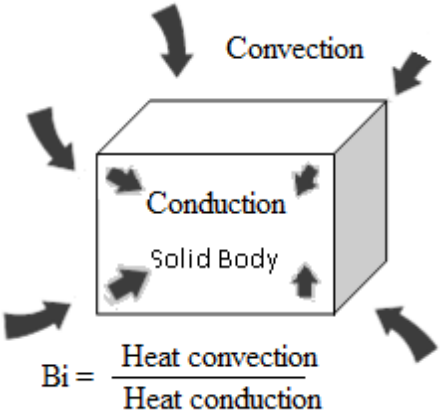

Figure 3.3: The Biot number can be viewed as the ratio of the convection at the surface to conduction within the body.

It can also be expressed as shown in Figure 3.3

$$B_i = \frac{h}{k/t_p}\frac{\Delta T}{\Delta T} = \frac{Convection\ at\ the\ surface\ of\ the\ body}{Conduction\ within\ the\ body} \tag{3.12}$$

$$B_i = \frac{\frac{t_p}{k.A}}{\frac{1}{h.A}} = \frac{Conduction\ resistance\ within\ the\ body}{Convection\ resistance\ at\ the\ surface\ of\ the\ body} \tag{3.13}$$

$$B_i = \frac{t_p/k}{1/h}$$

Lumped system analysis assumes a uniform temperature distribution throughout the body, which will be the case only when the thermal resistance of the body to heat conduction (the conduction resistance) is zero. Thus, lumped system analysis is exact when B_i = 0 and approximate when B_i > 0. Of course the smaller the biot number is the more accurate the lumped system analysis. It is generally accepted that lumped system analysis is applicable if $B_i \leq 0.1$ [15]. When this criterion is satisfied, the temperatures within the body relative to the surroundings (i.e. T - T_s) remain within five percent (5%) of each other even for well-rounded geometries such as a spherical ball. Thus, when B_i 0.1, the variation of temperature with location within the body will be slight and can reasonably be approximated as being uniform.

For Thin Single Stage microbolometer the analytical and numerical models proposed to solve the electro thermal effect in vacuum and air environment conditions. In the case of vacuum

condition the Biot number is approximately zero if we ignore the effect of radiation for lower temperature operation. For air environment the bio number need to be calculated using Eq. (3.11) and give as follow

$$B_i = \frac{10\frac{w}{m}(300\ X\ 10^{-9}m)}{1\ w/m} \tag{3.14}$$

$$B_i = 3.0\ X\ 10^{-6}$$

This value is much less than the required 0.1 value to assume a lumped mass model for Thin Single Stage microbolometer. Therefore, in the subsequent section we will present a lumped analytical and numerical electro-thermal model for Thin Single Stage microbolometer.

3.3 Electro-Thermal Analytical Modeling

Electro-thermal model of Thin Single Stage microbolometer has been developed and used to analyze the behaviour of multilayered MEMS structures. The device structure in Figure 3.4 is a full model used to develop the Electro-thermal analysis. The following assumptions have been also made for the steady-state solution:

i. The microbolometer thickness is very small compared to its length, i.e. $t_l \ll l_l$ and $t_p \ll l_p$ (t and L are the thickness and length of the microbolometer pixel, respectively. The subscript l and p stand for the microbolometer leg and microplate respectively). Therefore, the thickness effects are ignored, i.e., the temperature distribution along the plate and leg thickness is assumed uniform.
ii. There is no thermal resistance and peeling effect between any two neighbouring layers.
iii. The electrical resistance varies linearly with temperature for Vanadium oxide as defined in Eq. (2.2). Other electrical and thermal parameters of film materials are assumed to be constants, as listed in Table 2.3.

With these assumptions, the heat transfer equation is obtained by examining the differential element shown in Figure 3.4. For Thin Single Stage microbolometer, the differential element is composed of vanadium oxide and Silicon Nitride with a thickness (t_{VOx} & t_{Si3N4}), width (w_{VOx} & w_{Si3N4}), and length dx. For the general case of a DC current biased and IR energy source microbolometer, the energy balance for the differential element can be expressed as:

$$Q_{st} = Q_{IR} + Q_{JH} + \left(Q_{cond\_air} + Q_{cond} + Q_{Conv.}\right) + Q_{rad} \tag{3.15}$$

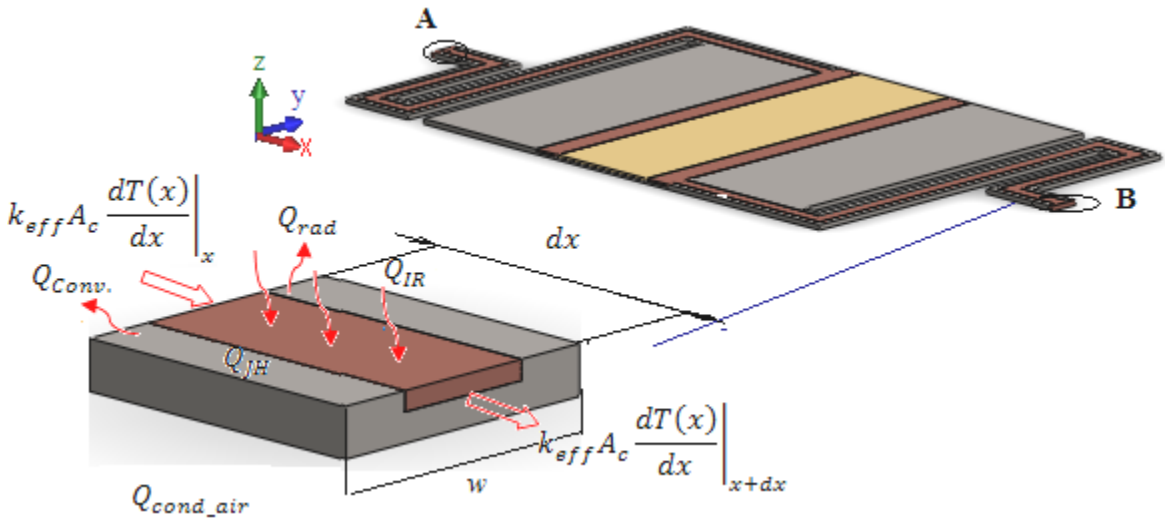

Figure 3.4: Differential element used for the thermal analysis

where, Q_{st} : Internal energy stored

Q_{IR} : Infrared energy absorbed

Q_{JH} : Rate of heat energy generated by joule heating

Q_{cond_air}: Heat energy conduction via legs

Q_{cond} : Heat energy conduction to the substrate through air

$Q_{Cov.}$: Heat convection to the surrounding from the top surface

Q_{rad} : Heat radiation to the surrounding

Using the radiation and convection boundary conditions given by Eq. (3.5) and (3.6), Eq. (3.16) can be expressed as:

$$C_{total}\frac{dT(x)}{dt} = (\,(P_{abs}).V_{ele}) + (q_{JH}.V_{ele}) - G_{th}(T(x) - T_{sub}) - \varepsilon\sigma A_s(T(x)^4 - T_{ambient}^4) \quad (3.16)$$

where $T(x)$ is the bolometer operating temperature

T_{sub} is the substrate temperature (taken as a prefect heat sink)

C_{total} is the total heat capacity of the multilayered structure

$\frac{dT(x)}{dt}$ is the rate of temperature change

η is the optical absorption efficiency of the detector,

P_{abs} is the optical signal power absorbed per unit volume

q_{JH} is the joule heat generated per unit volume as given in Eq. (3.1) ,

V_{ele} is the volume of the differential elements

ε is the detector emissivity,

σ is the Stefan-Boltzmann's constant

A_s is the detector area,

G_{th} is the conduction and convection thermal conductance of the detector and given by Eq. (3.17). The conduction for the microbolometer includes heat transfer via the legs to the heat sink and underneath the microplate air to the heat sink, in the case of air environment operating condition,

$$G_{th} = G_{cond} + G_{gas\_cond} + G_{Conv} \quad (3.17)$$

Equation (3.16) includes Q_{JH} and Q_{IR}variable heat energy source components. Heat generated by the DC bias current (Q_{JH}) is variable since the resistivity of the material change as a function of temperature. The IR radiation energy (Q_{IR}) component is variable due to time varying IR signal. At steady state, the rate of change of internal energy, (Q_{st}= C_{total} (d T(x) /dt)), is zero. As indicated in the first chapter, Thin Single Stage for the specified design burn at contact point between the leg and microplate location when 10 μA current applied. In order to investigate this

effect, the analytical model considers joule heat energy source form a DC bias current. Therefore Eq. (3.16) can be reduced to,

$$0 = \left(\left(P_{abs}\right).V_{ele}\right) - G_{th}(T(x) - T_{sub}) - \varepsilon\sigma A_s(T(x)^4 - T_{ambient}^4) \tag{3.18}$$

The steady-state temperature distribution along the legs and the microplate of the microbolometer are obtained by solving Eq. (3.18) for $T(x)$. The substrate temperature in Eq. (3.18) is assumed to be an ideal heat sink with ambient temperature value. By replacing the variable for the differential element in Eq. (3.18) the steady state condition can be expressed as:

$$\begin{aligned}\left(\left(P_{abs}\right).V_{ele}\right) - k_{eff}A_c\left.\frac{dT(x)}{dx}\right|_x + k_{eff}A_c\left.\frac{dT(x)}{dx}\right|_{x+dx} - hw(T(x) - T_s)dx \\ - Sk_{bottom}(T(x) - T_{sub})dx - \varepsilon\sigma A_s(T(x)^4 - T_{ambient}^4) = 0\end{aligned} \tag{3.19}$$

where k_{eff} is the effective thermal conductivity of the multilayered structure defined by Eq. (3.21),

A_c is the total cross-section area of the differential element (area of vanadium and silicon nitride)

w width of the differential element

S is the shape factor, and

k_{bottom} represents the thermal conductance of the layer underneath the microbolometer

In Eq. (3.19), h is the heat transfer coefficient of convection and it accounts for the heat dissipation via convection from the top surface of the microbolometer to the environment and it is on the order of 10 W/ (m^2.K) for free convection [25], thus meaning that the conductive heat dissipation is very small.

The term ($\varepsilon\sigma A_s$ [$T(x)^4 - T_s^4$]) is the heat loss from the detector by radiation, which could be negligible at low temperatures. FEA simulations performed on a Thin Single Stage microbolometer using ANSYS® has shown that the maximum temperature reached is below

300K for a 10 μA load. Hence, we have neglected the effects of radiation in the analytical model. However, it should be included in the model for high temperature applications.

The Thin Single Stage microbolometer leg and microplate multilayered structure is studied as a lumped model, where the weighted heat capacitance and thermal conductance of each individual layer are added up. The equivalent heat capacitance of the multilayer structure can be expressed as,

$$C_{total} = \sum_{i=1}^{n} c_i \rho_i v_i \tag{3.20}$$

where *n* denotes the number of layers

c_i is the specific heat capacity of each layer

ρ_i is the density of the each materials

v_i volume of the differential element

The equivalent heat conductance of the multilayer structure can be expressed as,

$$k_{eff} = \frac{1}{R_{eff}} \tag{3.21}$$

where R_{eff} is the effective thermal resistance of the multilayered structure. Equation (3.21) states that the effective thermal conductivity of the multilayered structure can be computed from effective thermal resistance. The effective thermal resistance can be used to solve steady heat transfer problems that involve parallel layers or combined series-parallel arrangements.

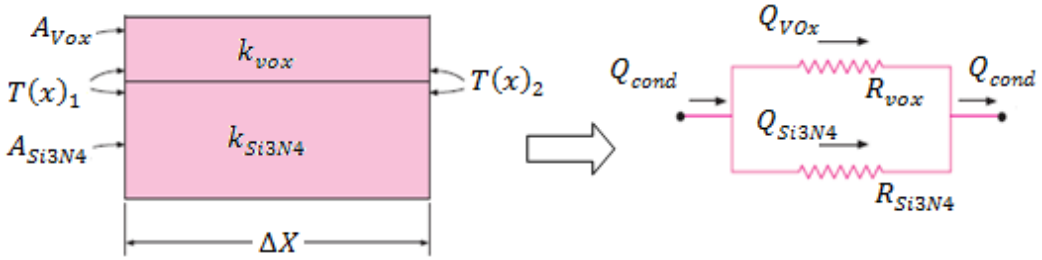

Figure 3.5: - Thermal resistance network for the two parallel layers of Thin Single Stage microbolometer

The thermal resistance network, which consists of two parallel resistances, can be represented as shown in the Figure 3.5. Noting that the total heat transfer is the sum of the heat transfers through each layer, we have

$$Q_{cond} = Q_{VOx} + Q_{Si3N4} = \frac{\Delta T(x)}{R_{Vox}} + \frac{\Delta T(x)}{R_{Si3N4}} = (\Delta T(x))\left(\frac{1}{R_{Si3N4}} + \frac{1}{R_{VOx}}\right)$$
$$R_{vox} = \frac{\Delta X}{k_{vox} A_{Vox}} \quad \& \quad R_{Si3N4} = \frac{\Delta X}{k_{Si3N4}\, A_{Si3N4}} \tag{3.22}$$

where A_{Vox} and A_{Si3N4} are the cross-section area of vanadium oxide and silicon nitride layer

k_{vox} and k_{Si3N4} are the thermal conductivity of vanadium oxide and silicon nitride respectively

$Q_{VOx}\ and\ Q_{Si3N4}$ are the heat flow via the vanadium oxide and silicon nitride layer respectively

Figure 3.5 illustrates resistance network for the two parallel layers MEMS structure heat flow, thus utilizing electrical current flow analogy, we get

$$Q_{cond} = \frac{T(x)_1 - T(x)_2}{R_{eff}} \tag{3.23}$$

Since the resistances are in parallel

$\frac{1}{R_{eff}} = \frac{1}{R_{vox}} + \frac{1}{R_{Si3N4}}$ This lead to $R_{eff} = \frac{R_{Vox}\ .\ R_{Si3N4}}{R_{vox} + R_{Si3N4}}$ (3.24)

The effect of the spreading resistance between the plate and arm for two-dimensional channels has also been considered for the boundary conditions. Spreading and constriction resistances have been analyzed and formulated for various geometries and boundary conditions [32].

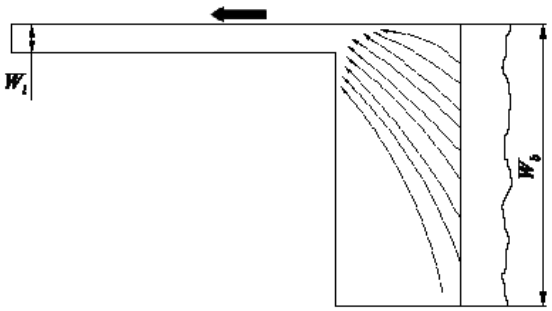

Figure 3.6: Spreading resistance when heat flows from the central microplate to the legs

For a long two-dimensional channel with thermal conductivity *k*, the steady state spreading resistance for a strip of width of w_l at one end and width of w_b at the other end as shown in Figure 3.6 is computed as [19]

$$R_s = \frac{1}{2\pi tk}\left((\varepsilon) + \frac{1}{\varepsilon}\right) ln\left(\frac{1+\varepsilon}{1-\varepsilon}\right) 2ln\left(\frac{1-\varepsilon^2}{4\varepsilon}\right) \tag{3.25}$$

where *t* is the thickness of the device , *k* is the thermal conductivity, and ε is the ratio of widths, expressed as:

$$\varepsilon = \frac{w_p}{w_l} \tag{3.26}$$

It should be noted that each layer in the model act as a heat source, although some of the layers have much higher electrical resistivity (e.g., silicon nitride). Considering homogenous heat generation and using (3.11), the total joule heat generated in the element (q_{JH}) can be found from the summation of the heat generated in each layer with current density j_i resistivity $\varphi\big(T(x)\big)$ as,

$$Q_{JH} = \sum_i j^2{}_i \, \varphi\big(T(x)\big)(V_{ele})_i \tag{3.27}$$

Equation (3.27) for the differential element at the microplate section with vanadium oxide and silicon nitride can be written as

$$Q_{JH} = \left(j^2_{Vox}\varphi_{vox}\big(T(x)\big)(V_{ele})_{vox}\right) + \left(j^2_{Si3N4}\varphi_{Si3N4}\big(T(x)\big)(V_{ele})_{Si3N4}\right) \tag{3.28}$$

$$= \left(j_{VOx}^2 \varphi_{vox}(T(x)) A_{vox} \Delta x\right) + \left(j_{Si3N4}^2 \varphi_{Si3N4}(T(x)) A_{Si3N4} \Delta x\right)$$

where j_{VOx} and j_{Si3N4} is the current density in vanadium oxide and silicon nitride layers

In order to calculate the heat generation in each layers we need to know the current passing through these layers As shown in Figure 3.7, the multilayered structure can be expressed as an equivalent electrical circuit with two resistors in parallel. The current in each layer is then given by,

$$I_{app} = I_{VOx} + I_{Si3N4}, \quad \frac{1}{R_T} = \frac{1}{R_{VOx}} + \frac{1}{R_{Si3N4}} \text{ and } \frac{I_{VOx}}{I_{Si3N4}} = \frac{R_{Si3N4}}{R_{VOx}} \tag{3.29.a}$$

$$R_{VOx} = \frac{l_l \varphi_{VOx}}{A_{VOx}} \; and \; R_{Si3N4} = \frac{l_l \varphi_{Si3N4}}{A_{Si3N4}} \tag{3.29.b}$$

$$\frac{A_{vox} . j_{VOx}}{A_{Si3N4} . j_{Si3N4}} = \frac{R_{Si3N4}/A_{Si3N4}}{R_{VOx}/A_{vox}} \tag{3.30}$$

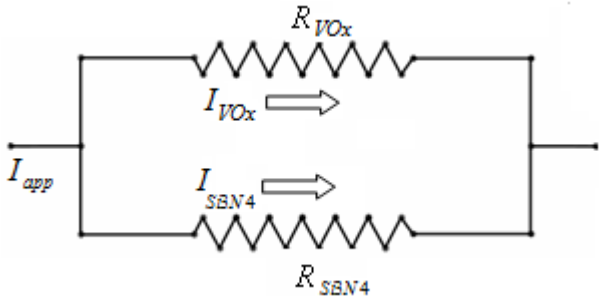

Figure 3.7: Equivalent circuit with resistors connected in parallel for the multilayered lag of the Thin Single stage structure.

Replacing the resistance of the two layers given in Eq. (3.29.b) into Eq. (3.29.a) we computed the current passing through each layers as :

$$I_{VOx} = I_{app} \frac{R_{Si3N4}}{R_{VOx} + R_{Si3N4}} = I_{app} \frac{\varphi_{Si3N4}/R_{Si3N4}}{\varphi_{VOx}/R_{VOx} + \varphi_{Si3N4}/R_{Si3N4}} \tag{3.31}$$

$$I_{Si3N4} = I_{app}\left(1 - \frac{R_{Si3N4}}{R_{VOx} + R_{Si3N4}}\right) = I_{app}\left(1 - \frac{\varphi_{Si3N4}/R_{Si3N4}}{\varphi_{VOx}/R_{VOx} + \varphi_{Si3N4}/R_{Si3N4}}\right) \quad (3.32)$$

where I_{app}, I_{VOx} and I_{Si3N4} are the applied current, the current passing through Vanadium oxide and the current passing through Si_3N_4, respectively. Although the above module account heat generated in multilayer conductor, for Thin Single Stage device, I_{Si3N4} is negligible (I_{Si3N4} = 9.0039e-19 μA) when 10 μA applied to the device. The resistivity of VO_x is related to temperature with a linear relationship controlled by a temperature coefficient of resistance α(-2% for VO_x) and taken in to account for the plate area where Vanadium oxide exist.

$$\varphi(T) = \varphi_{VOx}\big(1 + \alpha(T(x) - T_s)\big) \quad (3.33)$$

At steady state, the multilayered conduction is given by,

$$Q_{cond} = \frac{k_{eff}A_c}{\Delta x}(T(x)_{i-1} - T(x)_i) = \left(\frac{k_{VOx}A_{VOx}}{\Delta x}(T(x)_{i-1} - T(x)_i)\right) + \left(\frac{k_{Si3N4}A_{Si3N4}}{\Delta x}(T(x)_{i-1} - T(x)_i)\right) \quad (3.34)$$

$$= \left(\frac{(T(x)_{i-1} - T(x)_i)}{\Delta x}\right)(k_{VOx}A_{VOx} + k_{Si3N4}A_{Si3N4})$$

where A_{VOx} and A_{Si3N4} are cross-sectional area of vanadium oxide and silicon nitride layers, respectively,

Δx is the length of the differential element in the direction of heat transfer,

k_{VOx} and k_{Si3N4} the thermal conductivity of vanadium oxide and silicon nitride at the given cross section area, respectively.

Due to the small gap between the microplate and the substrate, effect of conduction via air to the substrate need to considered. Therefore, the shape factor of the different section used to construct the microbolometer has to be defined. The shape factor, *S*, described in Eq. (3.35) incorporates the thermal conduction from the bottom and both vertical sides of the leg and the plate structure to the effective projected area of the substrate (Figure 3.8).

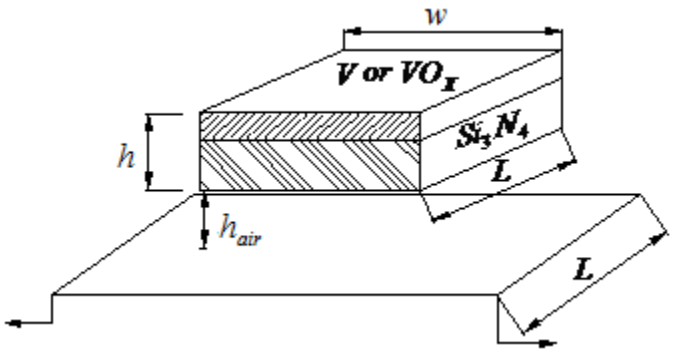

Figure 3.8: Cross sectional dimensions used in the calculation of the shape factor

For a beam-shaped microstructure the shape factor can be expressed as [12]:

$$S = \frac{t_p}{w}\left(\frac{2t_{air}}{h} + 1\right) + 1 \tag{3.35}$$

where t_p is the sum thickness of vanadium oxide and silicon nitride used to construct the element of leg, *w* is the width and t_{air} is the air gap between the leg and the substrate. This gap works as a quarter wavelength cavity, which sets the detector spectral response. The path of the heat from the microplate to the substrate passes through the air and aluminums reflector. These layers act as three thermal paths in series, with overall thermal conductivity, k_{bottom}:

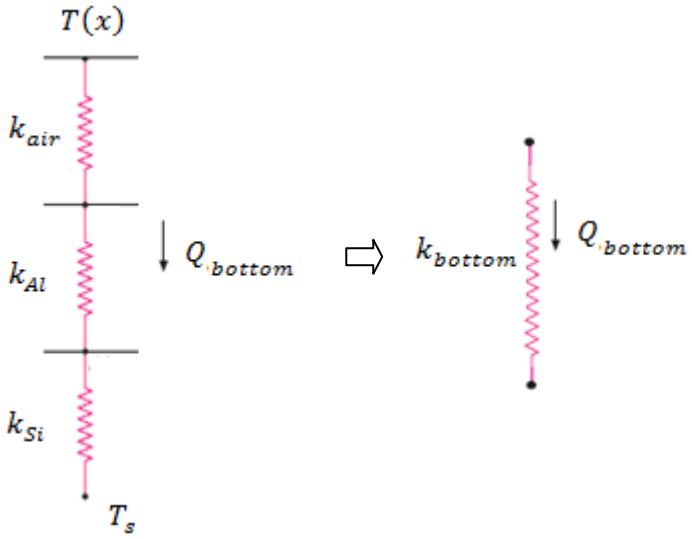

Figure 3.9: Series connection of the electrical resistance for the microplate to the substrate

$$\frac{1}{k_{bottom}} = \frac{t_{air}}{k_{air}} + \frac{t_{Al}}{k_{Al}} + \frac{t_{Si}}{k_{Si}}$$

$$k_{bottom} = \frac{1}{\left(\frac{t_{air}}{k_{air}} + \frac{t_{Al}}{k_{Al}} + \frac{t_{Si}}{k_{Si}}\right)} \tag{3.36}$$

where t_{Al} is the thickness of the Aluminums reflector layer, t_S is thickness of substrate, and k_{air}, k_{Al}, and k_S are the thermal conductivities of air, Aluminums and substrate, respectively. Finally, assuming the radiation effect is small comparing to the other heat transfer mechanisms, for steady state:

$$\begin{aligned}\left(j_{VOx}{}^2\left(\varphi_{VOx}(T(x))\right)A_{VOx}dx + j_{Si3N4}{}^2(\varphi_{Si3N4})A_{Si3N4}dx\right) \\ -(k_{VOx}A_{VOx} + k_{Si3N4}A_{Si3N4})\left.\frac{dT(x)}{dx}\right|_x \\ +(k_{VOx}A_{VOx} + k_{Si3N4}A_{Si3N4})\left.\frac{dT(x)}{dx}\right|_{\Delta x+x} - hw\,(T(x)-T_s)dx \\ -Swk_{bottom}\,(T(x)-T_s)dx = 0\end{aligned} \tag{3.37}$$

where j_{VOx} and j_{Si3N4} are the current density in vanadium oxide and silicon nitride layers respectively

Dividing (3.30) by $(k_{VOx}A_{VOx} + k_{Si3N4}A_{Si3N4})$ and taking the limit as $dx \rightarrow 0$, the governing equation for heat transfer is written as:

$$\frac{d^2T(x)}{dx^2} + \frac{\left(j_{VOx}{}^2\left(\varphi_{VOx}(T(x))\right)A_{VOx} + j_{Si3N4}{}^2(\varphi_{Si3N4})A_{Si3N4}\right)}{k_{VOx}A_{VOx} + k_{Si3N4}A_{Si3N4}} - \frac{w(T(x) - T_s)(Sk_{bottom} + h)}{k_{VOx}A_{VOx} + k_{Si3N4}A_{Si3N4}} = 0 \tag{3.38}$$

$$\begin{aligned}\frac{d^2T(x)}{dx^2} &+ \frac{\left(j_{VOx}{}^2\left(\varphi_{VOx}(T(x))\right)A_{VOx}\alpha_{VOx}(T(x) - T_s)\right)}{k_{VOx}A_{VOx} + k_{Si3N4}A_{Si3N4}} \\ &+ \frac{\left(j_{VOx}{}^2(\varphi_{VOx})A_{VOx}\right) + \left(j_{Si3N4}{}^2(\varphi_{Si3N4})A_{Si3N4}\right)}{k_{VOx}A_{VOx} + k_{Si3N4}A_{Si3N4}} \\ &- \frac{w(T(x) - T_s)(Sk_{bottom} + h)}{k_{VOx}A_{VOx} + k_{Si3N4}A_{Si3N4}} = 0\end{aligned} \tag{3.39}$$

Equation 3.39 has a general form:

$$\frac{d^2\psi(x)}{dx^2} - \beta^2\psi(x) = 0 \tag{3.40}$$

where:

$$\beta^2 = \frac{w(Sk_{bottom} + h) - j_{VOx}{}^2(\varphi_{VOx})A_{VOx}\alpha_{VOx}}{k_{VOx}A_{VOx} + k_{Si3N4}A_{Si3N4}} \tag{3.41}$$

$$\psi(x) = T(x) - T_s - \frac{\left(j_{VOx}{}^2\left(\varphi_{VOx}\right)A_{VOx}\right) + \left(j_{Si3N4}{}^2\left(\varphi_{Si3N4}\right)A_{Si3N4}\right)}{\beta^2(k_{VOx}A_{VOx} + k_{Si3N4}A_{Si3N4})} \tag{3.42}$$

Two form of differential equation will be considered depending on β^2 sign

Case A: second order differential equation with the form

$$\frac{d^2\psi(x)}{dx^2} - \beta^2\psi(x) = 0 \tag{3.43}$$

TCR value for a given microbolometer design can be positive or negative which makes the value of β^2 like wise

Assuming β^2 is positive the solution for the above differential equation is

$$\psi(x) = C_i e^{\beta x} + C_j e^{-\beta x} \tag{3.44}$$

where: C_i and C_j are constants that need to be determined from the boundary conditions

Case B: second order differential equation with the form

$$\frac{d^2\psi(x)}{dx^2} + \beta^2\psi(x) = 0 \tag{3.45}$$

Assuming β^2 is positive the solution for the above differential equation is

$$\psi(x) = C_i sin(\beta x) + C_j cos(\beta x) \tag{3.46}$$

Generally, for electro-thermal analysis we studied have the first form of solutions in air or vacuum environment depending. Therefore, the solution to the second-order differential Eq. (3.45) is written as:

$$T(x) = T_s + \frac{j_{vox}^2 \varphi_{vox} A_{VOx} + j_{Si3N4}^2 \varphi_{Si3N4} A_{Si3N4}}{\beta^2 (k_{VOx} A_{VOx} + k_{Si3N4} A_{Si3N4})} + C_i e^{\beta x} + C_j e^{-\beta x} \tag{3.47}$$

Equation (3.47) describes the temperature distribution of the Thin Single Stage microbolometer in an air environment. To obtain the temperature distribution in vacuum, the bottom air conduction and heat convection will be neglected.

To assess the functionality of the analytical solution given by Eq. (3. 47), this report considers two microbolometer geometries. These two microbolometer geometries will help us understand the effect physical parameters and different geometries on the temperature distribution of the device. The first one corresponds to the actual Thin Single Stage microbolometer and it is shown schematically in Figure 3.10. The second one has a simpler geometry and it is shown in Figure 3.10. We have called this simpler geometry the three-region microbolometer. The three region design is the same as the test device used in our experiment. Both microbolometer geometries are divided into regions based on their geometries and material properties. Hence, the Thin Single Stage microbolometer has been divided into five regions and the simpler geometry into three

(refer to Figures 3.10 and 3.11). The regions of the two different microbolometer geometries are defined as follows:

a. For the Thin Single Stage device geometry

Region I – leg (composed of V & Si_3N_4)

Region II – plate absorber area (plate with V & Si_3N_4)

Region III – plate pixel area (plate with VO_x & Si_3N_4)

Region IV – plate absorber area (plate with V & Si_3N_4)

Region V – leg (composed of V & Si_3N_4)

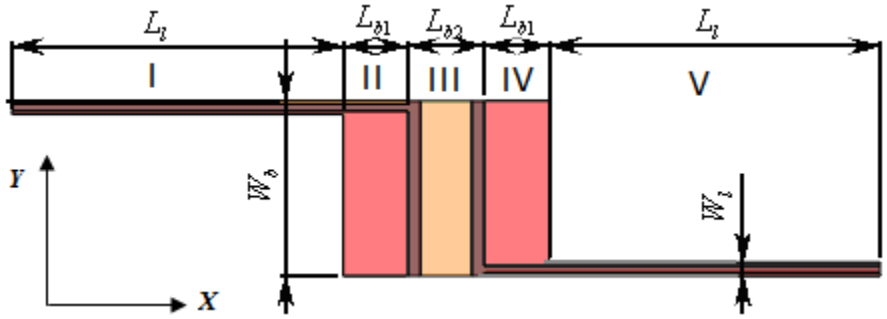

Figure 3.10: Top view of a Thin Single Stage microbolometer with five regions.

b. For the three-region geometry

Region I – leg (composed of V & Si_3N_4)

Region II – plate area (plate with VO_x & Si_3N_4)

Region III – leg (plate with V & Si3N4)

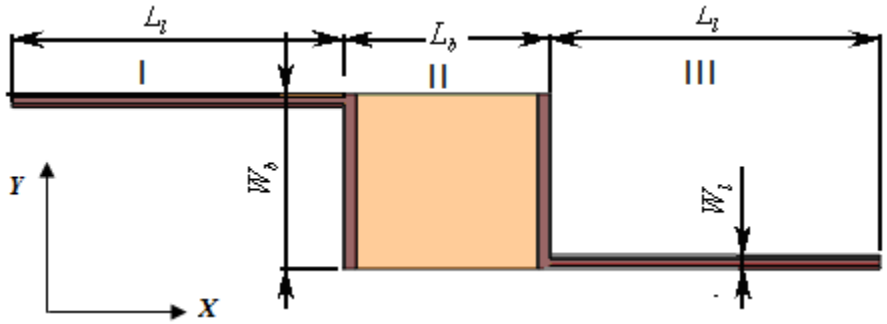

Figure 3.11: Top view of a Thin Single Stage microbolometer with three regions

Two sets of boundary conditions are used across the contact points of the legs and plate to solve for the integration constants, C_i & C_j in Eq. (3.47). The substrate is assumed to be an ideal heat sink; hence the end of the arm will have the same temperature as that of substrate. Therefore, two sets of boundary conditions are used to solve the constant. The temperature and heat conduction are continuous across the joint points and the temperature at the connection of the arm to the substrate is constant.

$$T(0) = T\left(2l_l + l_p\right) \tag{3.48}$$

The interface between regions I and II is assumed to have a constant contact resistance, which means that the heat flow is continuous but the temperature is discontinuous. In this case, the boundary condition describing the continuous heat flow at the interface can be written as:

$$k_{l\_eff}\frac{dT_l(x)}{dx} = k_{b\_eff}\frac{dT_b(x)}{dx} \tag{3.49}$$

where k_{l_eff} and k_{p_eff} are the effective thermal conductivity of the leg and microplate section, respectively

$T_l(x)$ and $T_p(x)$ are the temperature of the leg and microplate at the contact point, respectively

The effect of spreading resistance between the plate and arm for two-dimensional channels has also been considered. In this case, the rate of heat conduction will be the same as (3.49). However, due to the spreading resistance, the temperature will be different at the joint and the discontinuity in the temperature at the interface can be expressed as:

$$k_{l\_eff}\frac{dT_l(x)}{dx} = \frac{1}{R_s t\, w_p}\left(T_l(x) - T_p(x)\right) \tag{3.50}$$

where R_s is the constriction resistance, t is the thickness of the layer and w_p is the width of the microplate

Using the first set of boundary conditions, the following set of algebraic equations are obtained to calculate the constants C_i (i = 1 to 10) for the Thin Single Stage microbolometer:

$$\begin{bmatrix} 1 & 1 & 0 & 0 & 0 & 0 & 0 & 0 & 0 & 0 \\ e^{\beta_1 L_1} & e^{-\beta_1 L_1} & -e^{\beta_2 L_1} & -e^{-\beta_2 L_1} & 0 & 0 & 0 & 0 & 0 & 0 \\ e^{\beta L_{11}} & -e^{-\beta_1 L_1} & -\chi_{21} e^{\beta_2 L_1} & \chi e^{\beta_2 L_1} & 0 & 0 & 0 & 0 & 0 & 0 \\ 0 & 0 & e^{\beta_2 L_2} & e^{-\beta_2 L_2} & -e^{\beta_3 L_2} & -e^{-\beta_3 L_2} & 0 & 0 & 0 & 0 \\ 0 & 0 & e^{\beta_2 L_2} & -e^{-\beta_2 L_2} & -\chi_{32} e^{\beta_3 L_2} & \chi_{32} e^{-\beta_3 L_2} & 0 & 0 & 0 & 0 \\ 0 & 0 & 0 & 0 & e^{\beta_3 L_3} & e^{-\beta_3 L_3} & -e^{\beta_4 L_3} & -e^{-\beta_4 L_3} & 0 & 0 \\ 0 & 0 & 0 & 0 & \chi_{43} e^{\beta_3 L_3} & -\chi_{43} e^{-\beta_3 L_3} & -e^{\beta_4 L_3} & e^{-\beta_4 L_3} & 0 & 0 \\ 0 & 0 & 0 & 0 & 0 & 0 & e^{\beta_4 L_4} & e^{-\beta_4 L_4} & -e^{\beta_5 L_4} & -e^{-\beta_5 L_4} \\ 0 & 0 & 0 & 0 & 0 & 0 & \chi_{54} e^{\beta_4 L_4} & -\chi_{54} e^{\beta_4 L_4} & -e^{\beta_5 L_4} & e^{-\beta_5 L_4} \\ 0 & 0 & 0 & 0 & 0 & 0 & 0 & 0 & e^{\beta_5 L_5} & e^{-\beta_5 L_5} \end{bmatrix} \begin{bmatrix} C_1 \\ C_2 \\ C_3 \\ C_4 \\ C_5 \\ C_6 \\ C_7 \\ C_8 \\ C_9 \\ C_{10} \end{bmatrix} = \begin{bmatrix} T_S - T_1 \\ T_2 - T_1 \\ 0 \\ T_3 - T_2 \\ 0 \\ T_4 - T_3 \\ 0 \\ T_5 - T_4 \\ 0 \\ T_S - T_5 \end{bmatrix} \quad (3.51)$$

The length terms in the Eq. (3.51) represent the contact points of the different regions shown in Figure 3.10 and can be given as

$$\begin{aligned} L_1 &= L_l, \\ L_2 &= L_l + L_{p1}; \\ L_3 &= L_l + L_{p1} + L_{p2}; \\ L_4 &= L_l + 2L_{p1} + L_{p2}; \\ L_5 &= 2L_l + 2L_{p1} + L_{p2}; \\ \chi_{x,x-1} &= w_x \beta_x / w_{x-1} \beta_{x-1}. \end{aligned} \quad (3.52)$$

After computing the constant C_i for each region the temperature as a function of position can be simulated using Eq (3.47).

3.4 Numerical Methods and Simulation

In the previous sections we derived analytical methods for solving the general electro-thermal differential equations. By solving the second order differential equation, we were able to find an explicit formula for the solution of electro-thermal coupling models for microbolometer performance and reliability analysis. Using these analytical solutions, we can learn a lot about the quantitative and qualitative behaviour of the microbolometer and other MEMS device. This

qualitative insight will also be useful in understanding the effect of different parameters, including material properties and device geometry, on the thermal distribution. However, Electro-thermal modeling for Thin Single Stage microbolometer which accounts the effect of IR energy, transient condition and radiation heat transfer mechanisms along with spreading resistance between the plates cannot be solved with analytical methods. In order get a comprehensive electro-thermal model for the microbolometer to define its performance and reliability, these terms have to be incorporated. Therefore, in this section we will turn our attention to numerical methods for solving such problems.

There are several methods associated with numerical methods, which partitions the arbitrary computational domain into smaller units. These include the finite difference method (FDM), the finite volume method (FVM), the finite element method (FEM) and the boundary element method (BEM). Although each of these methods has their own advantage for non-linear equations, in this section we will focus on finite difference schemes. This is because finite difference method (FDM) are more appropriate for the type of problem that we want to address and can easily be modified for a range of microbolometer design parameters. This includes the different design shape, temperature dependent material properties and effect of infrared power for thermal analysis. The FDM model approach is also useful to incorporate the performance parameters of the device along with the electro-thermal model.

For Thin Single Stage microbolometer, it was assumed that the temperature profile at steady state is uniform through the thickness, thus a two-dimensional (2D) heat analysis is implemented. This assumption is supported by the preliminary finite element analysis developed for the model as shown in Figure 3.12. The finite difference method begins with the discretization of space and time such that there are an integer number of points in space and an integer number of times at which we calculate the field variable, in this case the temperature.

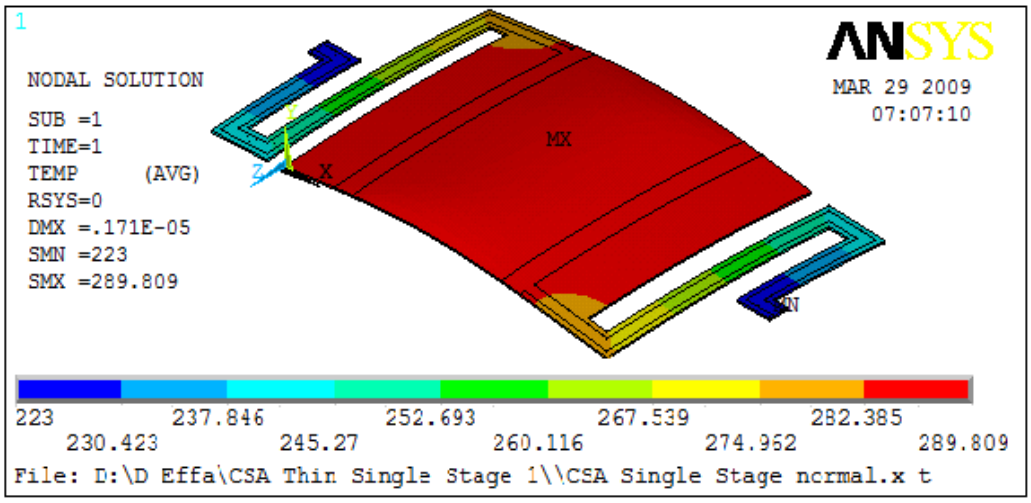

Figure 3.12: Temperature distribution (K) for the Thin Single Stage microbolometer for a DC bias current load of 10 μA without absorber

Considering the heat transfer between all neighbouring nodes for this method, the solution region which is representing the Thin Single Stage microbolometer is divided into small regions or meshes of Δx and Δy in the *x* and *y* directions, respectively. The resulting approximation grid is shown schematically in Figure 3.13. Based on this discretization a general two dimensional equation is developed with equal spacing of the points x_i & y_j with intervals of size $\Delta x = x_{i+1} - x_i$, $\Delta y = y_{j+1} - y_i$ and equal spacing of the time steps t_n at intervals of $\Delta t = t_{k+1} - t_k$.

To determine the actual size of interval (element size), let $M \geq 1$ and $N \geq 1$ be a given integer, and define the grid spacing in the *x*-direction and *y*-direction by

$$\Delta x = L_x/(M+1)$$
$$\Delta y = L_y/(N+1) \tag{3.53}$$

where L_x and L_y is the length and width of the microbolometer regions respectively.

Then, the grid points in the x-direction are given by $x_i = i\Delta x$ for i = 0, 1... M + 1 and in the y-direction as $y_i = i\Delta y$ for i = 0, 1... N + 1. Similarly, we define $t_k = k\Delta t$ for integers k ≥ 0, where Δt denotes the time step. The temperature can be approximated using a numerical method for

each discrete location with $T\ (x_m, y_n, t_i)$ at node (m, n) and time t_i. We will also denote this temperature value with $T^i_{m,n}$ at this discrete location. This method simplifies the system considerably, since instead of tracking a smooth function at an infinite number of points, one just deals with a finite number of temperature values at a finite number of locations and times.

Figure 3.13 shows the discredited Thin Single Stage microbolometer and the intersections of grid lines are the nodal points where temperature is calculated iteratively. The temperature is considered to be discrete value at respective coordinate, $T\ (x_m, y_n, t_i)$. Although half of the device can be modeled due to the symmetric nature of the structure, in this analysis the full model is used to develop the FDM model.

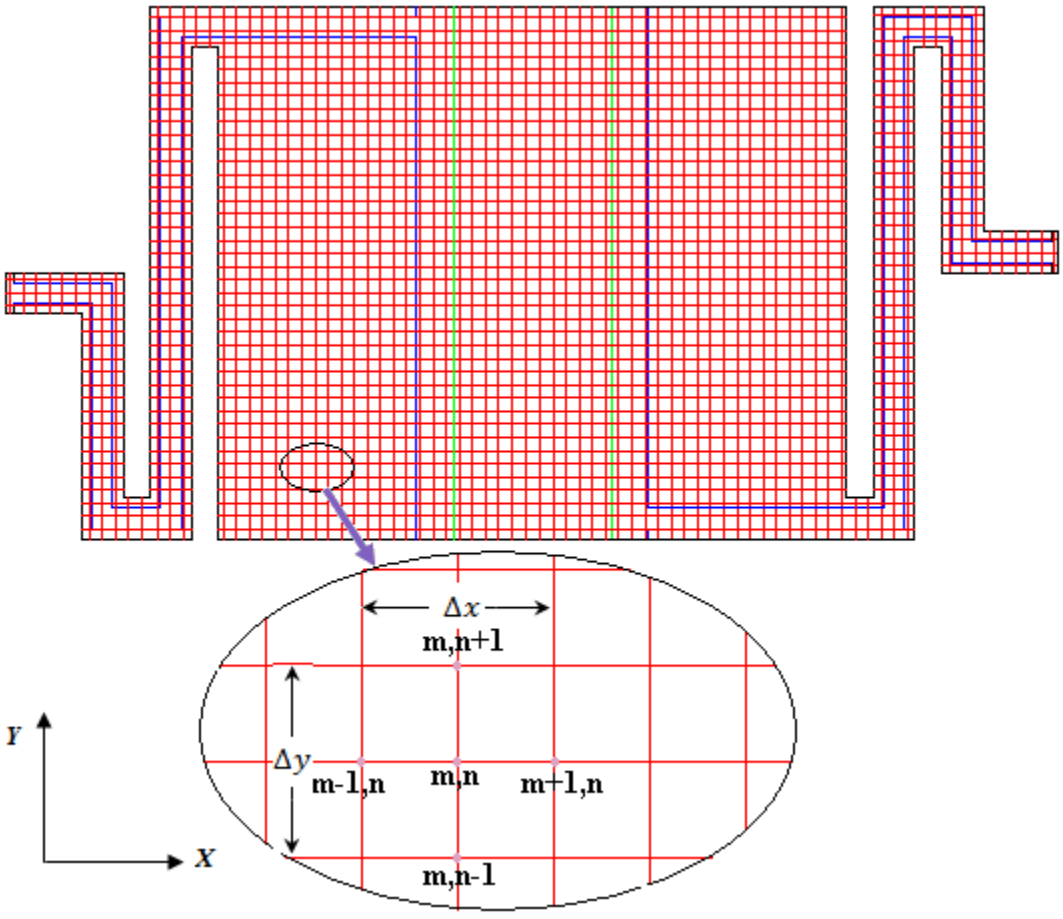

Figure 3.13: The schematic of the Thin Single Stage microbolometer used in finite difference modeling. The sample grid lines are drawn with same spacing as the actual analysis.

Similar to the analytical model studied, Thin Single Stage microbolometer is divided to five sub-regions based on its geometry and material compositions as shown in Figure 3.14 (a). Each of this part is subdivided based on the different material composition. For example the leg part is subdivided in to three regions, as shown in Figure 3.14 (b). The leg of the microbolometer is taken as a straight arm without a significant loss of generality. The heat equation at a single node (m, n) can be found by applying an energy balance to a control volume around each element (node). When solved, the set of equations for all elements produces the nodal temperatures throughout the body.

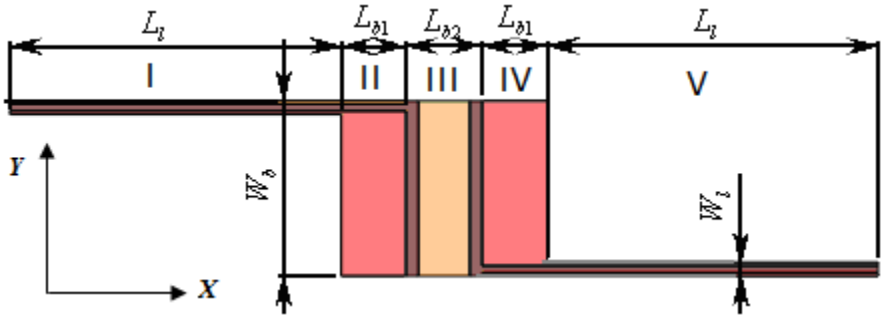

(a) Thin Single Stage microbolometer

(b)Region I and V

Figure 3.14: (a) Top view of a Thin Single Stage microbolometer with five regions (b) the leg part .

Applying the energy balance for control volume, as shown in Figure 3.15, of each node, the following state equation is obtained

$$Q_{st} = Q_{IR} + Q_{JH} + \left(Q_{cond,air} + Q_{cond,leg} + Q_{cov}\right) + Q_{rad} \tag{3.54}$$

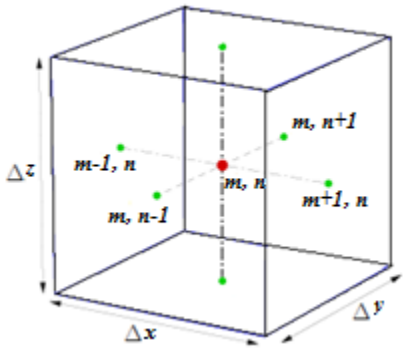

Figure 3.15: The 3D Control volume in Cartesian coordinates.

Replacing each element with appropriate terms Eq. (3.53) can be rewritten as

$$C_{total}\frac{dT(x,y,t)}{dt} = (P_{abs}).V_{ele} + \left(I_{app}^2 R\big((x,y,t)\big)\right).V_{ele} - G_{th}\big((x,y,t) - T_{sub}\big) - \varepsilon\sigma A_s(T(x,y,t)^4 - T_{ambient}^4) \quad (3.55)$$

The solution function $T\,(x_m, y_n, t_i)$ of this differential equation describes the temperature of Thin Single Stage microbolometer of different cross sectional area, at nodal position (x_i, y_j) and at any time $t_k \geq 0$. In the simplest case, we may assume that $T\,(x_m, y_n, t_i)$ is a constant function with its value somehow in the range defined by the initial boundary conditions. When we rewrite Eq. (3.54) for each node, the following state equation is obtained for the node (m, n) element which is the most general form for FDM formulation

$$Q_{m,n}^{st} = Q_{m,n}^{IR} + Q_{m,n}^{JH} + \left(Q_{m-1,n}^{Cond\_leg} + Q_{m+1,n}^{Cond\_leg} + Q_{m,n+1}^{Cond\_leg} + Q_{m,n-1}^{Cond\_leg}\right) + Q_{m,n}^{cond,air} + Q_{m,n}^{cov} + Q_{m,n}^{rad} \quad (3.56)$$

where $Q_{m,n}^{st}$ – Net rate of change of the internal energy storage within the element

$Q_{m,n}^{JH}$ – Rate of energy generated in element (m, n) by joule heating

$Q_{m,n}^{IR}$ – Infrared Energy absorbed in element (m, n)

$Q_{m,n}^{cond,air}$ – Conduction to the substrate via air

$Q_{m,n}^{cov}$ – Convection to the surroundings

$Q_{m,n}^{rad}$ – Radiation to the surroundings

$Q_{m-1,n}^{Cond\_leg}$, $Q_{m+1,n}^{Cond\_leg}$, $Q_{m,n+1}^{Cond\_leg}$, $Q_{m,n-1}^{Cond\_leg}$ – Conduction to element (m, n) *from* adjoining elements

By replacing the size of each elements and heat transfer mechanism for Eq. (3.56) for the node element the following equation can be developed

$$\begin{aligned}\rho c_{eff}\Delta x\Delta y\Delta z\left(\frac{dT(x,y,t)}{dt}\right) &= (P_{abs})\Delta x\Delta y\Delta z + \dot{q}_{m,n}^{JH}\Delta x\Delta y\Delta z + k_{eff}^{left}\Delta y\Delta z\left(\frac{dT(x,y,t)}{dx}\right) \\ &+ k_{eff}^{right}\Delta y\Delta z\left(\frac{dT(x,y,t)}{dx}\right) + k_{eff}^{up}\Delta x\Delta z\left(\frac{dT(x,y,t)}{dy}\right) \\ &+ k_{eff}^{down}\Delta x\Delta z\left(\frac{dT(x,y,t)}{dy}\right) + Sk_{bottom}\left(T_s - T_{m,n}^{i}\right)\Delta x\Delta y \\ &+ h_{m,n}\left(T_s - T_{m,n}^{t}\right)\Delta x\Delta y + \varepsilon\sigma\Delta x\Delta y\left[T_{m,n}^4 - T_s^4\right]\end{aligned} \tag{3.57}$$

Based on FDM discretization and approximation of the function, we write the following approximations of its derivatives in time and space

$$\left.\frac{\partial T}{\partial t}\right|_{x_i,t_{n+1}} \cong \frac{T_{i,n+1} - T_{i,n}}{\Delta t} \tag{3.58}$$

$$\left.\frac{\partial T}{\partial x}\right|_{x_i+1,t_n} \cong \frac{T_{i+1,n} - T_{i,n}}{\Delta x} \tag{3.59}$$

$$\left.\frac{\partial T}{\partial y}\right|_{y_i+1,t_n} \cong \frac{T_{i+1,n} - T_{i,n}}{\Delta y}$$

The differential equation $\left(\frac{dT}{dx}\right)$ and $\left(\frac{dT}{dt}\right)$ will be replaced by a finite difference equation in the solution process. The forward Euler algorithm, also called explicit time stepping, uses the field values of only the previous time step to calculate those of the next. In this case, the spatial derivatives will be evaluated at time step *n* and the time derivatives at *k+1*. With this method we

can calculate the approximated values $T(x_i, y_j, t_k)$ by proceeding from time point t_{k-1} to time pointt_k, if approximate values at time t_{k-1} are already known for all positions(x_i, y_j). This algorithm is efficient, in that each new temperature at time step *k+1* is calculated independently, so it does not require simultaneous solution of equations. When the finite difference approximations, Eq. (3.58) and (3.59), inserted into Eq. (3.57), for 2-D heat conduction, the explicit-form FDM modeling of the heat equation becomes

$$\begin{aligned}\rho C_{eff}\Delta x\Delta y\Delta z\left(\frac{T_{m,n}^{i+1}-T_{m,n}^{i}}{\Delta t}\right)&\\ =\dot{q}_{m,n}^{IR}\Delta x\Delta y\Delta z\ +\dot{q}_{m,n}^{JH}\Delta x\Delta y\Delta z\ +\ k_{eff}^{left}\Delta y\Delta z\left(\frac{T_{m-1,n}^{i}-T_{m,n}^{i}}{\Delta x}\right)&\\ +k_{eff}^{right}\Delta y\Delta z\left(\frac{T_{m+1,n}^{i}-T_{m,n}^{i}}{\Delta x}\right)+k_{eff}^{up}\Delta x\Delta z\left(\frac{T_{m,n+1}^{i}-T_{m,n}^{i}}{\Delta y}\right)&\\ +k_{eff}^{down}\Delta x\Delta z\left(\frac{T_{m,n-1}^{i}-T_{m,n}^{i}}{\Delta y}\right)+Sk_{bottom}(T_s-T_{m,n}^{i})\Delta x\Delta y&\\ +h_{m,n}(T_s-T_{m,n}^{t})\Delta x\Delta y+\varepsilon\sigma\Delta x\Delta y[T_{m,n}^{4}-T_s^{4}]&\end{aligned} \tag{3.60}$$

where $k_{eff}^{top}, k_{eff}^{left}, k_{eff}^{right}, k_{eff}^{down}$ is the thermal conduction coefficient,

C_{eff} - is the effective specific heat,

ρ - is the density and

h - is the convection film coefficient.

$\Delta x, \Delta y, \Delta z$ are the dimensional increments in rectangular coordinate system.

The various energy terms in Eq. (3.60) can be determined from physical relationships. Joule heating can be calculated from the input current and material resistivity, $\varphi\ (T(x,y))$, as

$$Q_{m,n}=\sum_{l=1}^{n}{j_l}^2\varphi_l\left(T(x_i,y_j)\right)\Delta v_{m,n}^{l} \tag{3.61}$$

where $Q_{m,n}$ is the total heat generated in each layers

j_l - is the current density input to the system and

$\Delta v_{m,n}^{l}$- is the element volume

$\varphi_l\left(T(x_i, y_j)\right)$ is the resistivity of the l[th] material layer

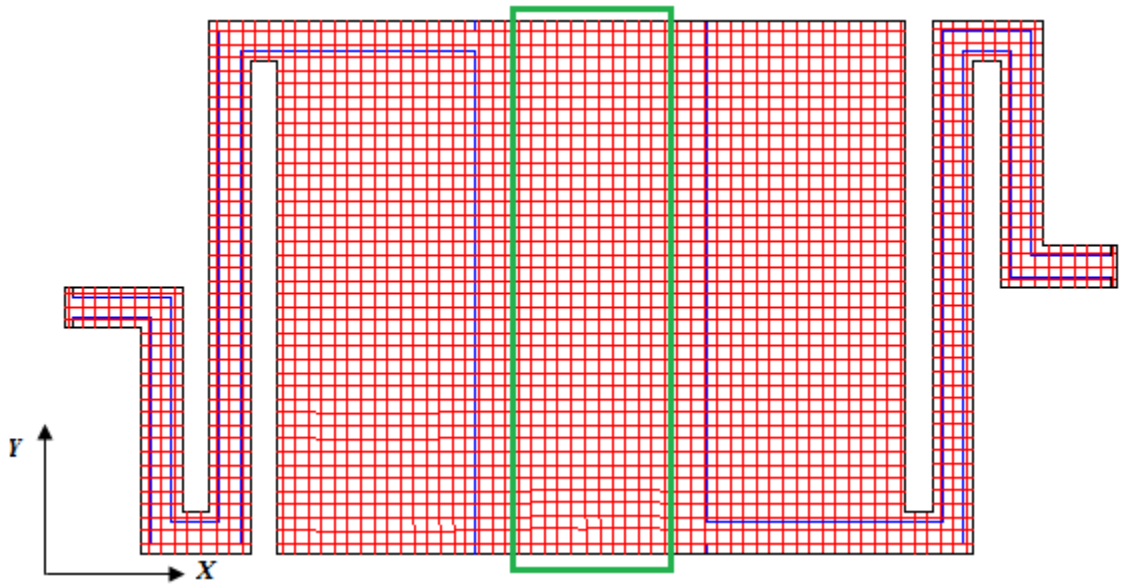

Figure 3.15: Sensing area (nodes in the green box) of the microbolometer

For Thin Single Stage microbolometer multilayer structure the heat generated in different area of the microbolometer is different depending on the material composition. For instance nodes around the sensing element will generate heat from vanadium oxide and silicon nitride layers as in Eq. (3.62)

$$Q_{m,n} = j_{VOx}^2 \varphi_{VOx}(T) A_{VOx} \Delta x + j_{Si3N4}^2 \varphi_{Si3N4}(T) A_{Si3N4} \Delta x \tag{3.62}$$

$$A_{VOx} = \Delta y . t_{VOx} \;\; \& \;\; A_{Si3N4} = \Delta y . t_{Si3N4}$$

where t_{VOx} and t_{Si3N4} is the thickness of the vanadium oxide silicon nitride respectively

The numerical method is able to incorporate the infrared single heat (q_{IR}) source in the model. Usually, the incident IR signal is modulated by using a mechanical chopper. In this case, energy source from IR (q_{IR}) per unit volume can be expressed as

$$Q_{IR} = \left(P_{abs} e^{j\omega t}\right) V_{ele} \tag{3.63}$$

where P_{abs} is the absorbed IR energy per unit volume, it will be discussed in chapter four,

ω is the modulation frequency of the microbolometer

η is the coupling efficiency, which is defined as the ratio of the absorbed radiation to the total incident radiation,

Due to small air gap under the microplate the effect of conduction is more significant than convection. This concept is explained in the previous section and the heat transfer for the nodal element model is described as

$$Q_{m,n}^{Cond\_air} = \frac{SA_s}{R_{bottom}} \left(T_{m,n}(t) - T_s\right) \tag{3.64}$$

where T_s - Temperature of the substrate (assumed constant)

$T_{m,n}(t)$- Temperature of the (m, n) node at the t^{th} time increment

A_s - the area of the element's surface that faces the substrate

S - is shape factor defined in the previous analysis, and

R_{bottom} - is resistivity of layers defined in the previous analysis. Over the bond pads, the layer representing the air gap is removed and h_{air} is set to zero

Conduction of heat between elements, such as elements *i-1*, i, and *i+1*, is modeled by the expression

$$\begin{aligned} Q_{m-1,n}^{cond,leg} &= \frac{k_{eff} A_x}{\Delta x}\left[T_{m-1,n}(t) - T_{m,n}(t)\right] \quad Q_{m+1,n}^{cond,leg} = \frac{k_{eff} A_x}{\Delta x}\left[T_{m+1,n}(t) - T_{m,n}(t)\right] \\ Q_{m,n-1}^{cond,leg} &= \frac{k_{eff} A_x}{\Delta y}\left[T_{m,n-1}(t) - T_{m,n}(t)\right] \quad Q_{m,n+1}^{cond,leg} = \frac{k_{eff} A_x}{\Delta y}\left[T_{m,n+1}(t) - T_{m,n}(t)\right] \end{aligned} \tag{3.65}$$

where A_x and A_y is the cross-sectional area of the element in x and y direction respectively

Δx *and* Δy is the length of the element in x and y direction and

k_{eff} is the effective thermal conductivity of the cross section.

The multilayered structure of the microplate is studied as a lumped model, where the heat capacitance and thermal conductance of each individual layer are added up. For multilayer structure, the effective conductivity at the sensing area is given by

$$k_{eff}A_T = (k_{VOx}A_{VOx} + k_{Si3N4}A_{Si3N4}) \tag{3.66}$$

where k_{VOx} and k_{Si3N4} is the conductivity of vanadium oxide and silicon nitride

Finally, stored thermal energy within each element is calculated as

$$Q_{st} = \rho_i c_i \Delta V \frac{dT}{dt}$$

$$Q_{st} = \rho_i c_i \Delta V \frac{\left(T_{m,n}(t+1) - T_{m,n}(t)\right)}{\Delta t} \tag{3.67}$$

where ρ_i and c_i are the density and specific heat of the multilayer structure and Δt is the time increment. The effective thermal capacitance of each section is also computed as

$$C_{total} = \sum_{i=1}^{n} c_i \rho_i \, v_i \tag{3.68}$$

where *n* denotes the number of layers

c_i is the specific heat capacity of each layer

ρ_i is the density of the each materials

v_i volume of the differential element

Effect of radiation can be negligible at low temperatures. However, for the high temperatures operation, which is expected in vacuum environments its effect needs to be included. The energy radiated to the surroundings can be expressed as

$$Q_{rad} = \varepsilon \sigma A_s \left(T_{sur}^4 - T_{m,n}^4(t)\right) \tag{3.69}$$

where A_s is the area of the exposed surface of the element and T_{sur} is the surrounding ambient temperature. Replacing the heat generation terms for joule heating and IR energy source Eq. (3.60) can be written as

$$\begin{aligned}\rho c_{eff}\Delta x\Delta y\Delta z\left(\frac{T_{m,n}^{i+1}-T_{m,n}^{i}}{\Delta t}\right)&\\ =\left(J_1^2\varphi_{VOx}(T)A_{vox}\Delta x+J_2^2\varphi_{Si3N4}(T)A_{Si3N4}\Delta x\right)&\\ +\left(P_{abs}e^{jwt}\right)x\Delta y\Delta z\ +\ k_{eff}^{left}\Delta y\Delta z\left(\frac{T_{m-1,n}^{i}-T_{m,n}^{i}}{\Delta x}\right)&\\ +k_{eff}^{right}\Delta y\Delta z\left(\frac{T_{m+1,n}^{i}-T_{m,n}^{i}}{\Delta x}\right)+k_{eff}^{up}\Delta x\Delta z\left(\frac{T_{m,n+1}^{i}-T_{m,n}^{i}}{\Delta y}\right)&\\ +k_{eff}^{down}\Delta x\Delta z\left(\frac{T_{m,n-1}^{i}-T_{m,n}^{i}}{\Delta y}\right)+Sk_{bottom}\left(T_s-T_{m,n}^{i}\right)\Delta x\Delta y&\\ +h_{m,n}\left(T_s-T_{m,n}^{t}\right)\Delta x\Delta y+\varepsilon\sigma\Delta x\Delta y\left[T_{m,n}^{4}-T_s^{4}\right]&\end{aligned} \tag{3.70}$$

In Eq. (3.70), the superscripts of *T* denote the time increment and the nodal coordinate system. The solution function *T* (x_m, y_n, t_i) of this differential equation describes the temperature of a thin films layer area of the different geometry, at every node position (x, y), at discrete time points t_0 = 0, t_1. . . t_n. By using Eq. (3.60), an explicit expression for the temperature at subsequent time i+1($T_{m,n}$ (i +1)) in terms of temperatures at the current time can be formed. The resulting expression can be written as

$$\begin{aligned}T_{m,n}^{i+1}=T_{m,n}^{i}+\left(J_1^2\varphi_{vox}(T)A_{vox}\Delta x+J_2^2\varphi_{Si3N4}(T)A_{Si3N4}\Delta x\right)+\left(P_{abs}e^{jwt}\right)x\Delta y\Delta z\ \frac{\Delta t}{\rho c}&\\ +\frac{k^{left}\left(T_{m-1,n}^{i}-T_{m,n}^{i}\right)\Delta t}{\rho c(\Delta x)^2}+\frac{k^{right}\left(T_{m+1,n}^{i}-T_{m,n}^{i}\right)\Delta t}{\rho c(\Delta x)^2}&\\ +\frac{k^{Up}\left(T_{m,n+1}^{i}-T_{m,n}^{i}\right)\Delta t}{\rho c(\Delta y)^2}+\frac{k^{down}\left(T_{m,n-1}^{i}-T_{m,n}^{i}\right)\Delta t}{\rho c(\Delta y)^2}&\\ +\frac{h_{m,n}\left(T_s-T_{m,n}^{i}\right)\Delta t}{\rho c\Delta z}+\varepsilon\sigma\Delta x\Delta y\left[T_{m,n}^{4}-T_s^{4}\right]&\end{aligned} \tag{3.71}$$

At time t = 0, the temperature of every nodes (x, y) is given by T_s(x, y), which is the substrate temperature. When the scheme is written in this form, we observe that the values on the time level t_{i+1} are computed using only the values on the previous time level t_m. Therefore we refer to this scheme as explicit. This is in contrast to implicit schemes where we have to solve a tridiagonal system of linear equations in order to pass from one time level to the next.

With initial and boundary conditions set as

$T(x, y, 0) = T_s(x, y)$ the initial temperature at t=0 all nodes will have the same temperature as environment (substrate)
$T(0, y, t) = T_s(y)$ temperature at the left anchor is same as the substrate
$T(x, L_1, t) = T_s(y)$ temperature at the right anchor is same as the substrate

We want to approximate the solution function T(x, y, t) at discrete points (x, y, t). Thus, we will define spatial mesh points

$$\begin{aligned} &(x_i, y_j) = (i.\Delta x, j.\Delta y) \\ &i = 0,1,2 \ldots., M+1 \text{ and } j = 0,1,2 \ldots., N+1 \\ &\Delta x = \tfrac{1}{M+1}, \text{ and } \Delta y = \tfrac{1}{N+1} \text{ temporal mesh sizes} \\ &t_k = k.\Delta t, k = 0,1,2 \ldots., \end{aligned} \tag{3. 72}$$

With respect to computational effort and exactness of the approximation, N, M and Δt may be chosen arbitrarily. In particular, one has to secure that the numerical method will be stable. This means, small perturbations e.g. resulting from rounding errors do not cause the resulting numerical solutions to diverge from each other without bound. For the heat equation, we know from theory that we have to obey the restriction [35]

$$\Delta t \leq \frac{(\Delta x)^2}{2c} \tag{3.73}$$

Or

$$\Delta t \leq \frac{(\Delta y)^2}{2c}$$

where c is thermal diffusivity

The validity of Eq. (3.73) is mainly to make the finite difference method solution to be stable. For an iterative solution, if m denotes the iteration number, one can use the following approximation [25]

$$T_{m,n}^{t+1^4} \approx 4T_{m,n}^{t^3}T_{m,n}^{t+1} - 3T_{m,n}^{t^4} \tag{3.74}$$

$$\begin{aligned} T(m,n,i+\Delta t) &= T_{m,n}^{i} + Q_{m,n}^{IR}\frac{\Delta t}{\rho c} + \frac{k^{left}\left(T_{m-1,n}^{i} - T_{m,n}^{i}\right)\Delta t}{\rho c(\Delta x)^2} \\ &+ \frac{k^{right}\left(T_{m+1,n}^{i} - T_{m,n}^{i}\right)\Delta t}{\rho c(\Delta x)^2} + \frac{k^{Up}\left(T_{m,n+1}^{i} - T_{m,n}^{i}\right)\Delta t}{\rho c(\Delta y)^2} \\ &+ \frac{k^{down}\left(T_{m,n-1}^{i} - T_{m,n}^{i}\right)\Delta t}{\rho c(\Delta y)^2} + \frac{h_{m,n}\left(T_s - T_{m,n}^{i}\right)\Delta t}{\rho c \Delta z} \\ &+ \varepsilon\sigma\Delta x\Delta y\left(4T_{m,n}^{t^3} - 3T_{m,n}^{t^4}\right) \end{aligned} \tag{3.75}$$

Therefore, by solving the system of difference equations from all of the elements over a series of time increments, a profile of temperatures throughout the device as a function of time can be produced. In numerical analysis, much effort is spent on the search for efficient schemes in the sense of optimizing accuracy and minimizing CPU time and memory requirements. Often, the most powerful techniques for solving partial differential equations use as much analytical information as possible. The so-called spectral methods are illustrative examples of this phenomenon. These methods are carefully constructed in order to take advantage of all the analytical insight we have gained through the development of Fourier techniques. Although in many respects it is quite similar to the finite difference method, the finite element method is preferable when it comes to complicated geometries in several space dimensions [34].

3.5 Thermo-Mechanical Analytical Model

Joule heating induces thermal stress and strain due to mismatch of the thermal coefficient of expansion (CTE) between different materials. The resulting structure deformations cause both tensile and compressive stresses in microbolometer legs and plate. For the Thin Single Stage microbolometer, the deformations of the microbolometer structure are mainly caused by the elongation of vanadium and vanadium oxide due to their higher CTE values. As a result, the sensing semiconductor plate along with the leg will bent up. The deformation is similar for the test PolyMUMPs® test device due to the gold higher thermal expansion value than polysilicon.

In the case of thermo-mechanical coupling, a good approximation is the solution of the thermal problem on a Lagrangian grid. The Lagrangian grid compute the time evolution of the different region material elements as grid cell elements and all dependent variables, including temperature, are evolved using a Lagrangian approach. This approach uses a finite element method to characterize the deflection of the actual device as a function of temperature at each time steps. In this section however, we implemented analytical approach with certain assumption to develop the deflection of the leg structure. This analytical approach can also be used to break the flexure leg into separate beam segments. In this case, the temperature increase due to joule heating is obtained from the electro-thermal analytical model and will be used to calculate the average temperature increase in the legs. The temperature distribution and the multilayered beam equations are used to calculate the effective force exerted by the tip of the multilayered cantilever as it curls upward or downward due to the thermal expansion mismatch between the multilayer structures. In deriving the analytical model for the PolyMUMPs® test device, the following assumptions are made:

- The temperature distribution assumed to increase uniformly across the leg with an average value
- There is no internal friction between the multiple layers
- The neutral axis of the multilayered beam lies on the same line as the neutral axis of the additional beam segment,

- The temperature and material properties assumed to be constant throughout the beam and with respect to time.

3.5.1 Stress and Deflection Analysis

Analytical model for the PolyMUMPs® test devices has been developed to compute the deflection due to thermal gradient. The PolyMUMPs® test device legs are bi-material beam and deflect as the beam temperature changes due to the mismatch of the thermal expansion of the two different materials.

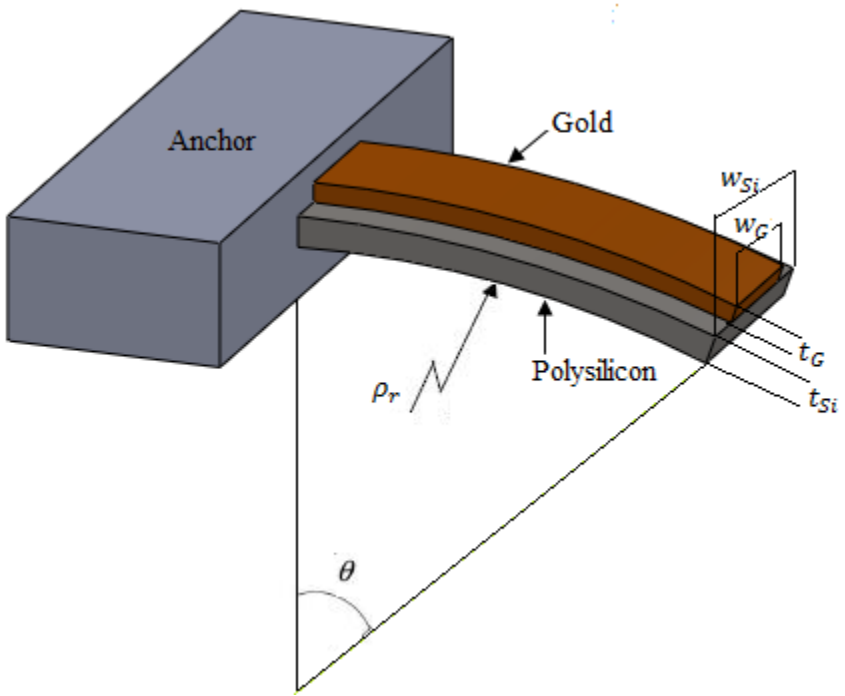

Figure 3.16: Schematic diagram of the test device bi-layer strip deflection due to thermal effect

To calculate the deflection of the beam, first we can decompose the bi-material beam into two free standing beams. Apply an effective force F_i and moment M_i on each beam to ensure the continuity of the strain and stress at the interface. For the stress and moment balance on the beam, we should have:

$$F_G = F_{Si} = F \text{ and } M_G + M_{Si} = Ft/2 \tag{3.76}$$

where F_G & F_{Si} are the forces in the gold and polysilicon layer respectively

M_G & M_{Si} are the moments in the gold and polysilicon layer respectively

$t = t_G + t_{Si}$ is the total thickness of the bi-material beam and the strain induced by thermal expansion in the beam is:

$$\varepsilon_{t,i} = \alpha_i(T - T_s) \tag{3.77}$$

where α_i is the coefficient of thermal expansion (CTE), with i=1, 2 specify beam 1 (gold) and beam 2 (Polysilicon), T the beam temperature, and T_s is the initial temperature of the beams, which is the substrate temperature .

The strain induced by the effective force *F* is:

$$\varepsilon_{f,i} = \frac{F}{E_i w_i t_i} \tag{3.78}$$

where E_i is Young's modulus of the materials, and

w_i *is* the width of the each beam (gold and polysilicon)

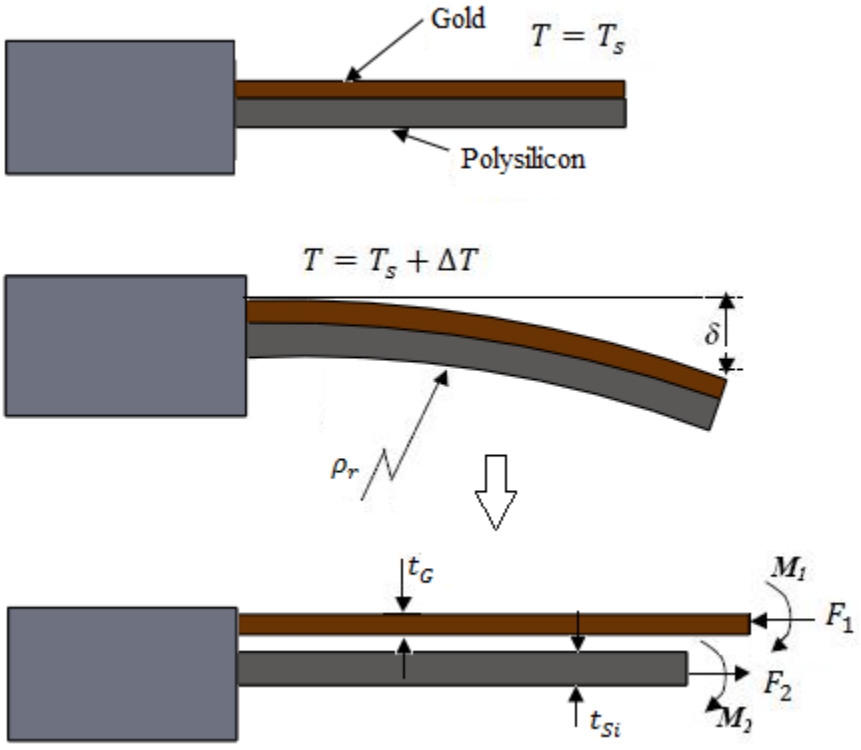

Figure 3.17 Schematic diagram of bi-layer cantilever beam for thermo-mechanical analysis

The effective moment will induce the bending of the beam. Assume the beam is bent into a curve with radius ρ. From the geometry relation, the strain at the surface of the beam induced by this moment can be written as:

$$\varepsilon_{M,i} = \pm\frac{t_i}{2\rho_i} \tag{3.79}$$

and

$$M_i = \frac{E_i I_i}{\rho_i} = \frac{E_i w_i t_i^3}{12\rho_i} \tag{3.80}$$

with ($\pm$) sign for top and bottom surface of the beam, and *I* the inertial momentum of the beam. Considering small deformation of thin beam, that the radius ρ is much larger than the thickness of the beam, we can assume that $\rho_G = \rho_{Si} = \rho$.

Combine Eq. (3.77) – (3.79) to get total strain at interface for each beam:

$$\varepsilon_G = \alpha_G(T - T_s) - \frac{F}{E_G w_G t_G} - \frac{t_G}{2\rho}, \text{ and } \varepsilon_{Si} = \alpha_{Si}(T - T_s) + \frac{F}{E_{Si} w_{Si} t_{Si}} + \frac{t_{Si}}{2\rho}, \tag{3.81}$$

Because of the continuity at interface, we should have $\varepsilon_G = \varepsilon_{Si}$, thus

$$\alpha_{Vox}(T - T_o) - \frac{F}{E_G w_G t_G} - \frac{t_G}{2\rho} = \alpha_{Si}(T - T_o) + \frac{F}{E_{Si} w_{Si} t_{Si}} + \frac{t_{Si}}{2\rho} \tag{3.82}$$

Substitute Eq. (5-76) and (5-80) into the above equation the curvature of the beam $\kappa = 1/\rho$ can be written as:

$$\alpha_G(T - T_o) - \frac{E_G w_G {t_G}^3 + E_{Si} w_{Si} {t_{Si}}^3}{6t\rho(E_G w_G t_G)} - \frac{t_G}{2\rho} = \alpha_{Si}(T - T_o) + \frac{E_G w_G {t_G}^3 + E_{Si} w_{Si} {t_{Si}}^3}{6t\rho(E_{Si} w_{Si} t_{Si})} + \frac{t_{Si}}{2\rho} \tag{3.83}$$

$$(\alpha_G - \alpha_{Si})(T - T_o) = \frac{1}{\rho}\left(\left(\frac{E_G w_G {t_G}^3 + E_{Si} w_{Si} {t_{Si}}^3}{6t(E_{Si} w_{Si} t_{Si})} + \frac{t_{Si}}{2}\right) + \left(\frac{E_G w_G {t_G}^3 + E_{Si} w_{Si} {t_{Si}}^3}{6t(E_G w_G t_G)} + \frac{t_G}{2}\right)\right) \tag{3.84}$$

$$\kappa = \frac{1}{\rho} = \frac{(\alpha_G - \alpha_{Si})(T - T_s)}{\left(\left(\frac{E_G w_G {t_G}^3 + E_{Si} w_{Si} {t_{Si}}^3}{6t(E_{Si} w_{Si} t_{Si})} + \frac{t_{Si}}{2}\right) + \left(\frac{E_G w_G {t_G}^3 + E_{Si} w_{Si} {t_{Si}}^3}{6t(E_G w_G t_G)} + \frac{t_G}{2}\right)\right)} \tag{3.85}$$

The deflection of a free standing cantilever under the moment M along the beam is:

$$\frac{d^2z}{dx^2} = \frac{M}{E_i I_i} = \frac{1}{\rho}$$
$$\left.\frac{dz}{dx}\right|_{x=0} = 0 \qquad (3.86)$$
$$z|_{x=0} = 0$$

Solving the Eq. 3.86 with the boundary condition the deflection along the length of the beam can be found us

$$z(x) = \frac{(\alpha_G - \alpha_{Si})(T - T_s)}{2\left(\left(\frac{E_G w_G {t_G}^3 + E_{Si} w_{Si} {t_{Si}}^3}{6t(E_{Si} w_{Si} t_{Si})} + \frac{t_{Si}}{2}\right) + \left(\frac{E_G w_G {t_G}^3 + E_{Si} w_{Si} {t_{Si}}^3}{6t(E_G w_G t_G)} + \frac{t_G}{2}\right)\right)} x^2 \qquad (3.87)$$

The above model is used to compute the deflection for test structure fabricated in PolyMUMPs®. The average leg temperature is used to compute the deflection for multilayer structure. However in actual case a thermal gradient exist in the leg and the deflection. The temperature distribution in the leg section depends in environment of operation. In order to use the above deflection of the microbolometer leg average temperature (T_{leg_avg}) has to be computed from electro-thermal model developed in the previous sections. Therefore, we calculate the tip deflection of the leg at the contact point with the microplate for the average temperature change by:

$$\delta_{tip} = \frac{(\alpha_G - \alpha_{Si})(T_{leg-avg} - T_s)}{2\left(\left(\frac{E_G w_G {t_G}^3 + E_{Si} w_{Si} {t_{Si}}^3}{6t(E_{Si} w_{Si} t_{Si})} + \frac{t_{Si}}{2}\right) + \left(\frac{E_G w_G {t_G}^3 + E_{Si} w_{Si} {t_{Si}}^3}{6t(E_G w_G t_G)} + \frac{t_G}{2}\right)\right)} L^2 \qquad (3.88)$$

where L is the length of the test device

In this research the temperature of the pixel structure is not directly measured during the experiment due to the size of the pixel. Therefore, in order to relate the deflection to the temperature Eq. (3.89) can be used. This can relate the temperature with the deflection i.e if we

can measure the deflection of the test device from the experiment we can indirectly compute the average temperature of the pixel from

$$\left(T_{leg-avg} - T_s\right) = \frac{2\left(\left(\frac{E_G w_G {t_G}^3 + E_{Si} w_{Si} {t_{Si}}^3}{6t(E_{Si} w_{Si} t_{Si})} + \frac{t_{Si}}{2}\right) + \left(\frac{E_G w_G {t_G}^3 + E_{Si} w_{Si} {t_{Si}}^3}{6t(E_G w_G t_G)} + \frac{t_G}{2}\right)\right)\delta_{tip}}{(\alpha_G - \alpha_{Si})L^2} \tag{3.89}$$

$$T_{leg-avg} = \frac{2\left(\left(\frac{E_G w_G {t_G}^3 + E_{Si} w_{Si} {t_{Si}}^3}{6t(E_{Si} w_{Si} t_{Si})} + \frac{t_{Si}}{2}\right) + \left(\frac{E_G w_G {t_G}^3 + E_{Si} w_{Si} {t_{Si}}^3}{6t(E_G w_G t_G)} + \frac{t_G}{2}\right)\right)\boldsymbol{\delta_{tip}}}{(\alpha_G - \alpha_{Si})L^2} + T_s \tag{3.90}$$

3.6 Finite Element Modeling Using ANSYS®

Finite element methods (FEM) are strong numerical solution techniques with proven advantages and have become an essential part of design processes in many engineering areas. Designing a microbolometer with specific characteristics requires multiphysics analysis to solve the coupled-field electro-thermal and thermo-mechanical problem. This section provides the FEA analysis for Thin Single Stage and test device as specified. ANSYS® multiphysics software has been used to analyze the microbolometer subjected to DC bias joule heating.

The FEM was simulated in different condition as per the need of each section below. To compare the FEM simulations to the analytical and numerical model, the simulation has been done under the same condition. Only a DC bias current load generates the heat without radiation heat transfer mechanism. Although the numerical model can include infrared radiation heat source and radiation heat transfer mechanisms the analytical model simplified without these components. The analysis assumes vacuum conditions with the heat being dissipated through the legs. Hence, the heat energy is assumed to be dissipated to the heat sink (i.e., the substrate) through conduction. This thermal loading induces deflection, stress and temperature distribution. Using ANSYS®, the coupled electrical-thermal-structural governing equations are solved to obtain the temperature distribution, deformations, and stresses. For the FEM simulations, we have used the geometry, dimensions and material properties specified in the previous section for Thin Single Stage microbolometer and PolyMUMPs® test device.

The electro-thermal analytical method introduced in the previous chapter section uses a one-dimensional model (1D) for the Thin Single Stage microbolometer and assumes the legs are straight. This assumption does not incorporate a large error in the 1D model since for the most part, the cross section and material properties can be considered uniform across the legs. However, due to flexural deformations of the device, this assumption cannot be used in a thermal-structural model and thus, a full three-dimensional (3D) model is required. All governing equations used in ANSYS® multiphysics have been solved in the 3D domain. To extract an accurate and reliable result from the simulations, it is important to recreate detailed features of the structure in the model. To do so, the 3D models for the FEM analysis of the microbolometer were created in SolidWorks® software and then imported to ANSYS®.

The direct coupling method is the most efficient method to solve the problem using ANSYS® software. The direct method usually involves just one analysis that uses a coupled-field element type containing all necessary degrees of freedom. ANSYS® offers a variety of coupled elements to handle different types of multi-physics problems. For electro-thermal and structural couple problem Solid98 elements is the most appropriate element with all the necessary degrees of freedom. These degrees of freedoms include displacement in all direction (U_X, U_Y, and U_Z), temperature (TEMP), and voltage (VOLT) to solve coupled structural-thermal-electric analyses.

Figure 3.18 shows the schematic of the mesh used for the Thin Single Stage microbolometer. As shown in this figure, to increase the time efficiency of the analysis, different mesh densities were adopted for the legs and plates. In addition, the meshed model was merged between the different materials used in the analysis to reduce the number of integration points.

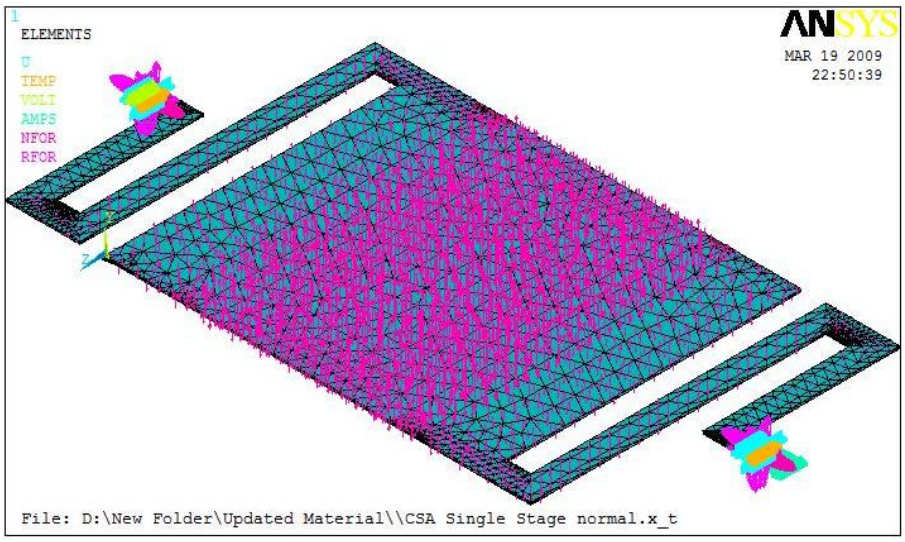

Figure 3.18- Meshed model with applied boundary conditions and load for a Thin Single Stage

Boundary conditions of three different domains (i.e. electrical, thermal and mechanical domains) are applied to the model. For the electrical boundary condition, different constant bias currents were applied across the legs and plate. In addition, a voltage equal to zero Volts was assigned to the end of one of the legs. The thermal boundary conditions assume that the temperature at the end of both legs is at the substrate temperature. In addition the substrate is considered as a perfect heat sink and its temperature is fixed and equal to T_{sub} = 223K (-50^{o}C). For the mechanical boundary conditions, we have considered that the ends of the legs are fixed to the substrate through the anchors, i.e. at the anchor supports $U_X = U_Y = U_Z = 0$.

The temperature distribution across the microbolometer is simulated due to the joule heating the effects only. We also simulated vacuum conditions and the heat dissipation through radiation has been included. Hence, the only heat transfer mechanism considered for the simulations is the heat conduction to the substrate through the legs.

Chapter Four

Microbolometer Performance Analysis and IR Absorption Modeling

To fully understand the process of infrared (IR) detection, some basic properties of the signals must first be understood. At room temperature, an object emits most of its energy in the form of IR radiation. Therefore, in observing terrestrial objects and activities without light reflection, infrared radiation is one of the most important spectrums to be monitored. To understand radiation characteristics of the target object in general, a blackbody concept is very useful. A blackbody, on an ideal surface, has three important properties [24]:

(i) All incident radiation is absorbed by a blackbody, regardless of wavelength and direction.
(ii) No surface can emit more energy than a blackbody for a defined temperature and wavelength.
(iii) A blackbody emits radiation as a function of wavelength and temperature, but this radiation is independent of direction. Therefore, a blackbody is a dispersed emitter.

There are two types of IR detectors, namely the photon and thermal detectors which were introduced in Chapter two. Thermal detectors are broadband sensors and have a very wide spectral response, up to ~100 μm wavelength. Therefore, materials with high emissivity are more suitable IR detector materials. However, due to the detection mechanism they have a slower response time compared to photo detectors. For the temperature of the blackbody and the wavelength range filtered from λ_1 to λ_2, the incident power on the bolometer can be calculated by [21]

$$P_{Signal} = \frac{\Omega_s \gamma M}{\pi} \tag{4.1}$$

where Ω_s is the solid angle for a round aperture as shown in Figure 4.1

γ is the transmittance, and

M is the exitance, defined in Eq. 4.3.

The solid angle is characterized by the microbolometer design and for a round aperture it can be express as

$$\Omega_s = \pi \frac{r^2}{R^2 + r^2} \tag{4.2}$$

where *r* is the radius of the aperture,

R is the distance between the blackbody and the bolometer as given in the Figure 4.1

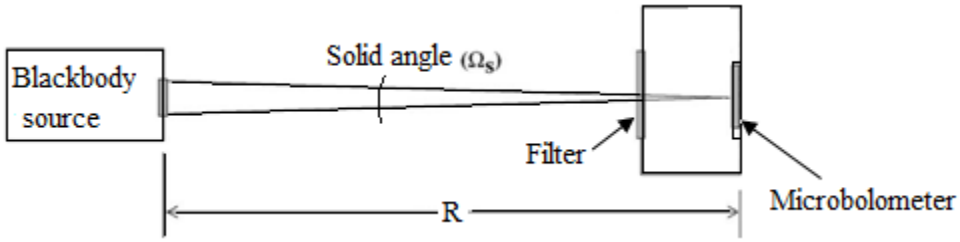

Figure 4.1: Microbolometer setup for IR absorption

The exitance, defined in Eq. (4.1), is the power per unit area leaving a blackbody surface. Mathematically, spectral exitance is defined by

$$M = \int_{\lambda_1}^{\lambda_2} \frac{2\pi hC^2}{\lambda^5 [e^{hC/\lambda kT} - 1]} d\lambda \tag{4.3}$$

where *h* is the Planck constant

k is the Boltzmann constant

C is the speed of light in vacuum

Replacing Eq. (4.3) and Eq. (4.2) into Eq. (4.1) provide a very important equation to quantify the radiation power, which is also called Planck law [21].

$$P_{Signal} = \frac{\gamma}{\pi}\pi\frac{r^2}{R^2 + r^2}\int_{\lambda_1}^{\lambda_2}\frac{2\pi hc^2}{\lambda^5[e^{hc/\lambda kT} - 1]}d\lambda \tag{4.4}$$

Integrating the Planck distribution in Eq. (4.4) over wavelengths length of interest for a given temperature yields the blackbody emissive power, P_{in}. Introducing emittance into the integrated Eq. (4.4) yields Eq. (4.5). This is a modified Stephan-Boltzmann law with emittance, e and microbolometer setup parameter, solid angle.

$$P_{Signal} = e\frac{\gamma}{\pi}\left(\pi\frac{r^2}{R^2 + r^2}\right)\sigma T^4 \tag{4.5}$$

where T is the temperature of the blackbody

e is emittance

σ is the Stefan-Boltzmann constant.

As indicated in Eq. (4.5), the amount of infrared emitted by a blackbody is a strong function of its temperature. Therefore, the total emitted radiation energy can be calculated given the absolute temperature, T. This relationship is at the core of IR thermography because it is the emissive power that an IR imager physically measures, while temperature is the parameter of interest. In order to determine the temperature of blackbody we need to know how the peck wavelength related to the temperature. The Wien displacement law expresses this relationship of temperature, T to the peak wavelength, λ_{peak}, of radiation emitted by a body [24]:

$$\lambda_{peak}.T = 2897.8\ \mu m.\,K \tag{4.6}$$

Equation (4.6) can be used to compute the temperature of a surface if for a peak wavelength of interest. For example, most viewed images in our surroundings are near 300 K, and the corresponding wavelength distribution for this temperature is around 10 μm with approximation of black body. Most of thermal imaging systems operate in Medium Wavelength Infrared (MWIR) or Long Wavelength Infrared (LWIR) ranges. Thin Single Stage has been design to measure signal

in the range of 8 to 12 µm with a peak wave length of 10 µm [1]. Therefore Eq. (4.5) and (4.6) can be used to estimate the amount of IR energy absorbed in the microbolometer.

4.1 Types of Infrared

The infrared (IR) is a certain range of wavelength longer than visible light. This IR radiation was discovered only 200 years ago by William Herschel's prism splitting of sunlight [25]. Using his own invented monochromator, he measured the radiation energy and classified it according to the color range. However, the radiation energy was still detectable within invisible range over red color area called infrared. What is considered to be infrared light spans 3 orders of magnitude and is usually divided into several regions that have different practical significance. The near infrared spans from 0.75 μm to 1.5 μm and it is used in telecommunications applications. Another application for near-infrared is remote sensing, e.g., to study and detect vegetation by their optical signature. Short and medium wavelength infrared ranging from 1.5 μm to 7 μm and can be used to detect some gases. Long wavelength infrared (8 μm − 14 μm) finds its main use in thermal imaging [36].

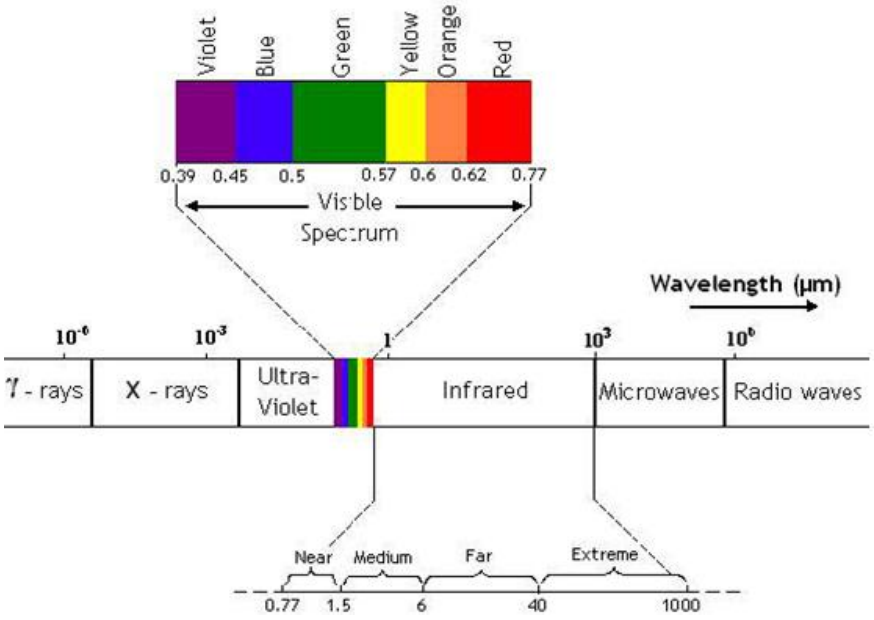

Figure 4.2: The infrared portion of the electromagnetic spectrum

There are many different applications for using the detective ability of non-visible wavelength generated from radiation energy: exploring space objects, military, security guard, medical investigation, night-vision systems for automobiles, fire detection, industrial and constructional areas in any kinds of weather condition.

4.2 Atmospheric Transmission

Due to absorption from water and carbon dioxide, the atmosphere is not transparent to all infrared wavelengths. In nature, there exist convenient windows of atmospheric transmission of infrared (IR) light. Infrared detectors are used to detect radiation emitted by a target. Figure 4.3 shows the transmission spectrum of the earth's atmosphere through a 1km path. As can be seen in the figure, there are two bands of wave-length to which the atmosphere is transparent: the 3μm−5 μm and the 8 μm −14 μm.

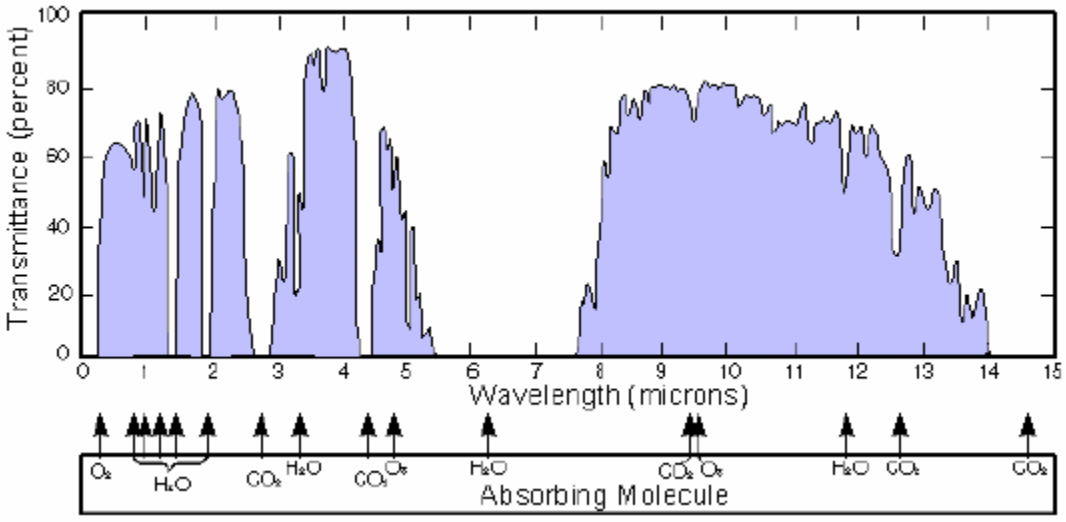

Figure 4.3: Atmosphere Transmission Spectrum

Generally, to remotely measure the temperature of an object, one must be able to determine the amount of infrared radiation it emits, preferably in the $8\mu m - 14\ \mu m$ atmospheric window. It is also possible to use the $3\ \mu m - 5\ \mu m$ window, but less infrared is emitted in this range, making it more demanding on the infrared detector that is used. Thermal imaging, which refers to the ability to measure the temperature on different points on a scene, requires either an array of

infrared detectors operating in those wavelength ranges or a way to scan a scene using a single detector. There are many applications to thermal imaging including both for civilian or military applications.

4.3 Microbolometer Performance Analysis

The performance of microbolometer is mainly determined by their thermal properties such as the temperature coefficient of resistance (TCR) of the IR absorber, the thermal isolation of the microplate (characterized by the microbolometer thermal conductance), and the absorption coefficient, η (the fraction of the incident power converted to signal). A suspended microplate provides a good thermal isolation, while the thermal efficiency is enhanced using optical interference as well as coating the surface of the microplate with a high-IR absorption layer. Therefore, optimization of the thermal parameters is a vital step in the design process to obtain higher sensitivities.

The determination of the absorption coefficient (η) of microbolometer sensors is not a straightforward task due to the complex geometry of the microbolometer structure and the uncertainty of the material parameters. This chapter mainly focus to develop analytical model to compute the absorption coefficient for Thin Single Stage microbolometer. The analytical model developed in this section will be used to calculate the IR energy absorbed for the electro-thermal analysis for the numerical model. To augment this discussion, first some of the material parameters that affect the device performance are briefly discussed.

One of the primary information that need to be determine for microbolometer performance is the average temperature change of the pixel area at different condition. The change in temperature can happen due to the heat energy generation from joule heating or the absorptions of IR energy. The average temperature change primarily used to obtain the change in resistance of the sensor layer and conductance of the structure. Therefore, the increment in average temperature, $\overline{\Delta T}_{avg}$ (see Figure 4.4), for Thin Single Stage microplate has to be calculated. At steady state, the average microplate (region III) temperature is given by [1]:

$$\bar{T}_{avg} = \left(\int_{l_l}^{l_l+l_p} T_p(x)dx \right) / l_p \tag{4.7}$$

where l_l is the length of the TSS microbolometer leg

l_p is the length of the microplate

$T_p(x)$ is the temperature distribution for region III as computed in the previous chapter

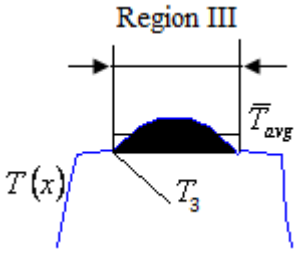

Figure 4.4: The temperature-Position plot for Thin Single Stage region III

As defined in chapter three Thin Single Stage is subdivided in to Five regions. Each Region has different temperature distribution as a function of position based on the constant value C_i computed from the region geometry and material properties. A detail result analysis of the electro-thermal models will be presented in the next chapter. In Figure 4.4, we presented example temperature distribution for thin Single stage in order to explain how the average temperature computed. Equation (4.7) is basically calculates the area under the temperature curve in region III and divide this value to obtain average microplate (region III) temperature values. Using the solution obtained in chapter three for the microbolometer region III temperature distibution, $T_p(x)$ and integrating Eq. (4.7) over the length of these regions, the average temperature will be

$$\bar{T}_{p_{(avg)}} = T_3 + \left(\frac{C_3}{\beta * l_p} * e^{(\beta(l_l+l_b))} - e^{(\beta * l_l)} \right) - \left(\frac{C_4}{\beta * l_p} * e^{(\beta(l_l+l_b))} - e^{-(\beta * l_l)} \right) \tag{4.8}$$

where T_3 is the contact temperature between region II and region III

C_3 and C_4 are the constant computed in Eq. 3.51 and β is defined in Eq. 3.41

The average temperature of the nodes from the numerical methods solution can be computed by taking the overall sum of each node temperature and dividing this to the number of nodes. This temperature on the microplate can expressed as

$$\bar{T}_{p_{(avg)}} = \left(\int_0^M \int_0^N T_p(x, y, t) \right) / \left(M_p * N_p \right) \tag{4.9}$$

where $T_p(x, y, z, t_c)$ is the temperature of each nodes in the microplate region

M_p and N_p are number of microplate nodes in the x and y direction respectively

For the test device the microplate is only have one region with average temperature is given by $\bar{T}_{p_{(avg)}}$ as given above. However, for Thin Single Stage the microplate has three different regions. Therefore, the weighted average for each region is computed from $\bar{T}_{p_{(avg)}}$ and indicated as in the subsequent section as $\bar{T}_{avg}$.

Microbolometer measure the change in temperature of the microplate due to the IR absorbed temperature. It's also important to compute the change in temperature due to joule heat for the device reliability and performance analysis. The average change in temperature on the bridge due to joule heating can be obtained as

$$\Delta\left(T_p\right)_{JH} = \bar{T}_{avg} - T_s \tag{4.10}$$

where T_s is the substrate temperature assume to be the initial boundary condition

The temperature change when an incident infrared energy absorbed with the microplate can be calculated from the ration of the absorbed energy and the total thermal conductance of the pixel design

$$\Delta\left(T_p\right)_{IR} = \frac{P_{abs}}{G_{total}} = \frac{\eta P_{signal}}{G_{total}} \tag{4.11}$$

where G_{total} is the total thermal conductance of the microbolometer given by Eq. (4.16)

η is the absorption coefficient or coupling efficiency,

To develop highly sensitive thermal detectors, the corresponding temperature change must be as large as possible [31]. Therefore, if the sensing plate (*Vanadium oxide*) has a resistance R_0 at room temperature and a temperature coefficient of resistance (TCR) equal to α, the average resistance is given by,

$$R_{average} = R_o\left(1 + \alpha\Delta\left(T_p\right)_{IR}\right) \tag{4.12}$$

and the change in resistance due to the absorbed IR energy is then

$$\Delta R(T) = R_o\alpha\frac{\eta P_{signal}}{G_{Total}} \tag{4.13}$$

The change in voltage ΔV, is measured when the microbolometer is biased with a current I_{app}, and can be expressed as

$$\Delta V(IR) = I_{app}R_o\alpha\frac{\eta P_{signal}}{G_{Total}} \tag{4.14}$$

Another important microbolometer characteristic feature is the total capacitance of the microplate. The detecting area of the thermal detector can be expressed by a thermal capacitance C_{th}, called thermal mass, the absorbing volume to store heat energy. The thermal capacity of the bolometer pixel can be expressed by [17]

$$C = \sum_{i=1}^{n} v_i\rho_i c_i \tag{4.15}$$

where v_i is the volume of each bolometer membrane material, ρ_i is the density of each bolometer membrane material and c_i is the specific heat of each bolometer membrane material.

4.3.1 Thermal Conductance

The microplate area is thermoelectrically coupled to the supporting structure and thermal insulating material as a supporting membrane is required to minimize the heat flow. The thermal conductance (W/K) is defined as the heat energy per unit time that is required to increase the area-averaged temperature of the microbolometer IR sensitive plate by 1K. The thermal conductance (G) gives a measure of how well the plate is thermally isolated from the substrate. Better thermal isolation results in higher microbolometer sensitivity since the incoming IR radiation will be absorbed faster. Therefore, thermal insulating materials as a supporting membrane are required to minimize the heat flow. However, improving the thermal isolation reduces the sensing speed of the microbolometer. Therefore, careful consideration of the thermal conductance parameter is required at the design stage to optimize sensitivity without compromising speed [26]. The total thermal conductance between a bolometer and its surrounding can be estimated by [23]

$$G_{total} = G_{cond} + G_{rad} + G_{gas-cond} + G_{conv} \tag{4.16}$$

where G_{cond} is the thermal conductance between the bolometer and its surrounding through the bolometer legs, G_{rad} is the thermal conductance between the bolometer and its surrounding by emitted heat radiation, $G_{gas-cond}$ is the thermal conductance between the bolometer and its surrounding through the gas, and G_{conv} is the thermal conductance between the bolometer and its surrounding by gas convection.

If a bolometer array is operated in a vacuum atmosphere, both the thermal conduction ($G_{gas-cond}$) through the gas and the thermal conduction (G_{conv}) by gas convection are negligible [34]. In this situation, the thermal conduction between the bolometer and its surrounding is dominated by the thermal conduction G_{cond} through the bolometer legs. Therefore, ignoring the effect of radiation, the thermal conductance of the microbolometer operating in vacuum can be computed by

$$G_{cond} = 2 * \sum_{i=1}^{n} k_i . \frac{A_i}{L_i} \tag{4.17}$$

where k_i is the thermal conductivity of the material

A_i is the cross section area of the leg structure

L_i is the length of the arm

For Thin Single Stage microbolometer

$$G_{cond} = 2 * \left(k_{leg.Vox} . \frac{A_{leg-Vox}}{L_{leg}} + k_{leg.Si3N4} . \frac{A_{leg-Si3N4}}{L_{leg}} \right) \tag{4.18}$$

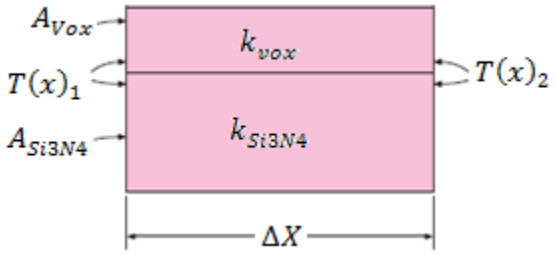

Figure 4.5: Microbolometer multilayered leg structure

If a bolometer array is operated in a gas atmosphere, the thermal conduction $G_{gas\text{-}cond}$ through the gas contributes significantly to the total thermal conductance G_{total} between the bolometer and its surrounding. For practical cases, the thermal conductance G_{conv} by gas convection is negligible compared to the thermal conductance $G_{gas\text{-}cond}$ through the gas [34]. With the assumptions that the temperature difference between the bolometer membrane and its surrounding is small, the thermal conductance G_{rad} emitted by infrared radiation can be expressed as [36]

$$G_{rad} = 8\epsilon\beta\sigma A_s \left(\bar{T}_{avg}\right)^4 \tag{4.19}$$

where σ is the Stefan-Boltzmann constant, ε is the effective emissivity of the bolometer membrane, β is the bolometer fill factor, A is the bolometer pixel area (pixel pitch), and $\bar{T}_{avg}$ is the average temperature of the bolometer membrane. In most practical cases the thermal

conduction due to radiation, G_{rad} is negligible compared to the thermal conduction $G_{leg\text{-}cond}$ through the bolometer legs [29].

At steady state, the general heat equation mathematically was express in chapter 3 as in Eq. 3.18. Neglecting the radiation, the thermal conductance of the microbolometer also be given by:

$$G_{th} = \frac{q_t(x, y, z, t)}{\bar{T}_{avg} - T_s} \tag{4.20}$$

where $q_t(x, y, z, t)$ is the total heat energy generated or absorbed as given in Eq. 3.5, and the denominator is the area-averaged plate temperature increase. When the microbolometer is electrically biased, the total generated heat is due to the effect of the incident infrared power as well as the electrical joule heating.

4.3.2 Time Constant

The thermal time constant, τ, is another important design parameter as it indicates the time response of the microbolometer. In general, thermal time constant of thermal detectors is longer than the photon detectors. For example, for an imaging system with real time detection, the value of τ must be lower than the inverse of the frame rate [26]. The frame video rate of the imaging system is limited by τ. For instance, a video frame rate of 30 Hz requires the time constant to be less than 15 ms [17]. Thermal time constant can be defined by the ratio of thermal mass over thermal conductance,

$$\tau = \frac{C_{total}}{G_{total}} \tag{4.21}$$

where τ *is the time constant*

C_{total} and G_{total} are strongly related to the sensing material properties and geometries of the bolometer. According to this expression, in order to reduce τ, C_{total} should be decreased and G_{total} should be increased. Reducing C_{total} may be a good idea; however increasing G_{total}

would end up in a lower responsivity. Therefore, to increase τ a reduction in G_{total} should be made in conjunction with a reduction in C_{total}, so as to keep τ in a predefined range. The thermal time constant (τ) can also be expressed as the time for the excess temperature (T) to reach ~63% of its steady-state value, following a step change in input power. Therefore, it defines the response speed of the microplate temperature to a change in input power.

4.3.3 Responsivity ($\Re$)

The sensitivity of a microbolometer is mainly characterized by its responsivity, $\Re$. The responsivity is a basic figure of merit in both IR detectors and detector focal plane arrays (FPAs) and it is defined as the output signal voltage or output signal current of an infrared bolometer pixel per incident radiant power on the pixel. The relationship between the absorbed IR energy (P_{abs}) and the incoming IR energy on the microplate (P_{In}) is given by

$$P_{abs} = \eta . P_{Signal} \tag{4.22}$$

For uncooled microbolometers, the responsivity, $\Re$ can be expressed as [25]:

$$\Re = \frac{\Delta V}{P_{abs}} = \frac{I_{app}\alpha\beta R_{eff}\eta}{G_{total}\sqrt{1+\omega^2\tau^2}} \tag{4.23}$$

where I_{app} is the applied current, R_{eff} is the resulting resistance of the parallel bolometer resistance and the ROIC Input impedance, η is the absorption coefficient, β is the fill factor, G_{total} represents the thermal conductance of the multilayer structure, ω is the modulation angular frequency, and τ is the thermal time constant. The responsivity is high when:

- The absorptivity is high and therefore, most of the incoming radiant flux is absorbed and converted to temperature rise.
- The thermal conductance is small providing good absorber insulation and a high temperature rise for a given absorbed radiant flux.

- The TCR of the thermistor (α) is large leading to a large change in resistance for a given change in absorber temperature.
- I_{app} is high and hence a big change in signal voltage for a given change in resistance is possible.

Within these parameters, I_{app} and R_{eff} cannot be increased without bound; otherwise excessive joule heating from the bias source can lead to overheating and failure of the pixel. Therefore, the main design parameters that can be tailored to increase the responsivity are α, η, β and G. Among these parameters, α (TCR) is the property of the IR sensitive material, and therefore only choosing an IR sensitive material with higher TCR will increase $\Re$. On the other hand, the other parameters depend on the pixel geometry as well as the material properties of the layers forming the pixel.

4.3.4 Noise Equivalent Temperature Difference (NETD)

4.4 Infrared Absorption Model for Thin Single Stage Microbolometer

Uncooled infrared detectors use the absorbed infrared energy for heating the temperature sensitive part. Earlier in this chapter we presented, a method to compute the incoming signal power. However, only a portion of this energy is absorbed by the microbolometer pixel and part of this energy will reflect back. The amount of absorbed energy is determined by the absorption coefficient of the detector. Determining absorption coefficient (η) is important for determining the main performance parameters of a microbolometer, such as responsivity and detectivity [37]. The absorption coefficient also determines the spectral response of the microbolometer. The absorption coefficient also known as coupling efficiency is defined as the ratio of the absorbed power to the incident power. It can be found by solving the transverse electromagnetic (TEM) wave equations.

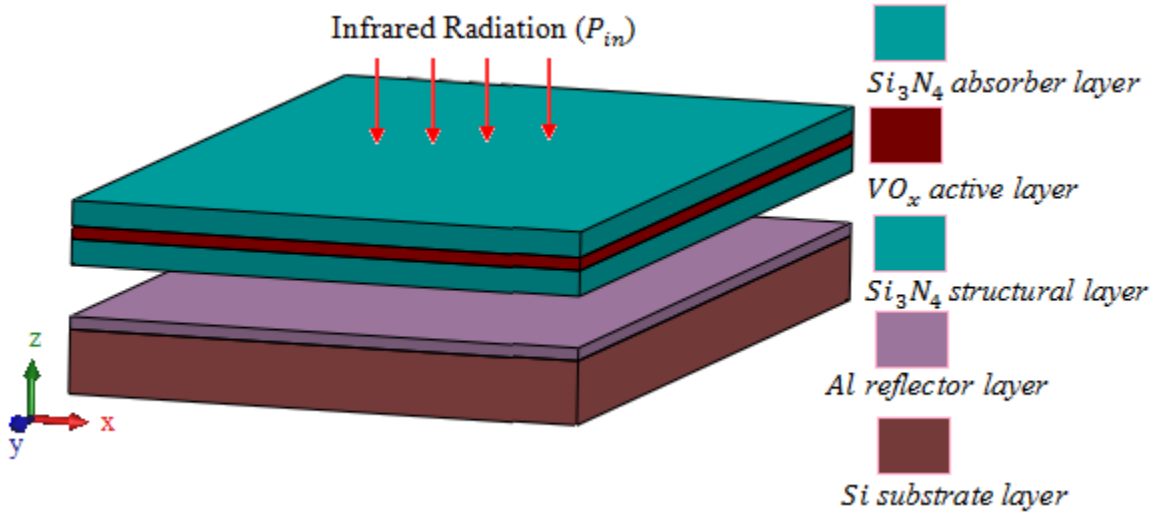

Figure 4.6: Top view and stack layers for region III of Thin Single Stage microbolometer

This section introduces a method to estimate the total absorption coefficient of Thin Single Stage microbolometer with a multiple layer structure and different regions. For Thin Single Stage microbolometer, the detector structure is divided sub-regions having different layer combinations. Region II and IV, as shown in Figure 4.7, has silicon nitride IR absorber, vanadium conductor, aluminum reflect. Region III has sensor layer vanadium oxide in addition to the layers indicated in the other two regions. The absorption coefficient of each sub-region is calculated separately. Then, the area ratios of the sub-regions together with these coefficients are used in order to calculate the total absorption coefficient of the IR detector. The absorption in the required part of the infrared spectrum can be optimized by adjusting the layer properties and layer thicknesses.

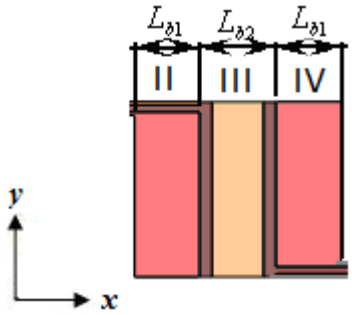

Figure 4.7: Top view of Thin Single Stage microbolometer microplate

4.4.1 Theoretical Background of the IR Absorption

Optical properties of any material are fully determined by the spectral dependence of their complex optical constants which consist of the refractive index $n(\lambda)$ and extinction coefficients $k(\lambda)$ and ($n(\lambda)$, $k(\lambda)$) are known as optical constants. Between the lattice vibration region and the fundamental absorption edge a non-metallic material is transparent and its refractive index diminishes very slowly with wavelength. In most dielectrics this value is almost constant in the visible spectrum and reveals net high-frequency contributions due to excitations in the low-frequency region. Therefore, this value is regarded to be the measure of composition of the dielectric thin films and is measured routinely at the wavelength of He–Ne laser (632.8 nm) by ellipsometry [15]. Knowledge of optical constants of such materials also in the infrared (IR) spectral region helps in analysing their vibration properties, whereby data about the molecular structure and order are obtained.

The absorption coefficient of a given layer stack can be calculated by modeling the layers as cascaded transmission lines. In this model, all the layers are represented by their characteristic impedances. The Transverse Electromagnetic (TEM) wave is assumed to propagate perpendicular to the absorber layer surfaces. The total number of layers, including the air gap and the thin film layers forming the microbolometer pixel, is n. The characteristic wave impedance of a layer i is expressed as [35],

$$Z_i = \sqrt{\frac{\mu_i}{\varepsilon_i}} = \sqrt{\frac{\mu_0}{\varepsilon_o}}\sqrt{\frac{\mu_{r_i}}{\varepsilon_{r_i}}} = Z_o\sqrt{\frac{\mu_{r_i}}{\varepsilon_{r_i}}} \tag{4.25}$$

where μ_{ri} and ε_{ri} are the relative permeability and permittivity of layer *i*. The Cascaded Transmission Lines (CTL) model of a particular detector region can be generated by using these characteristic impedances. For multilayer structures, the propagation constant for layer *i* at a given wavelength λ is defined as [2]

$$k_i = j\,\lambda\sqrt{\varepsilon_{r_i}.\mu_{r_i}.} \tag{4.26}$$

For lossy media, complex relative permittivity is used instead of relative permittivity, given by

$$\hat{\varepsilon}_r = \varepsilon_{r_i} + j\frac{\sigma_i}{\lambda\varepsilon_0} \tag{4.27}$$

where λ is the wave frequency (*rad/sec*), ε_0 is the permittivity of free space, σ_i is the conductivity of layer *i*, and *j* is the imaginary unit. For free space, both the relative permittivity and permeability are equal to one ($\mu_{r_i} = \varepsilon_{r_i}$=1), giving

$$Z_{free\ space} = Z_0 = 377\Omega \text{ (As the free space } \textbf{\textit{impedance}}\text{)} \tag{4.28}$$

Generally, magnetic materials are not used in a microbolometer (i.e. μ_{r_m}=1) and so the equations for Z_i and k_i can be simplified as

$$\begin{aligned} Z_i &= Z_0\sqrt{\hat{\varepsilon}_r} = \sqrt{\frac{\varepsilon_0}{\mu_0}}\sqrt{\varepsilon_{r_i} + j\frac{1}{\omega\rho_i\varepsilon_0}} \\ k_i &= j\omega\sqrt{\hat{\varepsilon}_r} \end{aligned} \tag{4.29}$$

The electric field (E-field) vector for layer *i* at position z ($z_{i-1} \le z \le z_i$) can be written as a summation of two vectors

$$\vec{E}_i(z) = \vec{E}_{i,r}(z) + \vec{E}_{i,l}(z) \tag{4.30}$$

In the above equation, the E-field vectors $\vec{E}_{i,r}(z)$ and $\vec{E}_{i,l}(z)$ correspond to the waves that propagate up from the reflector (positive-y direction) and down to the reflector (negative-y direction), respectively. Similar to Eq. (4.30), the magnetic field (H-field) for layer *i* at position y can be written as a summation of the up-propagating and down propagating vectors.

$$\vec{H}_i(z) = \vec{H}_{i,r}(z) + \vec{H}_{i,l}(z) \tag{4.31}$$

In Eq. (4.30) and (4.31) the electric and magnetic electric filed component of each region can be expressed as,

$$\vec{E}_{i,r}(z) = \hat{z}E_0 e^{-jk_0 z} \qquad \vec{H}_{i,r}(z) = \hat{z}\eta_0 E_0 e^{-jk_0 z}$$
$$\vec{E}_{i,l}(z) = \hat{z}r_i E_0 e^{jk_0 z} \qquad \vec{H}_{i,l}(z) = -\hat{z}r_i \eta_0 E_0 e^{jk_0 z} \tag{4.32}$$

where E_0 is the electric field components of free space

r_i the reflective components of the i[th] medium

In a TEM wave, the electric field $\vec{E}$ and magnetic field $\vec{H}$ and the propagation direction $\hat{k}$ obey the right hand rule. Therefore, the magnetic field (H-field) of a TEM wave that propagates in the k-direction is given by

$$\vec{H} = \hat{k}\, X\, \frac{1}{Z}\vec{E} \tag{4.33}$$

where $\vec{H}$ is the H-field, $\vec{E}$ is the E-field, Z is the wave impedance and $\hat{k}$ is the unit vector in the propagation direction. For a multilayer structure applying the boundary equation at the contact surface, it's possible to compute the reflective (r_o) and transmission components of the wave (t_o). These two terms will be used to compute the total absorption coefficient of the structure as

$$\eta = 1 - \left(\frac{r_0}{t_o}\right)^2 \tag{4.34}$$

4.4.2 Infrared Absorption in a Thin Single Stage Microbolometer

The IR absorption simulations play an important role in the design of the microbolometer structure. These simulations allow determining the optimum thickness of the layers and the sheet resistance of the absorber layer in order to absorber the required maximum IR wavelength. To calculate the amount of IR energy absorbed in the microplate the absorption coefficient is modeled for Thin Single Layer in this section. The representative perspective view of a layer stack in a Thin Single Stage microbolometer pixel is shown in Figure 4.6. This

specific stack is composed of a mirror metal (Al), vacuum cavity, structural layers (Si_3N_4), an active detector material (Vanadium oxide), and an absorber layer in region II. In Eq. (4.30) and (4.31) the electric and magnetic electric filed component of each region can be expressed as, $\vec{E}_{i,r}(z)\ and\ \vec{E}_{i,l}(z)$

Layer 1: vacuum/air medium

$$\begin{aligned} E_{1,r} &= \hat{z}E_0e^{-jk_0y} & H_{1,r} &= \hat{z}\eta_0E_0e^{-jk_0z} \\ E_{1,l} &= \hat{z}rE_0e^{jk_0y} & H_{1,l} &= -\hat{z}r\eta_0E_0e^{jk_0z} \end{aligned} \tag{4.35}$$

Layer 2: silicon nitride absorber

$$\begin{aligned} E_{2,r} &= \hat{z}t_1E_0e^{-jk_1z} & H_{2,r} &= \hat{z}\eta_1t_1E_0e^{-jk_1z} \\ E_{2,l} &= \hat{z}r_1E_0e^{jk_1z} & H_{2,l} &= -\hat{z}\eta_1r_1E_0e^{jk_1z} \end{aligned} \tag{4.36}$$

Layer 3: vanadium oxide (for region III in Figure 4.7)

$$\begin{aligned} E_{3,r} &= \hat{z}t_2E_0e^{-jk_2z} & H_{3,r} &= \hat{z}\eta_2t_2E_0e^{-jk_2z} \\ E_{3,l} &= \hat{z}r_2E_0e^{jk_2z} & H_{3,l} &= -\hat{z}\eta_2r_2E_0e^{jk_2z} \end{aligned} \tag{4.37}$$

Layer 4: silicon nitride structural support

$$\begin{aligned} E_{2,r} &= \hat{z}t_3E_0e^{-jk_1z} & H_{2,r} &= \hat{z}\eta_1t_3E_0e^{-jk_1z} \\ E_{2,l} &= \hat{z}r_3E_0e^{jk_1z} & H_{2,l} &= -\hat{z}\eta_1r_3E_0e^{jk_1z} \end{aligned} \tag{4.38}$$

Layer 5: vacuum medium

$$\begin{aligned} E_{1,r} &= \hat{z}t_4E_0e^{-jk_0z} & H_{1,r} &= \hat{z}\eta_0t_4E_0e^{-jk_0z} \\ E_{1,l} &= \hat{z}r_4E_0e^{jk_0z} & H_{1,l} &= -\hat{z}r_4\eta_0E_0e^{jk_0z} \end{aligned} \tag{4.39}$$

The parameters are formulated below:

$$k_0 = \omega\sqrt{\varepsilon_0\mu_0} \quad \& \quad k = \omega\sqrt{\varepsilon_0\varepsilon_c\mu_0} \tag{4.40}$$

$$\eta_0 = \sqrt{\frac{\mu_0}{\varepsilon_0}} \qquad \& \qquad \eta = \sqrt{\frac{\mu_0}{\varepsilon_0 \varepsilon_c}}$$

where t_i and r_i are transmission and reflection coefficients for layer i, respectively in Figure 4.6 Therefore, the H-filed of the wave that propagates to the right $\vec{H}_{i,r}(z)$ and to left $\vec{H}_{i,l}(z)$ can be found as follows

$$\begin{aligned} \vec{H}_{i,r}(z) &= \hat{z}\, x\, \frac{1}{Z_i} E_{i,r}(z) = \hat{z} \frac{1}{Z_i} t_i E_o e^{-jk_i z} \\ \vec{H}_{i,l}(z) &= \hat{z}\, x\, \frac{1}{Z_i} E_{i,l}(z) = -\hat{z} \frac{1}{Z_i} t_m E_o e^{-jk_i z} \end{aligned} \tag{4.41}$$

In this model, it is also assumed that the mircomirror (aluminum reflector) reflects back all of the radiation normally incident on it. Taking all of these into account, the boundary conditions can be written as follows.

First Boundary: (y = 0)

$$\begin{aligned} &E_{1,r}(0) + E_{1,l}(0) = E_{2,r}(0) + E_{2,l}(0) \\ &H_{1,r}(0) + H_{1,l}(0) = H_{2,r}(0) + H_{2,l}(0) \\ &1 + r_o = t_1 + r_1 \\ &1 - r_o = \frac{\eta_1}{\eta_0}(t_1 - r_1) \end{aligned} \tag{4.42}$$

Second Boundary: (z = z_1= absorber $_{thk}$.)

$$\begin{aligned} &E_{2,r}(z_1) + E_{2,l}(z_1) = E_{3,r}(z_1) + E_{3,l}(z_1) \\ &H_{2,r}(z_1) + H_{2,l}(z_1) = H_{3,r}(z_1) + H_{3,l}(z_1) \\ &t_1 e^{-jk_1 z_1} + r_1 e^{jk_1 z_1} = t_2 e^{-jk_2 z_1} + r_2 e^{jk_2 z_1} \\ &t_1 e^{-jk_1 z_1} - r_1 e^{jk_1 z_1} = \frac{\eta_2}{\eta_1}\left(t_2 e^{-jk_2 z_1} + r_2 e^{jk_2 z_1}\right) \end{aligned} \tag{4.43}$$

Third Boundary: (z = z_2= absorber $_{thk}$. + Vox $_{thk}$.)

$$
\begin{aligned}
&E_{3,r}(z_2) + E_{3,l}(z_2) = E_{4,r}(z_2) + E_{4,l}(z_2) \\
&H_{3,r}(z_2) + H_{3,l}(z_2) = H_{4,r}(z_2) + H_{4,l}(z_2) \\
&t_2 e^{-jk_2 z_2} + r_2 e^{jk_2 z_2} = t_3 e^{-jk_2 z_1} + r_3 e^{jk_2 z_2} \\
&t_2 e^{-jk_2 z_2} - r_2 e^{jk_2 z_2} = \frac{\eta_1}{\eta_2}\left(t_3 e^{-jk_2 z_1} + r_3 e^{jk_2 z_2}\right)
\end{aligned}
\tag{4.44}
$$

Fourth Boundary: (z = z_3= absorber $_{thk.}$ + Vox $_{thk.}$ + Si3N4 bottom$_{thk.}$)

$$
\begin{aligned}
&E_{4,r}(z_3) + E_{4,l}(z_3) = E_{5,r}(z_3) + E_{5,l}(z_3) \\
&H_{4,r}(z_3) + H_{4,l}(z_3) = H_{5,r}(z_3) + H_{5,l}(z_3) \\
&t_3 e^{-jk_3 z_3} + r_3 e^{jk_3 z_3} = t_4 e^{-jk_3 z_3} + r_4 e^{jk_3 z3_2} \\
&t_3 e^{-jk_3 z_3} - r_3 e^{jk_3 z_3} = \frac{\eta_0}{\eta_1}\left(t_4 e^{-jk_3 z_3} + r_4 e^{jk_3 z_3}\right)
\end{aligned}
\tag{4.45}
$$

Fifth Boundary: (z = z_4 = absorber$_{thk.}$ + Vox$_{thk.}$ + Si3N4 bottom$_{thk.}$ + Al$_{thk.}$)

$$
\begin{aligned}
&E_{5,r}(z_4) + E_{5,l}(z_4) = 0 \\
&t_4 e^{-jk_2 z_4} + r_4 e^{jk_2 z_4} = 0
\end{aligned}
\tag{4.46}
$$

Taking t_N as the initial point, one can recursively find t_n and r_n in terms of r_N, where n equals N-1 at the first iteration and n = 0 at the last iteration. The iterations end as r_0 and t_0 are found. The coupling efficiency η is found by using the coefficients t_0 and r_0. The overall reflection coefficient, which is defined as the ratio of the amplitude of the reflected wave to the amplitude of the incident wave as given in Eq. 4.41

Therefore, the absorber power in each region can also be expressed as

$$
P_{abs} = \eta P_{Signal} = \left(1 - \left(\frac{r_o}{t_o}\right)^2\right) P_{Signal} \tag{4.47}
$$

Where, P_{abs} is the absorbed power, and P_{Signal} is the incoming power. This equation gives the absorbed power of a particular region in the detector. If we assume that the detector is composed of m regions having different absorption characteristics and nonmagnetic layers, the incident power and absorbed power on a particular region can be expressed as [35]

$$P_{abs} = \frac{1}{2}\eta \int_{S_x} \left(\vec{E}_{in}\, X\, \vec{H}_{in}\right) \overrightarrow{dA} = \frac{1}{2}\eta A_x \frac{E_0^2}{\eta_0} \tag{4.48}$$

where E_{in} is the incoming electric field, H_{in} is the incoming magnetic field, A is the total area of the detector, P_{abs_x} is the absorbed power in a particular region, $\tilde{A}_x$ is the reflection coefficient of this region, and A_x is the area of the particular region. The total absorbed power can be found by adding the absorbed power of the particular regions. Then, the percentage of the absorbed power of the detector can be expressed as,

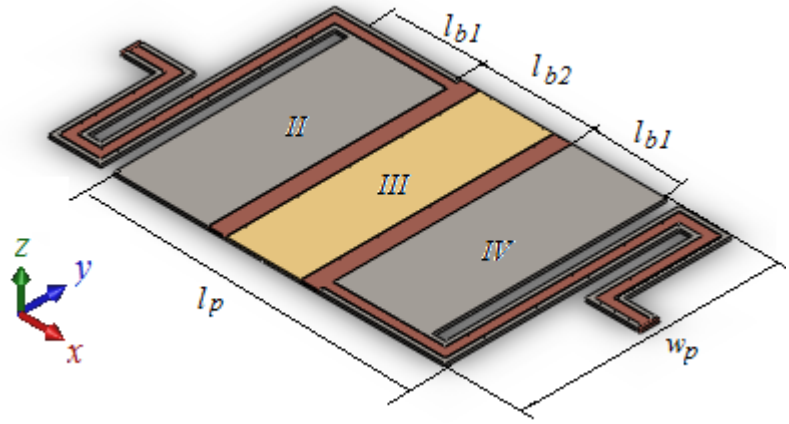

Figure 4.8: Thin Single Stage microbolometer microplate effective IR absorber regions (II-IV)

$$P_{abs} = \left(P_{abs\_1} + P_{abs\_2} + \cdots + P_{abs\_m}\right) \tag{4.49}$$

where, P_{abs} is the total percentage of the absorbed power.

P_{abs_1}, P_{abs_2}, ... P_{abs_m} are the IR absorbed energy per unit volume

This means that the total percentage of the absorbed power can be found by taking the weighted average of the absorbed powers of the individual regions with respect to the area occupied by the regions.

4.4.3 IR Absorption Simulation Results

The absorption simulations play an important role in the design of the microbolometer structure because it can allow determining the optimum thickness of the layers easily. The Cascaded Transmission Lines (CTL) model explained in the previous section can be used to estimate the absorption coefficient of a microbolometer detector. These simulations mainly determine the thickness of the sacrificial layer and the sheet resistance of the absorber layer. The Cascaded Transmission Lines (CTL) model explained in previous sections was used to estimate the absorption coefficient of a Thin Single Stage microbolometer detector. The model is developed in Matlab® code and simulates the IR absorption for the Thin Single Stage microbolometer using material properties and device geometry.

To provide a high absorption of the radiation in the bolometer membrane, microbolometer design contains resonant optical cavity (Fabry-Perot) structures that are optimized for the targeted wavelength interval. The most commonly used resonant optical cavity design is an air gap between the microplate and the infrared mirror (aluminum). The resonant optical cavity is placed at a distance of $\lambda/4$ from the mirror surface on the substrate for the required wavelength (λ) of interest. Therefore for a 2.5 μm air gap the expected maximum absorbed wavelength will be 10 μm.

Using the analytical model developed for Thin Single Stage microbolometer, the maximum absorption wavelength of 9.5 μm computed which is slightly lower than the expected 10 μm. In fact, microbolometers designed to operate in certain wavelength range, for example from 8 μm to 12 μm with a pick value of 10 μm. The model also simulate, the Thin Single Stage microbolometer structure absorbed 92% the incoming signal at the 9.5 μm wavelength. This absorption coefficient has been used to compute the absorbed IR energy in the electro-thermal numerical model.

When the air gap thickness changed from 2.5 μm to 2 μm the maximum absorption wavelength changed to 8 μm as expected. The gap design requires $\lambda/4$ for the maximum wavelength, λ absorptions. Generally, the assumption for the calculations is that the active layer is kept in the

vacuum and a single pass of the radiation through the active layer is allowed. On the other hand, further increases in active layer thickness would increase the thermal mass of the detector, which would increase the time constant and reduce the frame rates for the detector array. The proposed method can also be used for double stage microbolometer detectors.

Chapter Five

Modeling Results and Discussion

Chapter three presented a detailed analysis of the analytical and numerical models developed for a Thin Single Stage microbolometer and PolyMUMPs® test device. In order to compute the IR energy absorbed by the pixel, in the previous chapter a coupling efficiency model for a Thin Single Stage microbolometer was developed. This chapter uses these models, along with the FEM simulation software ANSYS®, to simulate the electro-thermo mechanical characteristics of a Thin Single Stage microbolometer and PolyMUMPs® test device. Results from the simulations are compared to experimental data gathered using the PolyMUMPs® test device. The models are then used to determine how the Thin Single Stage might be optimized in order to obtain desired performance and reliability characteristics for specific applications.

This chapter begins with a description of the Matlab® GUI interface developed to simulate the analytical and numerical models. This is followed by a discussion of the electro-thermal analytical model simulation results (Section 5.2) and electro-thermal numerical simulation results (Section 5.3). In Section 5.4, the FEM simulation results, using a commercial software ANSYS®, for electro-thermal and thermo-mechanical analysis are presented. The IR absorption model results, which were used to compute the absorbed IR energy for the numerical model, are presented in Section 5.5. Based on the results, the effects of microplate size and gap thickness on spectral absorption are discussed. Finally, Section 5.6 provides a comparison between the PolyMUMPs® test device deflection results of the ANSYS® FEM simulation and the experimental results.

5.1 GUI Matlab® Code for Analytical and Numerical Model

The analytical and numerical models have been developed with Matlab® graphical user interface (GUI) as shown in Figure 5.1. As can be seen in the figure, various options are included to facilitate the use of the models. The Matlab® GUI design helps to select the geometric parameters, operating environments, solution methods, type of input loads and many other

options. The numerical model includes an IR energy source and radiation heat transfer mechanisms. Furthermore, it can easily be modified for temperature dependent material properties, such as conductivity, resistivity and Young modulus. As part of the Matlab® program output, the temperature distribution can be plotted for both air and vacuum environments using the analytical and numerical models developed in Chapter three. The temperature distribution simulated from these models provides critical information about the performance and reliability of the device. Using the simulated thermal distributions, the performance parameters of the microbolometer, such as the time constant, responsivity and noise equivalent temperature difference (NETD) can also be computed.

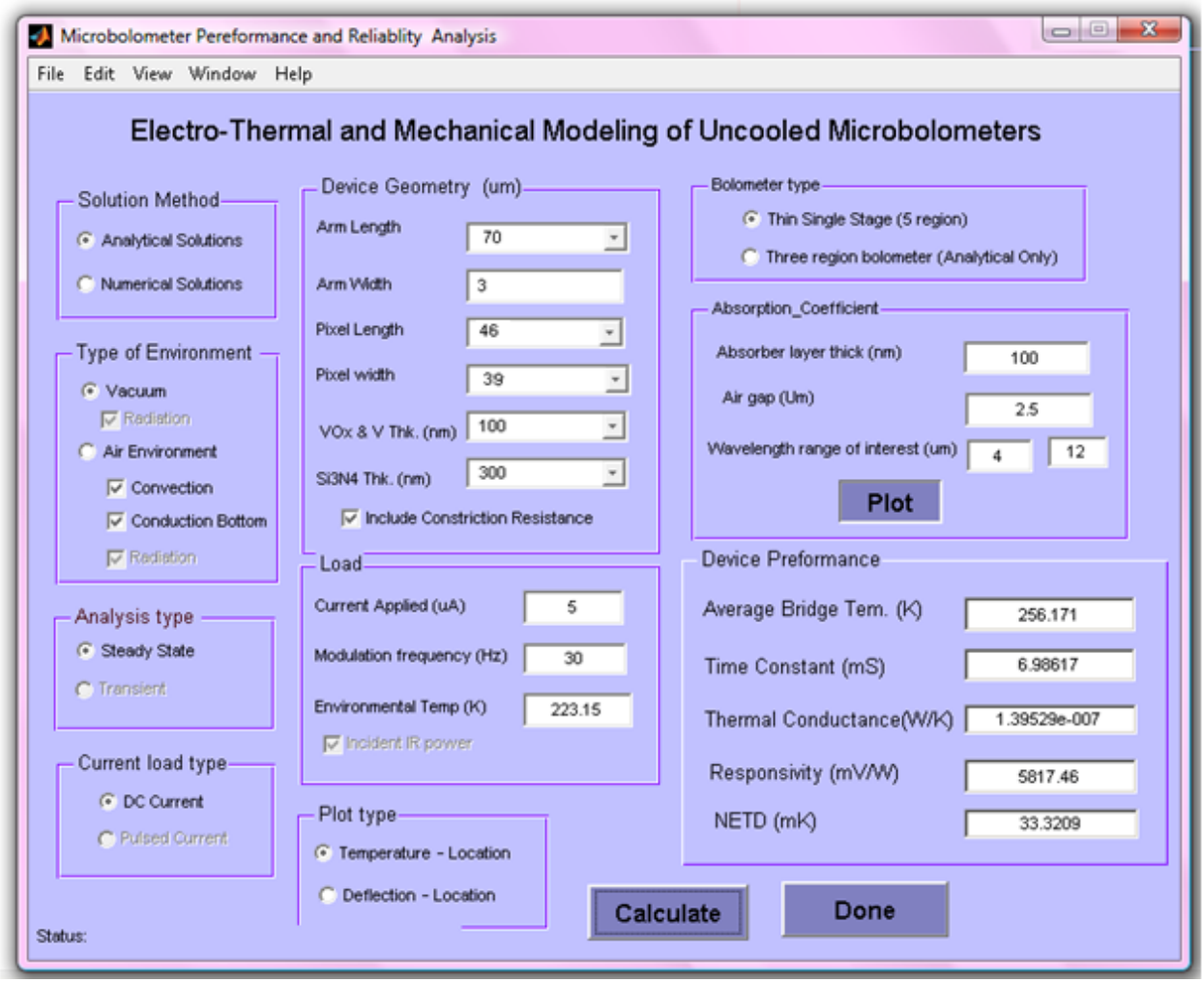

Figure 5.1: Matlab® GUI for the Thin Single Stage microbolometer analytical and numerical models

5.2 Electro-Thermal Analytical Results

To evaluate the functionality of the analytical model, the steady-state electro-thermal characteristics of the Thin Single Stage microbolometer and the PolyMUMPs® test device have been studied and are presented here. The model has been simulated for different environments, geometries and load conditions. In the subsequent sections, simulation results that take into account the geometric dimensions and material properties presented in Chapter two are presented. The analytical model is simulated in air and vacuum environments to obtain the thermal distribution across the Thin Single Stage and PolyMUMPs® test device structures. During the initial test, prior to this study, the actual Thin Single Stage device was burned at the contact point between the legs and microplate when applied 10 μA. Therefore in the subsequent section, we were more interested to simulate the temperature distribution for a current load up to 10 μA.

5.2.1 Electro-Thermal Simulation for Thin Single Stage

The temperature distribution at any given time provides valuable information about the microbolometer performance that can ultimately be used to predict thermal failure. Hence, one of the main objectives of this study was to predict the temperature distributions across the microbolometer structure. The temperature distribution across the length of the Thin Single Stage microbolometer was simulated for a range of current loads. The thermal distribution for a 5 μA current load in an air environment is shown in Figure 5.2. It can be observed that for the Thin Single Stage microbolometer, although the larger microplate cross section area reduces the thermal and electrical resistance of the sensing area, the temperature reaches its peak at the center, in region III. This is due to the fact that the higher electrical resistivity value of vanadium oxide (VOx), compared with vanadium of the legs part, causes a higher joule heat generation at the center of the microplate. Furthermore, the higher thermal conductivity of vanadium also introduces a higher thermal gradient along the legs (regions I and V). Hence, material properties, such as electrical resistivity and thermal conductivity, are important factors that greatly influence the magnitude and position of temperature distributions across the device.

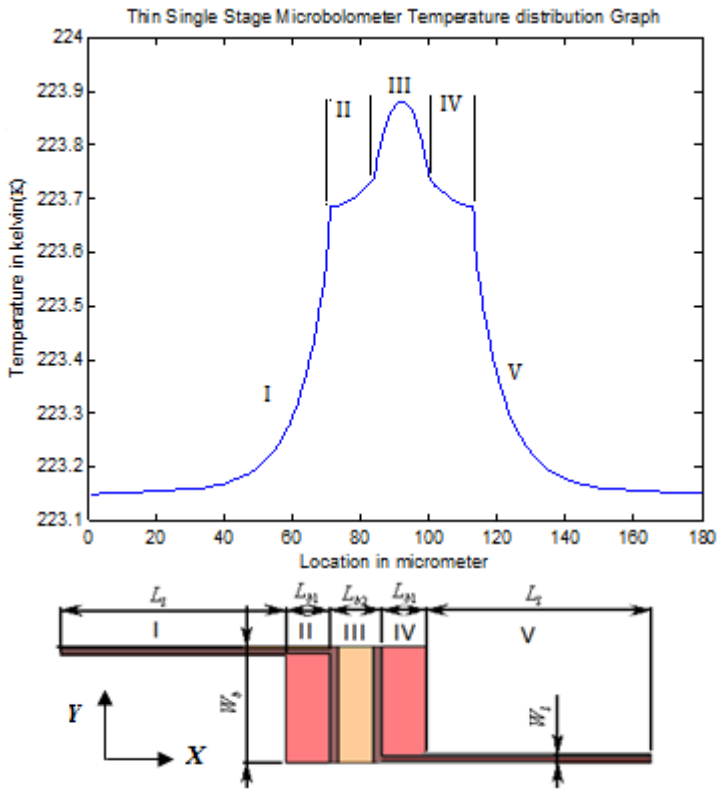

Figure 5.2: Temperature distribution for a 5 μA in air environment for TSS microbolometers.

Microbolometers are mostly designed to operate in a vacuum environment to reduce the thermal conductance and hence decrease the time constant of the device. Thus, the Thin Single Stage microbolometer has also been simulated in a vacuum environment, where only heat transfer via the leg is considered. Therefore, convection and heat conduction via air to the substrate was eliminated from Eq. (3.19). The device was simulated for a range of current loads and the temperature distribution has the same profile across the device, but differs in magnitude.

The temperature distribution for a 5 μA current load in a vacuum environment is plotted in Figure 5.3. Comparing Figures 5.2 and 5.3, it can be seen that temperature profiles developed in a vacuum environment differ noticeably from those simulated in an air environment. In a vacuum, the microplate temperature rises up to the steady-state condition and eventually becomes the highest temperature area, since heat is only conducted via legs to the substrate. Furthermore, the Thin Single Stage microbolometer reaches steady-state peak temperatures of 257.35 K with a 5 μA current load in a vacuum, whereas it will only reach 223.9 K with the same

load in an air environment. These results indicate that, the effect of heat conducted from the microplate to the substrate via air significantly reduces the temperature of the Thin Single Stage microbolometer in an air environment.

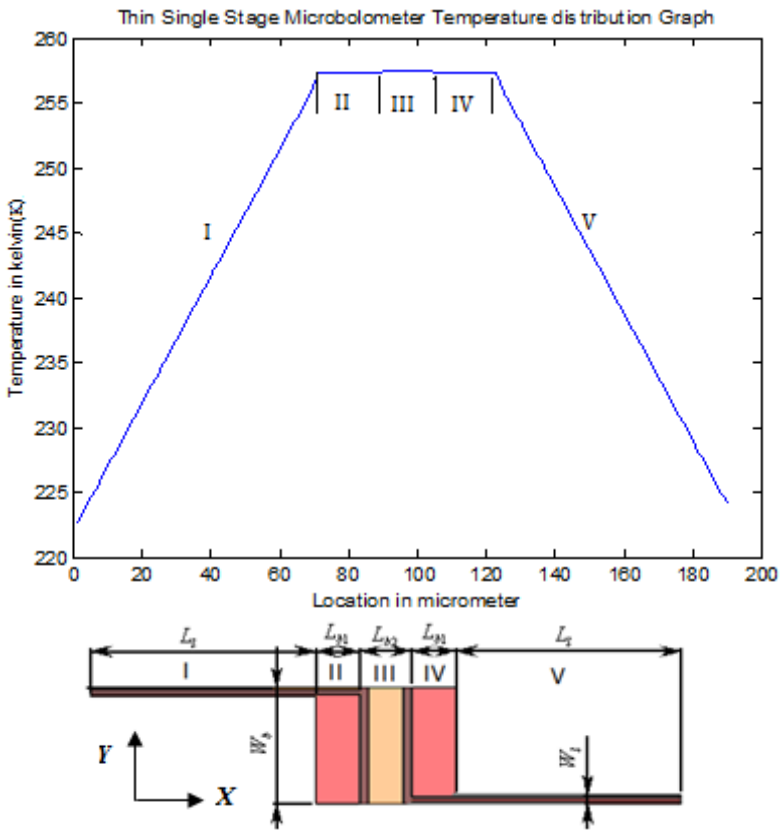

Figure 5.3: Steady-state temperature distribution for a 5 μA current load applied in a vacuum environment.

At steady state the temperature distribution across the microplate, comprising regions II, III, and IV, has only a small gradient in the vacuum condition. This effect is characterized by the thermal conductivity of silicon nitride and vanadium oxide layers, which used to fabricate the microplate regions II, III, and IV. Both materials have the same thermal conductivity, therefore heat flow with the same rate as the total cross section area remain constant. The vanadium layer on top of the microbolometer legs, comprising regions I and V, has a higher thermal conductivity than both silicon nitride and vanadium oxide and heat energy transfers much faster in this region than in the microplate areas, as shown in Figure 5.3.

Generally, the temperature distribution trend in vacuum is similar for other materials including for the test device, which was fabricated with gold and polysilicon. This supports the assumption that the heat conduction via the material is much more significant than any other mechanism of heat transfer considered in the model. In air, the effect of heat conduction to the substrate creates a considerable temperature reduction and change the temperature distribution plot for the same current load as shown in Figures 5.2 and 5.3.

Table 5.1 summarizes the variation of both average microplate temperature and the time constant as a function of applied DC current in both air and vacuum conditions. As can be inferred from these results, the magnitude of temperature increase is much higher in the vacuum condition than in the ambient air condition. Also, the thermal time constant is much larger during operation in vacuum.

Table 5.1: Variation of temperature change and time constant for different applied currents

Current (μA)	**Average Temp. Increase (*K*)**		**Time Constant (*ms*)**	
	Air	**Vacuum**	**Air**	**Vacuum**
1	0.016	4.095	0.022	8.61
5	0.41	33.17	0.086	6.98
10	1.61	42.372	0.091	2.46
15	3.41	44.717	0.089	1.17

The analytical model was also simulated for different dimensions and material properties using the GUI interface. In general, the magnitude of temperature increase is highly dependent on the material properties of the device, particularly the electrical resistivity and thermal conductivities of each layer. For instance, to study the effect of the electrical resistivity in the temperature distribution, the resistivity of the vanadium oxide layer is used in the legs instead of vanadium resistivity (3.0×10^{-7} Ωm). In this case, the steady-state temperature distribution for a for Thin Single Stage microbolometer reaches a maximum at the legs, as indicated in Figure 5.4. Also, the center of the plate has a lower temperature, partly due to the larger cross section of the pixel area (i.e. the sensitive area) compared to the vanadium conductor in the legs. The larger cross section

area reduce the thermal and electrical resistivity and hence lower the temperature. As a result, we can assert that the external thermal resistance influences the location of the maximum temperature and hence, the temperature profile across the bolometer.

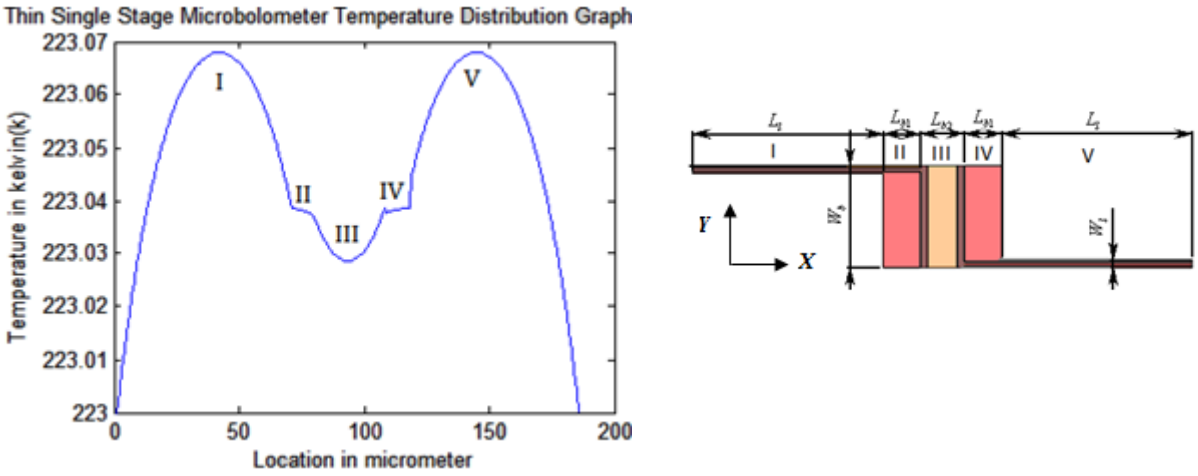

Figure 5.4: Steady state temperature distribution for a 5 μA current load in air environment, assuming that the resistivity of the vanadium oxide used in the microplate the same as that of the vanadium.

Finally, the results shown in each of the above figures demonstrate the effect of the non-uniform power density. As the applied current increases, more power is dissipated at the points having higher temperature, thus the position of maximum temperature shifts towards the legs. For this reason, the position of maximum temperature is largely dominated by relative values of conduction thermal resistance and external thermal resistances. In the case of an air environment, the location of maximum temperature is largely determined by the thermal conductance and electrical resistance of the materials as well as by the applied current. The thickness of both vanadium and vanadium oxide will considerably affect the temperature change and in fact could be a potential reason for failure due to high temperature generation in these layers. On the other hand, the thickness of silicon nitride (Si_3N_4) does not notably affect the temperature change although it affects the time constant.

5.2.2 PolyMUMPs® Test Device Analytical Model

The Matlab® code was modified for PolyMUMPs® test device geometric structure and materials. The geometrical model design was revised with the proper dimension measured from the optical profiler. The material properties were derived from the PolyMUMPs® manual, as listed in Chapter two. The temperature distribution of the PolyMUMPs® test device output in both air and vacuum conditions is shown in Figure 5.5 and Figure 5.6, respectively. In both cases, the temperature distribution across the length of the microbolometer was plotted for an input current of 10 *mA* (~0.8V). The effects of air conduction from the microplate to the substrate cause the temperature to decrease in the microplate region. Furthermore, the test device temperature distribution in the air environment is quite different from that plotted for the Thin Single Stage microbolometer due to structural and material composition differences.

However, for vacuum conditions the temperature reaches its peak at the center as in the case of the Thin Single Stage microbolometer, as indicated in Figure 5.6. The temperature distribution in vacuum environment is expected to simulate a maximum value in the middle of the microplate. This is mainly because, heat energy only conducted via legs to the substrate and heat energy build up in the microplate area causing a maximum temperature in this region.

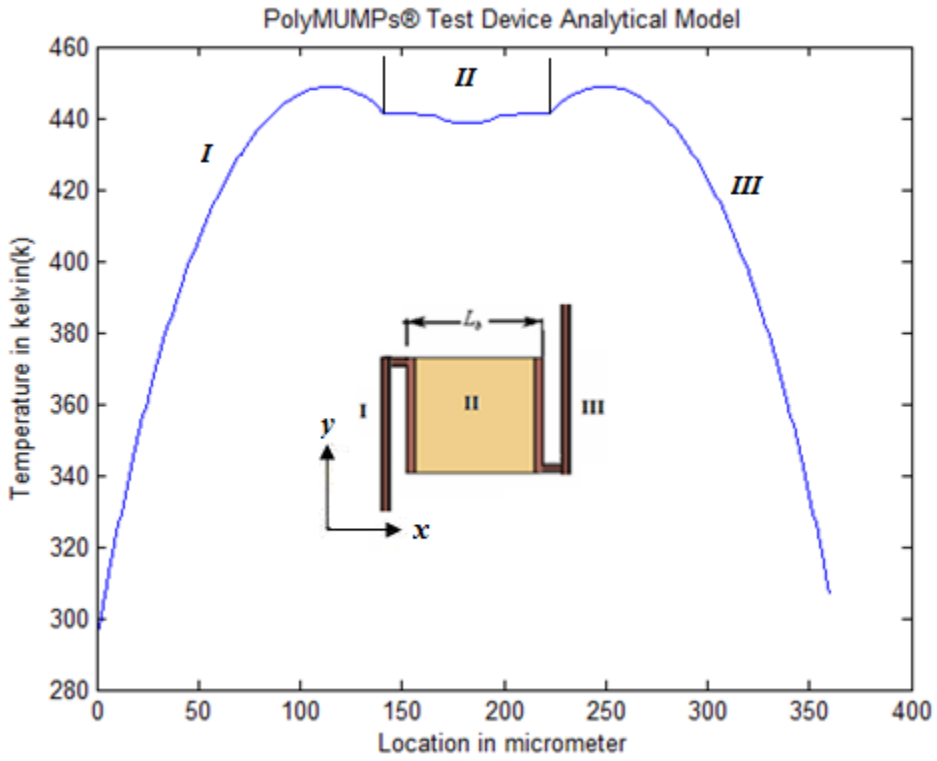

Figure 5.5: Temperature distribution for a 10 mA (0.8V) in air for PolyMUMPs® test device.

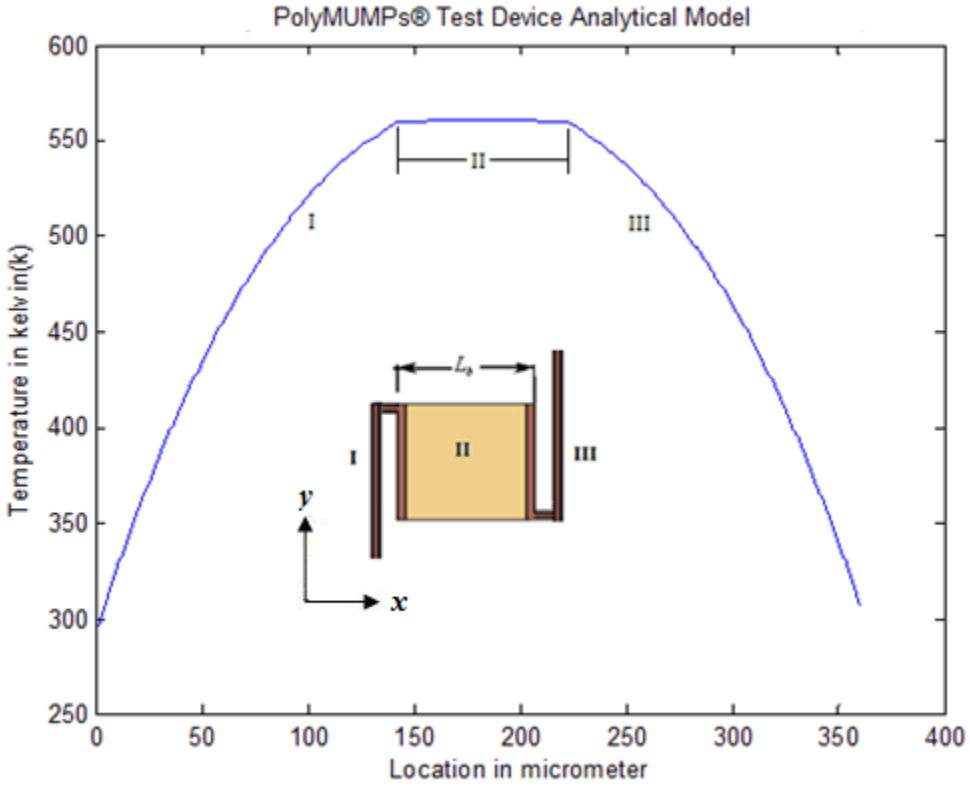

Figure 5.6: Temperature distribution for a 10 mA (0.8V) in vacuum for PolyMUMPs® test device.

5.3 Numerical Model Result for Thin Single Stage

The numerical model is the most comprehensive analysis that includes all heat transfer mechanisms and heat energy sources. The model simulates both steady-state and transient conditions with joule heating and an IR radiation heat source. The numerical model is also capable of including temperature dependent material properties, such as conductivity, heat capacitance, and resistivity. However, most of these temperature dependent material properties were not available during the present research and only temperature dependent electrical resistivity included in the following simulations.

First, in order to compare the numerical model with the analytical model, the results in the subsequent sections were simulated at the same operating condition. A Finite Difference Method (FDM) was developed to solve the time-dependent temperature field for the multilayer microbolometer structure. An approximation to the solution function was calculated at discrete spatial mesh points, proceeding in discrete time steps. The starting values were derived from an initial value condition, in which case the microbolometer is assumed to have the substrate temperature. For Thin Single Stage microbolometers presented here, initial values of all inner and outer grid points were set at 223.15 K (-50 ^{o}C).

Boundary conditions are constant values at the anchor connection of the legs to the substrate with 223.15 K. The temperature was computed for each node in the analysis. As in the case of the analytical models when simulated in the vacuum environment, the only source of heat transfer is conduction of heat to the substrate through the legs. The FDM solver has been used for a different number of nodes, and indicates that the calculated solutions monotonically converge to a stable value for the node numbers greater than 800. At steady state, the average microplate temperature and the maximum temperature for a range of current loads was recorded and presented in Table 5.2. Previously we noted the effective of resistively on the thermal distribution using the analytical model. For Thin Single stage the main joule energy source is vanadium oxide of the pixel structure due to its higher electrical resistivity. Since vanadium oxide has a negative TCR value, the resistivity reduces as the temperature increase. This effect cause the temperature increase to taper as the applied current increase as shown in Table 5.2

Table 5.2: Numerical model results in vacuum condition for Thin Single Stage microbolometer

Current (μA)	Average micro plate Temp. (*K*)	Maximum Temp (*K*)	Average microplate Temp. Increase (*K*)
0	223.15	223.15	0
1	228.90	229.23	3.753
2	238.61	239.87	13.46
3	248.00	250.32	24.85
4	253.41	256.01	30.26
5	256.58	259.6	33.65
6	258.99	261.23	33.84
7	260.46	264.01	37.31
8	261.49	266.32	38.34
9	261.66	266.85	38.51
10	262.80	267.26	39.65
12	263.15	267.34	40.00
14	263.72	268.47	40.57
16	264.11	269.56	40.96

A temperature distribution for 5 μA current loads in the vacuum condition, which was evaluated as the stable solution to the heat equation, can be seen in Figures 5.7 - 5.10. The figures indicate that the temperature reaches its peak value at the center of microplate, as computed in the analytical model. Furthermore, the temperature is shown to decrease significantly on the legs, which is mainly attributed due to the high thermal conductivity of vanadium. The same temperature gradient has been observed for the legs when simulated using the analytical model.

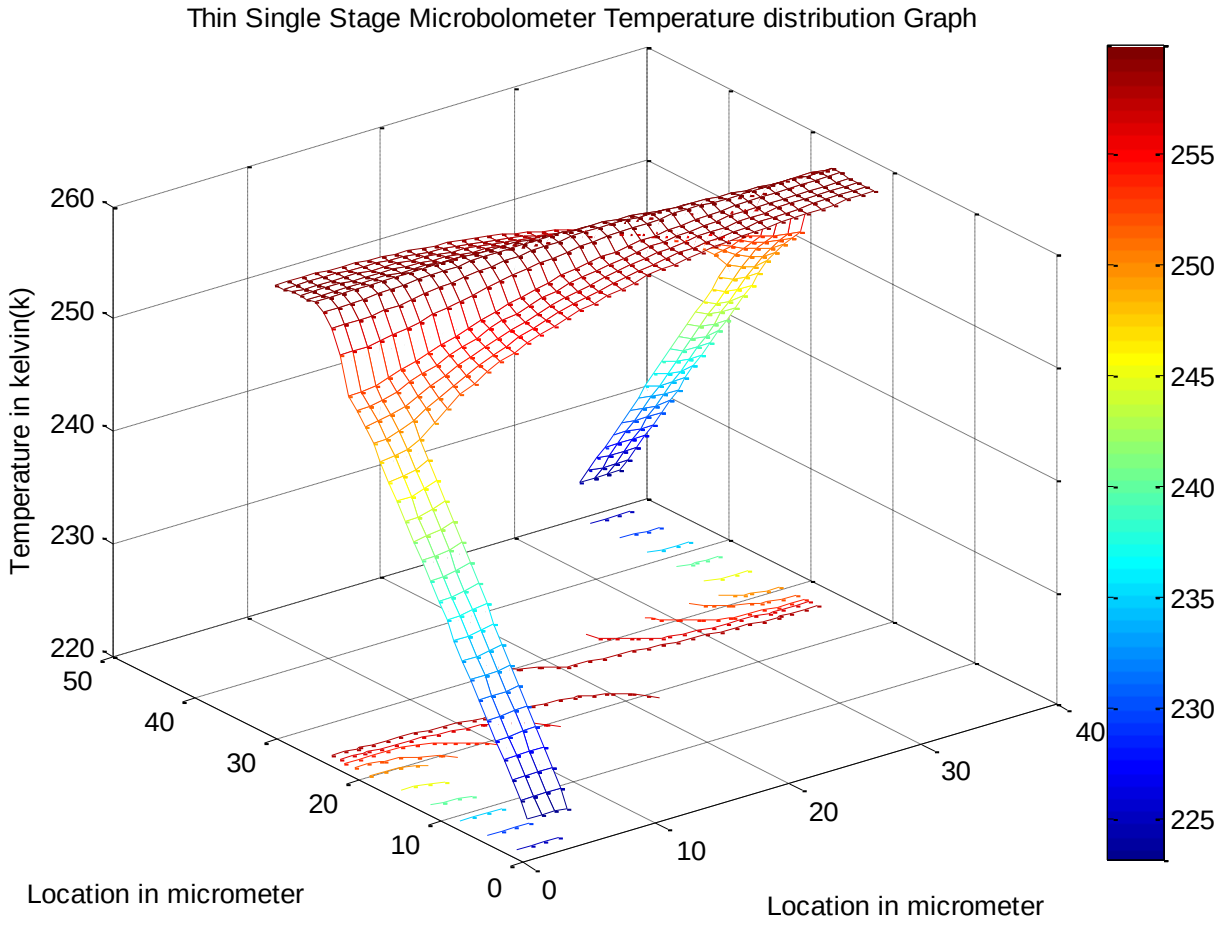

Figure 5.7: Steady state temperature distribution (numerical model) for a 5 µA current load in vacuum for a Thin Single Stage microbolometer without the effect of radiation heat dissipation

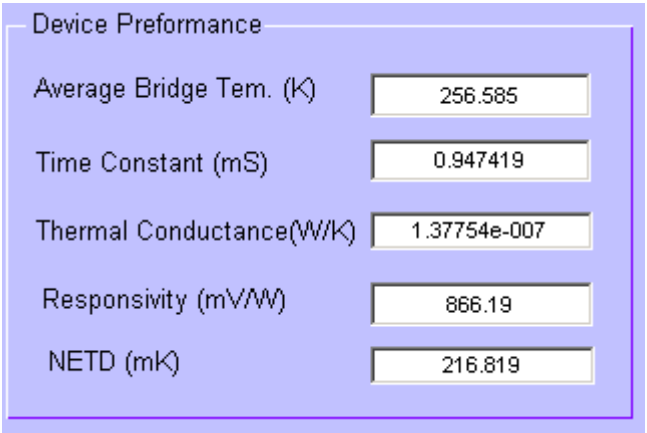

Figure 5.8: Performance parameters computed for a 5 µA in vacuum for a Thin Single Stage.

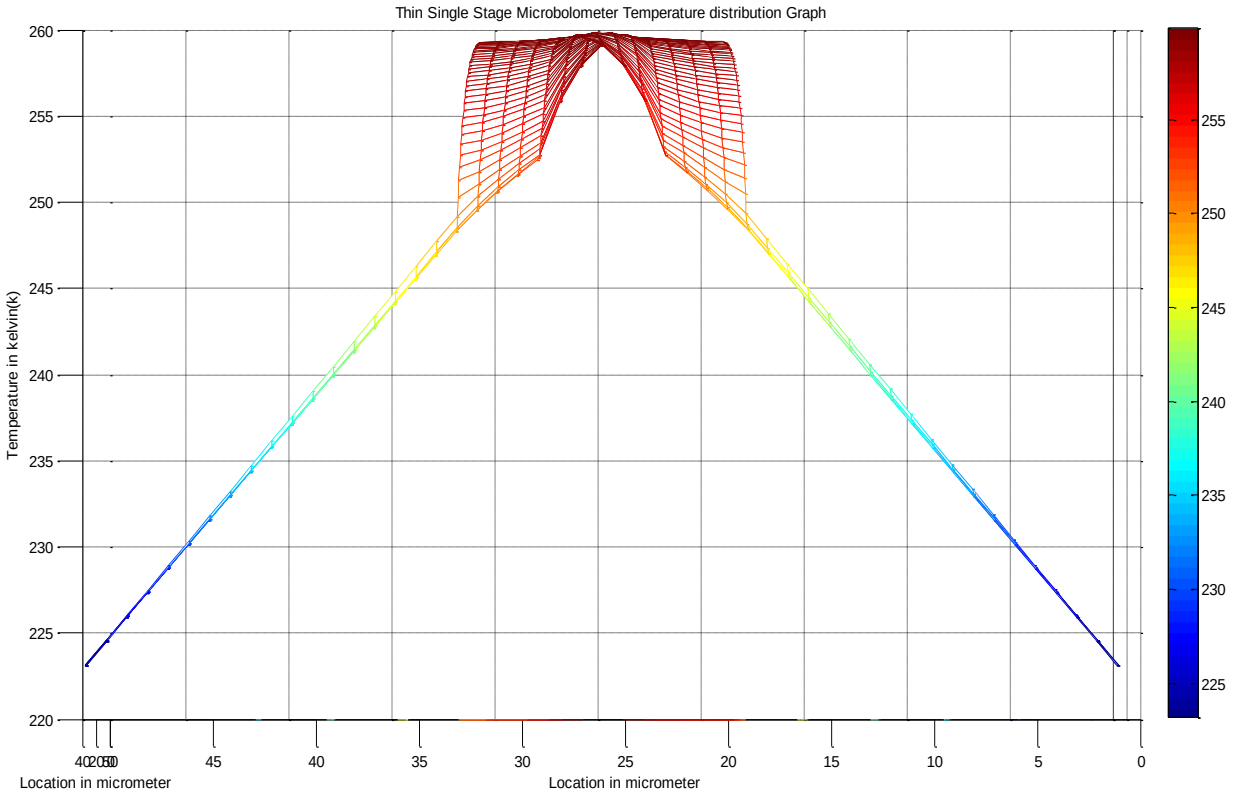

Figure 5.9: Steady state temperature distributions (numerical model) for a 5 µA current load in vacuum for a Thin Single Stage microbolometer without the effect of radiation heat dissipation

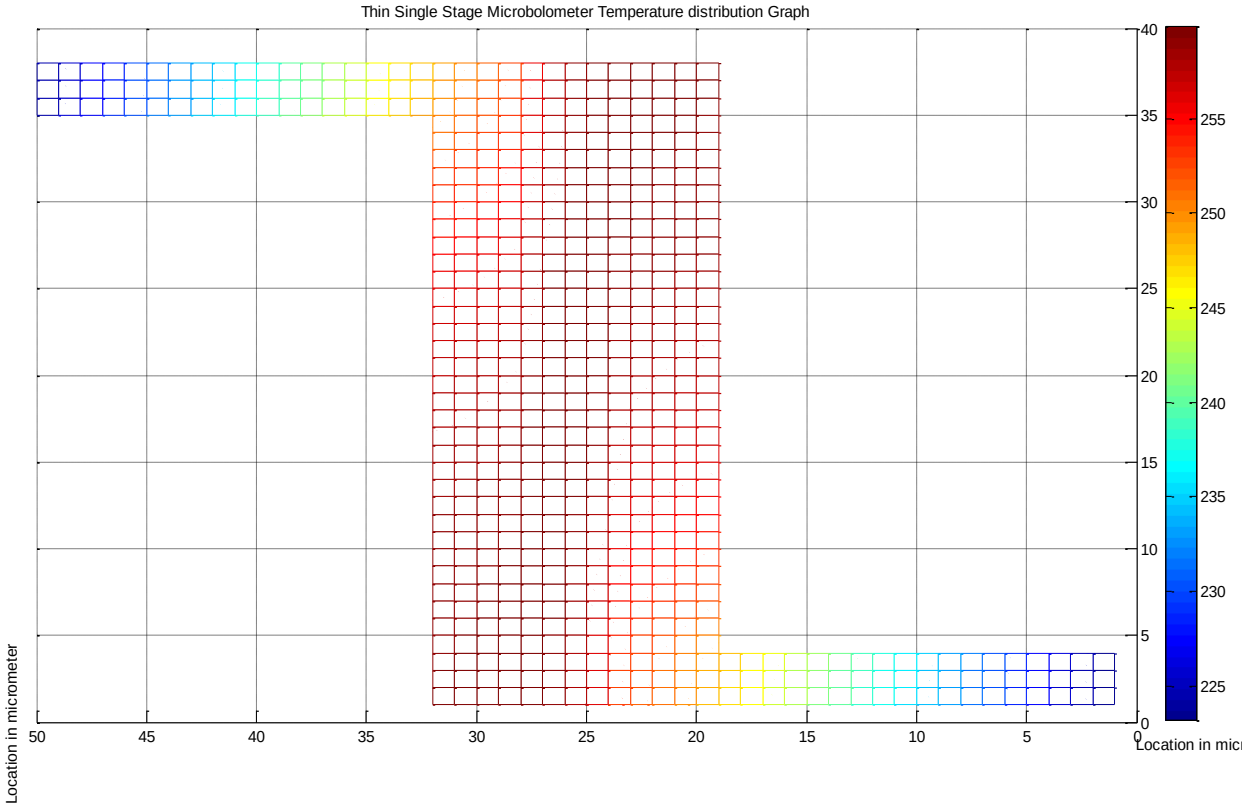

Figure 5.10: Steady state temperature distribution (numerical model) for a 5 µA current load in vacuum for a Thin Single Stage microbolometer without the effect of radiation heat dissipation

5.3.1 Effect of Radiation Heat Loss

To investigate the characteristics of all heat loss mechanisms, the numerical model was simulated including the effect of radiation heat loss as an additional boundary condition. As presented in the previous simulation results, Thin Single Stage microbolometers operating in vacuums, without the effect of radiation heat dissipation, generate low thermal distributions (<275K) at 10 µA current loads. The effect of radiation heat dissipation to the surroundings at this low temperature is negligible [8]. However, even a small thermal radiation effect could considerably affect microbolometer performance since the absorbed IR energy is very small and could have a close order magnitude of radiation heat loss. In order to characterize the effect of radiation, this component was added to the numerical model and simulated. The applied current vs. temperature plot for the Thin Single Stage microbolometer shown in Figure 5.11 indicates

that the effect of radiation computed in the model is very small for low temperature ranges. From this figure, it can be observed that at lower temperature the effect of radiation is minimal for the average microplate temperature but the temperature difference increase steadily as current loads increase.

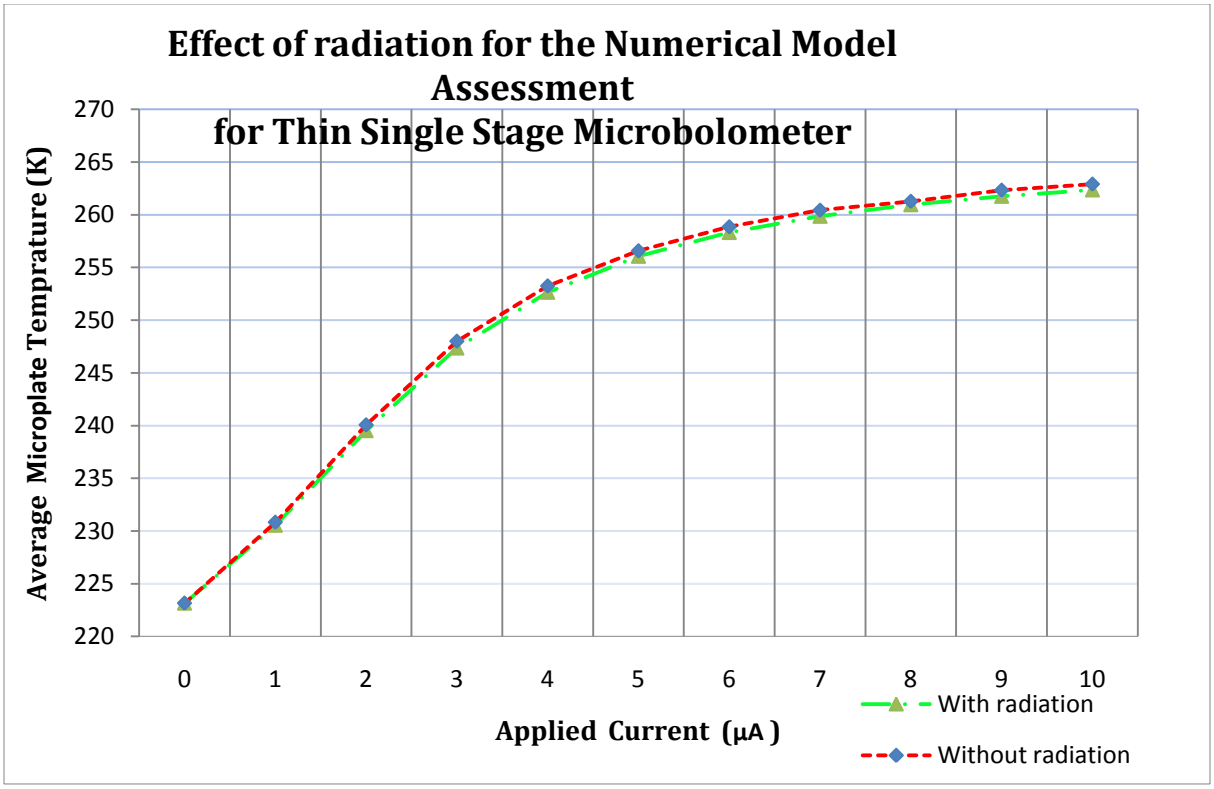

Figure 5.11: The electro-thermal model result with and without the effect of radiation

5.3.2 Effect of Infrared Energy

The numerical model was used to simulate IR energy absorbed in addition to joule heating of the microplate structure and thermal distributions were computed for a range of applied currents. Microbolometers absorb IR radiation and convert it into thermal energy. The addition of thermal energy in the absorber microplate causes the microplate temperature to increase and further changes some of its electrical properties. Typically, the temperature increase causes a concomitant increase in the electrical resistance of the sensing material, which is measured with a Complementary Metal-Oxide Semiconductor (CMOS) circuit. Therefore, modeling the effect of

incoming IR energy is very important. In section 4.4, the IR absorption coefficient model was used to compute the amount of energy absorbs from an incoming IR signal for Thin Single Stage microbolometer. Equation 3.63 was used with the IR absorption coefficient model to compute the absorbed IR energy. Thin Single Stage microbolometer applied with a range of current loads and constant and a constant IR energy sourced with a pick for 10 μm wavelength value. Figure 5.12 shows the temperature variation of a for joule heating (without IR) and both joule heating and IR heat energy (with IR).

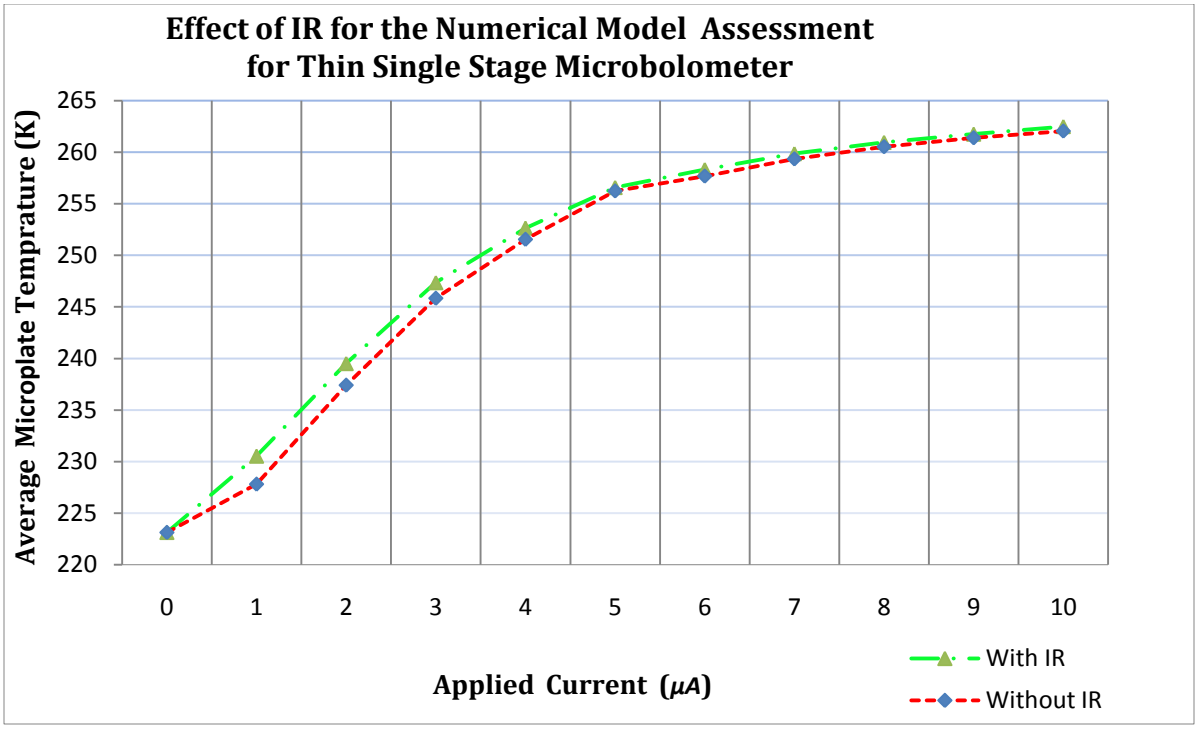

Figure 5.12: The electro-thermal model result with and without the effect of IR energy

The added temperature increase attributed to IR energy is very small compared to the joule heating energy and, therefore, can be dismissed as a reliability concern under normal operating conditions. As shown in the plot, the absorbed IR energy generates a small amount of thermal energy, which raises the microplate temperature with maximum 1.1 % increase at 1 μA current load for this particular device. However, the simulation is significant for computing the performance analysis, designing the device and for developing the CMOS circuit to measure the temperature change.

5.3.3 Comparison between the Analytical and Numerical Electro-Thermal Model

The analytical and numerical models have been compared under the same operating conditions without the effect of radiation heat transfer. In order to compare the two models only joule heat generated is considered. The heat-transfer effect of the microbolometer, for both analytical and numerical methods, was modeled by imposing similar thermal boundary conditions on the structure. Constant-temperature boundaries were applied to the interfaces between the anchors and the substrate. The heat-generation distribution was determined using the electrical current density distribution, which was accurately estimated by both modeling methods. Temperature dependent material properties were assumed to be constant and only the temperature dependence of electrical resistivity was taken into account for both models.

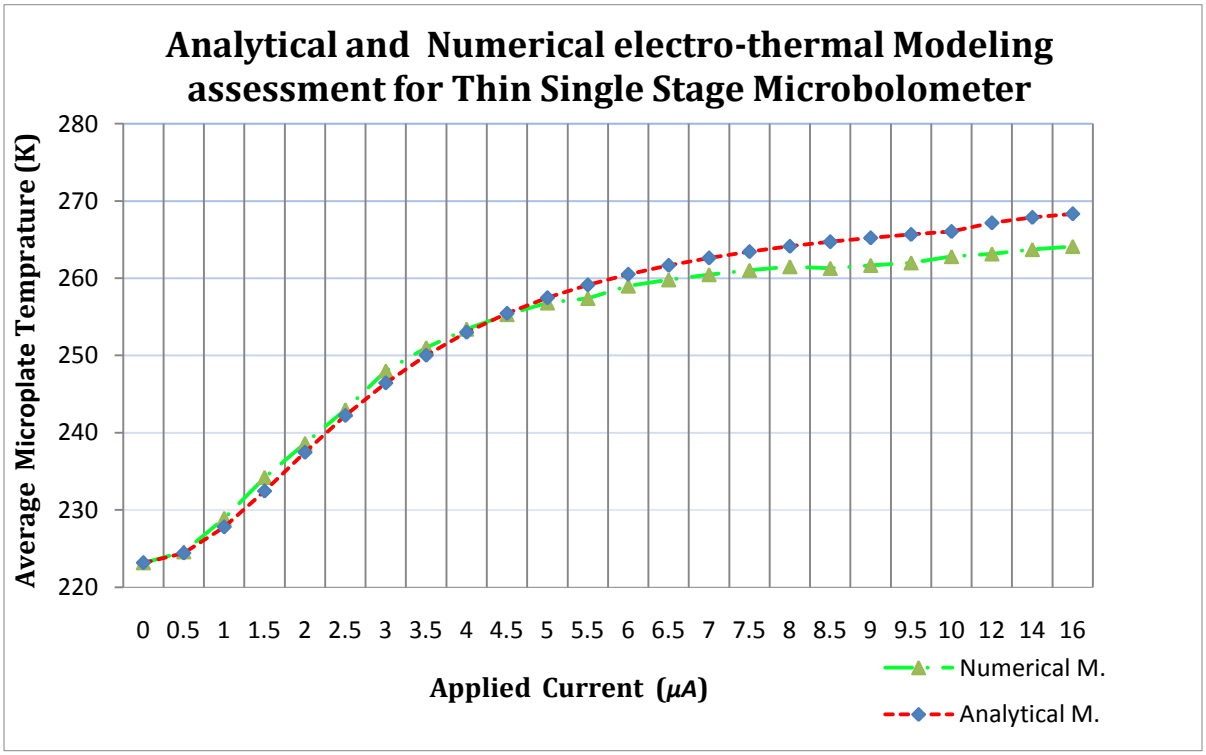

Figure 5.13: The electro-thermal model comparison under the same operating conditions for analytical and numerical models.

The average temperature as a function of the applied current is plotted in Figure 5.13 for the analytical and numerical models. The figure presents the comparison of the results by the FDM

solver and analytical model under the same condition. These results show that the two models are within very close agreement and have a maximum of difference 1.6 % when the applied current reaches at 16 μA. We noticed that, the numerical model generated very good approximations of the analytical solutions; however, the analytical simulation only takes a fraction of a second to compute while the numerical model takes up to 10 minutes to solve the same problem. This suggests that computation time can be reduced by several orders of magnitude by using the analytical model, if we are mainly interested to investigate the effect of joule heating.

5.4 Finite Element Simulation Results

The Thin Single Stage microbolometer and PolyMUMPs® test device were simulated using the commercial FEA software, ANSYS®, and plots were generated for the temperature distribution, stress distribution and total deflections. To compare the results with those of the analytical and numerical models, the simulations were performed for a range of constant DC bias currents (I) under the same operating conditions. In general, due to the geometrical symmetry and the assumption of isotropic material properties, the results obtained from the FEM simulations are symmetrical, similar to those obtained from the analytical and numerical models. However, it can easily be shown that small variations in the geometry of the structure, such as the ones that could be introduced during fabrication, for example, will render non-symmetrical results.

5.4.1 Temperature Distribution Plots

As previously discussed, one of the main objectives of the present research was to develop a model which can accurately predicts the temperature distribution of a microbolometer structure. Both the analytical and numerical modeling methods have demonstrated to be effective ways of predicting such a thermal distribution. In order to validate the analytical and numerical models using commercial FEA software, ANSYS® has been used. The temperature distribution plot of a Thin Single Stage microbolometer operating in a vacuum environment for a 5 µA load is provided in Figure 5.14. It can be observed from this plot that, as with the previous models, the temperature distribution is symmetrical. In addition, similar to the analytical and numerical

models, the maximum temperature occurs at the center of the microplate. The electrical contact areas have the minimum value, reflecting the constant temperature boundary condition to the heat sink assumed in the simulations.

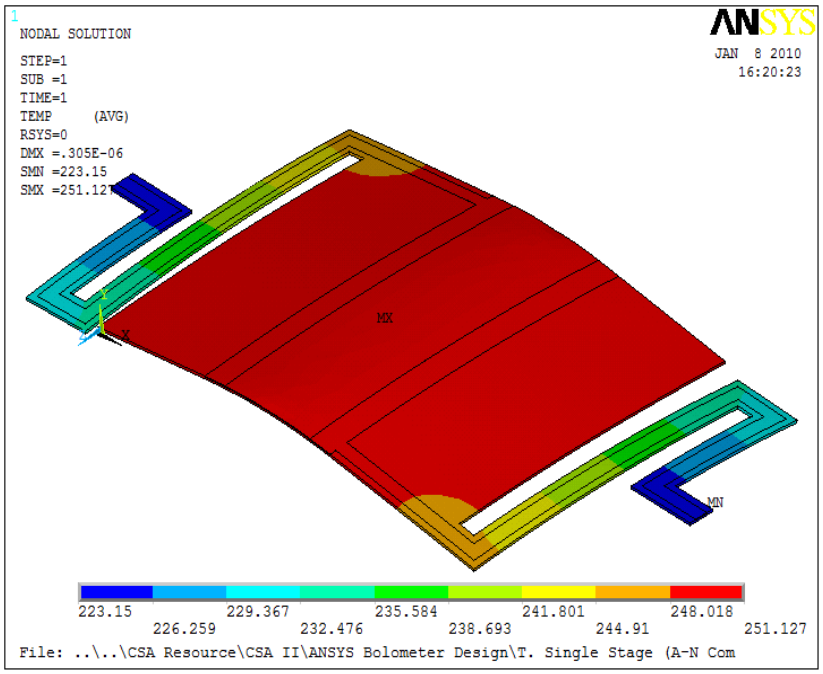

Figure 5.14: Temperature distribution (K) for the Thin Single Stage microbolometer for a DC bias current load of 5 μA in vacuum condition.

It should be noted that the overall temperature distribution for the Thin Single Stage microbolometer and the location of the maximum temperature values obtained using FEM simulations are comparable to those of the analytical and numerical models. For instance, the maximum temperature obtained using the analytical model in the case of the Thin Single Stage microbolometer operating in vacuum conditions with a 5 μA DC bias current was equal to 257.2 K, as presented in Figure 5.3. As indicated in Figure 5.14, a maximum temperature of 251.127 K was predicted under the same conditions using ANSYS®, which represents only a 2.3% difference. The maximum temperature plot for various load is presented for the analytical and numerical model and FEM simulation in Figure 5.15. As in the case for the previous models FEA simulation was done for various layer thickness and material properties. It should be noted that from the simulations performed it has been observed that variations in silicon nitride

thickness do not influence the value of the maximum temperature. However, the vanadium oxide and vanadium layer thickness influence the temperature distribution significantly.

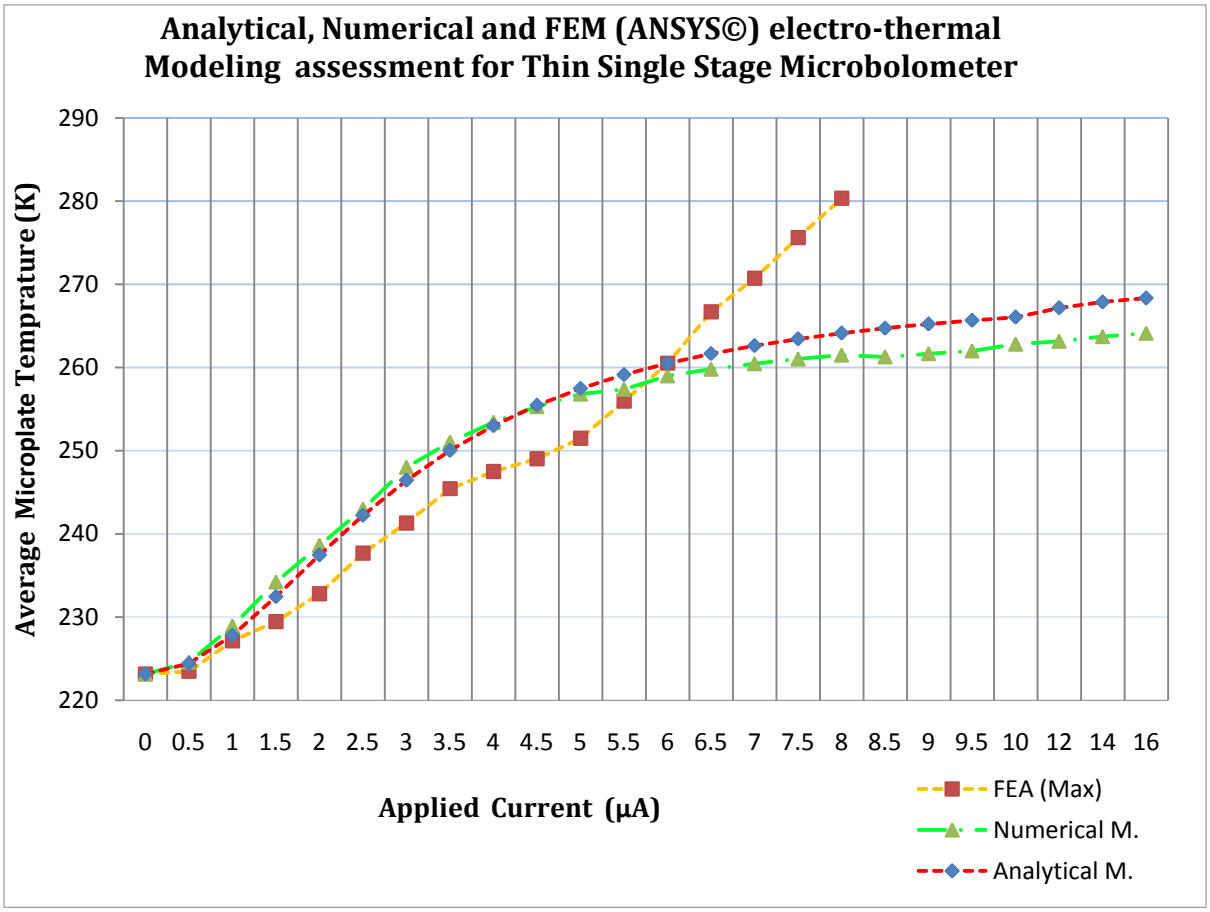

Figure 5.15: The electro-thermal model comparison under the same operating conditions for all analysis methods.

For the heat transfer analysis not only is the final (steady state) solution is usually of interest, but also the way the temperature field changes from the initial values as time proceeds is important, which is referred to as the transient solution. Therefore, the Thin Single Stage microbolometer has been simulated for transient analysis using ANSYS® software. For the transient analysis, it is assumed that all the Thin Single Stage microbolometer nodes have an initial temperature of 223.15 K at time t = 0, which is the boundary condition used in the previous models as well. When a 5 µA bias current is applied to the pixel, heat begins to generate and flow from the pixel nodes, where some of the heat is stored, to the substrate. Since the maximum temperature for the

vacuum condition is realized at the middle of the microplate, the center node from the pixel structure was selected to analyze the transient temperature change with time. The temperature change of the microplate center node over time is shown in Figure 5.16. As can be seen from the figure, the time taken to reach steady state for the temperature is about 0.45 ms.

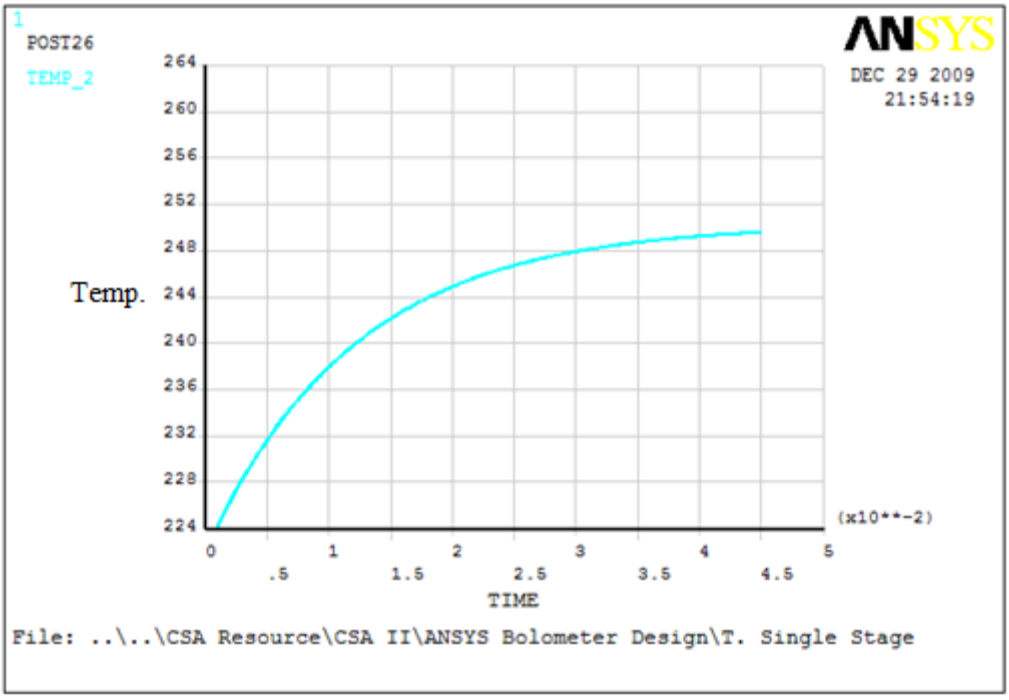

Figure 5.16: Transient thermal analysis plot for Thin Single Stage microbolometer

The temperature distribution for the PolyMUMPs® test device was also simulated for both air and vacuum conditions. It was important to develop a FEM simulation for the air condition because the actual test is conducted in an air environment. As with the Thin Single Stage microbolometer, the maximum temperature occurs at the center of the test device plate in the vacuum condition. However, the thermal distribution simulated for the test device when it operates in an air environment differs significantly from that Thin Single Stage microbolometer. This is attributed to differences in device geometry and material properties. The temperature distribution for the test device and the location of the maximum temperature values obtained through FEM simulations are also comparable to those of the analytical model result simulated for the PolyMUMPs® test device. The maximum temperature obtained using the analytical model for the case of the test device in vacuum conditions and 10 mA (0.8V) of DC bias current was

553.20 K, as shown in Figure 5.6. A maximum temperature of 534.51 K was predicted under the same conditions using ANSYS®, as shown in Figure 5.17, which represents a difference of only 3.4%.

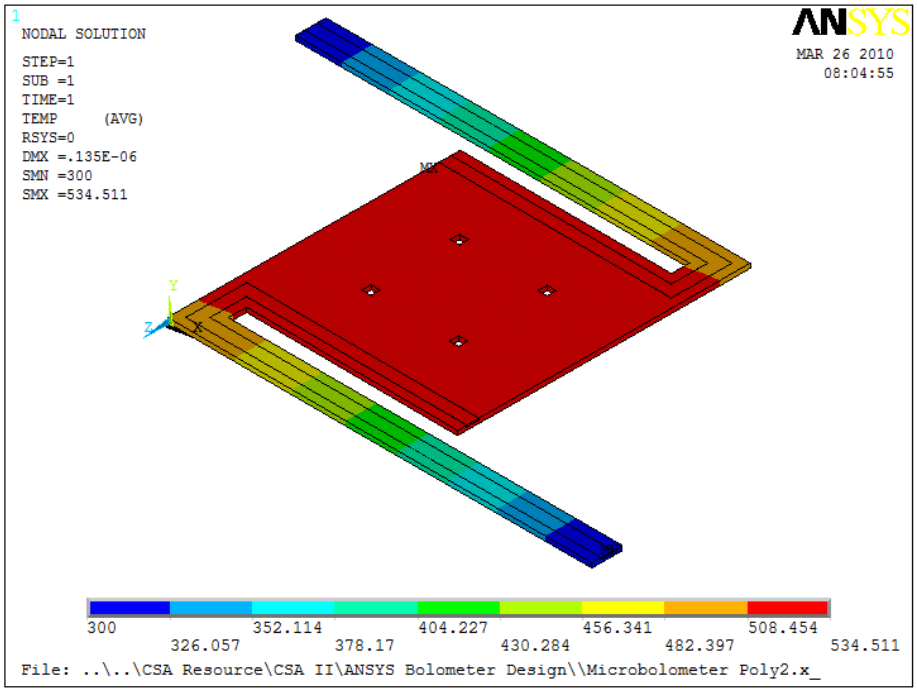

Figure 5.17: Temperature distribution (K) for PolyMUMPs® test device for a DC bias current load of 10 mA (0.8V) in vacuum condition.

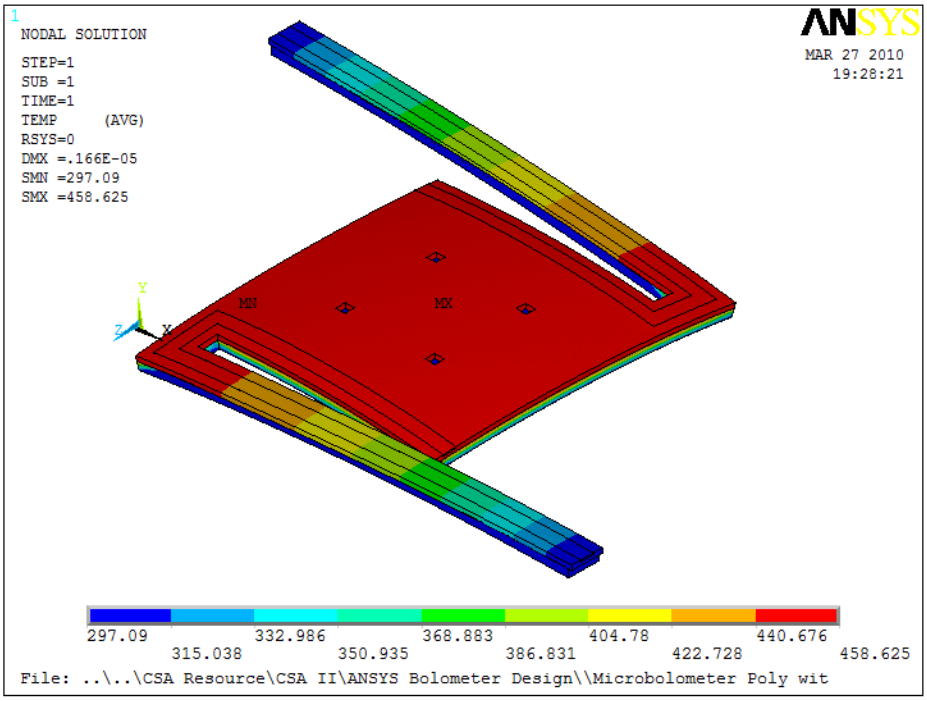

Figure 5.18: Temperature distribution (K) for PolyMUMPs® test device for a DC bias current load of 10 mA (0.8V) in air condition.

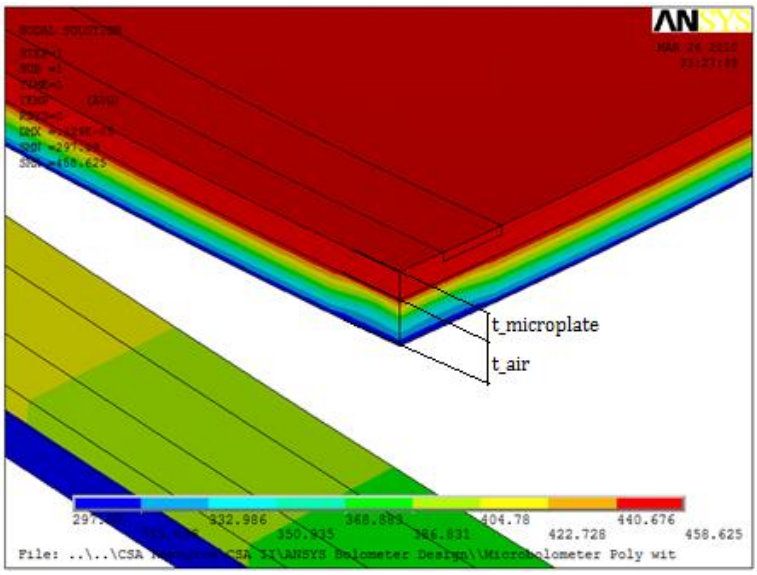

Figure 5.19: Temperature distribution of the air under the microplate (K) for PolyMUMP test device for a DC bias current load of 10 mA (0.8V) in air condition.

5.4.2 Total Deflection Distribution Plots

The coefficient of thermal expansion (CTE) mismatch between different materials induces thermal stress if the device temperature changes. The stress caused by the CTE mismatch, along with thermal gradient induced thermal strain, causes structure deflection. The distribution of the thermal structural deformations obtained from the FEM simulations for both the Thin Single Stage microbolometer and the PolyMUMPs® test device, when 5 µA of DC bias current is applied, is shown in Figure 5.20. It should be noted that the electrical contact area is the same color in the figure, indicating that contact areas are constrained in all directions. From this figure, it can be observed that the maximum deformation is equal to 305 nm and it is directed upward for a Thin Single Stage microbolometer. The maximum deflection occurs at the center of the microplate due to the fact that the CTE value of vanadium oxide is much higher than that of silicon nitride. In addition to the higher CTE value of Vanadium oxide , the maximum temperature in the middle of the microplate, causes the deflection to be higher in this region III of the microplate area.

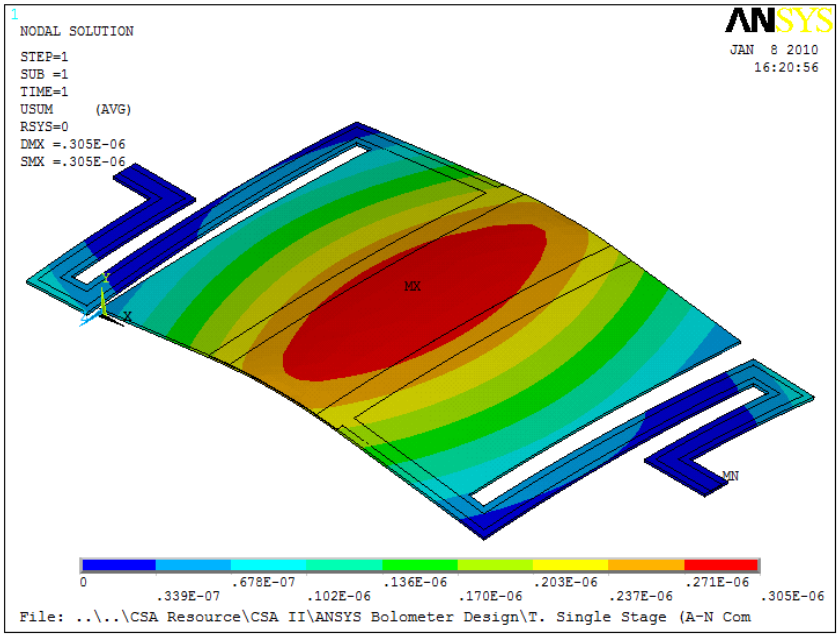

Figure 5.20: Thin Single Stage microbolometer deflection distribution plot in pm

The maximum thermal deformation for the test device was also observed for a range of DC voltage. As expected, the legs of the test device deflect down to the substrate due to the higher coefficient of thermal expansion of Gold. The simulation also predicts a curvature in the microplate due to the CTE mismatch between the gold and polysilicon used to fabricate the device. For 10 mA (0.8V), a maximum deflection occurs in the middle of the plate, as shown in Figure 5.21 and 2.22.

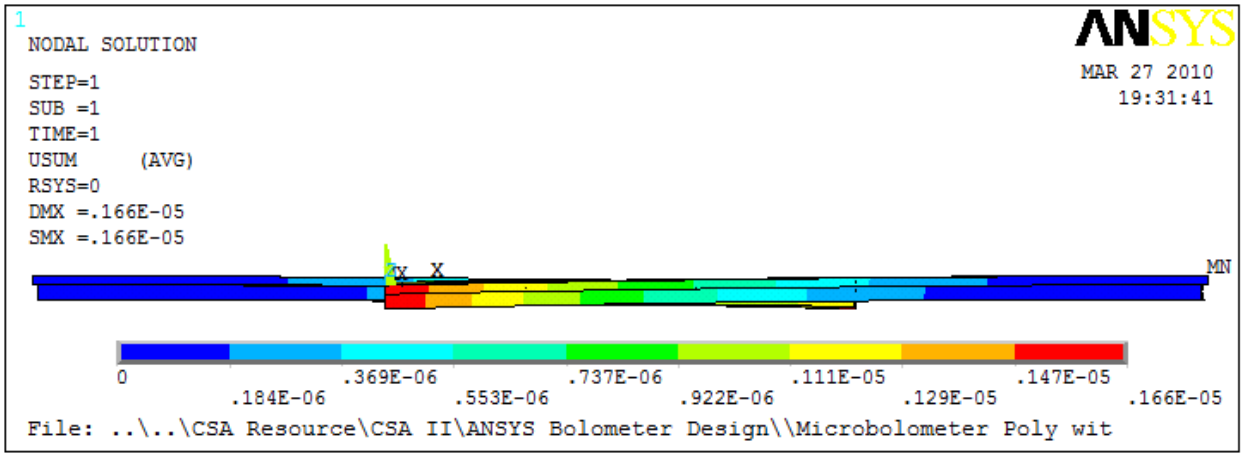

Figure 5.21: Side view deflection distribution plot for PolyMUMPs® test device for 10mA (0,58V)

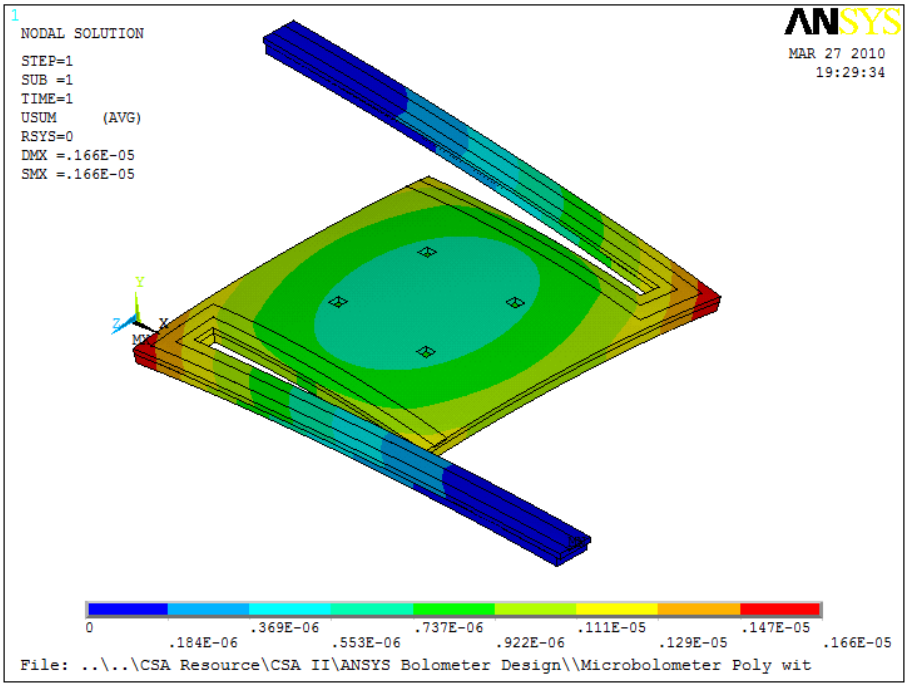

Figure 5.22: Deflection distribution plot effect for PolyMUMPs® test device for 10mA (0.8V)

5.4.3 Stress Distribution Plots

As one of the best criterions used for the analysis of ductile materials, the Von Misses stress method was used to evaluate the thermal stresses induced in the structure. The thermal stress distributions for a TSS microbolometer are shown in Figures 5.23.

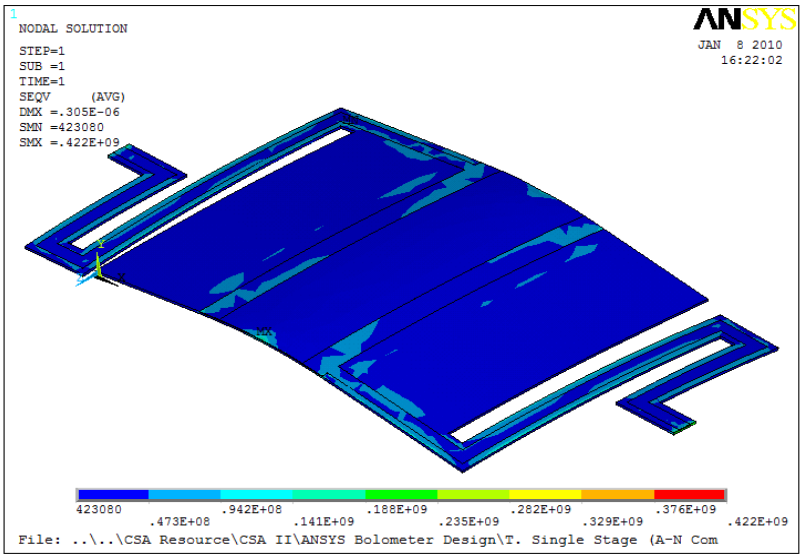

Figure 5.23: Stress distributions in MPa for a Thin Single Stage microbolometer for a 5 μA DC bias.

From the plot shown in Figure 5.23, the maximum value of the thermal stress occurs at the contact point between the vanadium and the vanadium oxide and is equal to 2142 MPa. It should be noted that this value is well below the yield strength of all materials used in the device. Peak thermal stress is 2050 MPa at re-entrant corners of aperture. This is less than the 234 GPa tensile strength for silicon nitride. Note that stress variation indicates some limited effect of mesh limitation.

5.5 Infrared Absorption Result for Thin Single Stage Microbolometer

5.6 Experimental Analysis and Results

In previous sections of this chapter both models and simulations results were discussed. In this section, the analytical and numerical models are validated using experimental results derived from the PolyMUMPs® test device. The test device size is too small to measure the temperature directly from the microplate. As a result, indirect measurement of the thermal distribution was

used to validate the analytical and numerical models. This method of indirect temperature measurement entailed measuring the deflection of the PolyMUMPs® test device when applied with a bias electric current. The deflection is then measured and related to the temperature of the device obtained from the FEM simulations under the same testing conditions.

In section 5.4.1, ANSYS® FEM simulation provided a reasonable thermal distribution agreement with both analytical and numerical models. In addition to the electro-thermal simulation, ANSYS® simulation has been used to estimate the deflection of the test device due to the joule heating effect. The joule heating effect creates an increase in thermal distribution across the device as presented in the earlier sections. The temperature increase causes deflection due to a thermal coefficient mismatch between the different layers used to fabricate the test device. In this section, the deflection simulated using ANSYS® software is compared with the experimental results. This approach uses the nodal temperatures from the electro-thermal FEM simulation as inputs for thermo-mechanical ANSYS® simulation to predict the steady-state microplate deflection and then compares this with the microplate deflection measured experimentally under the same testing conditions. This will relate the current applied to the change in temperature. Then, the results will be used to indirectly compare the analytical and numerical results with the experimental results. The thermo-mechanical model developed for test device legs in Chapter three is also compared with the experimental results.

Prior to the experiment, the actual size of the test device was measured. The designed dimensions and structure of the test device can be altered during the fabrication process for a variety of reasons. One of the main factors is that the fabrication tolerance of each process varies depending on the fabricating technique used. Therefore, it is important to measure the actual test device dimensions in order to provide accurate values in the different models developed. The following sub-section begins with the results of the optical profiler measurements of the actual thin-film and the air gap between the microplate and substrate.

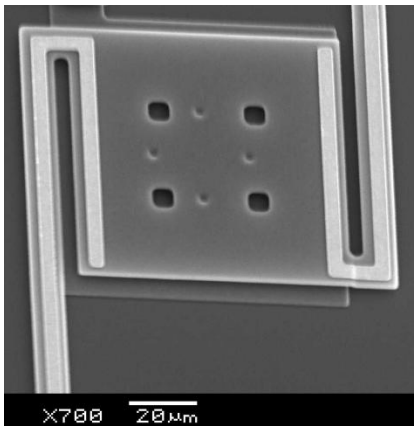

Figure 5.24: The SEM images of the test structures with 140 μm leg length

5.6.1 Experimental Setup

An Optical profiler was used to measure the actual fabricated dimension and deformation of the test device as a function of applied voltage. The optical profiler is a non-contact 3D measuring instrument used to measure dimensions spanning from sub-nanometer roughness to millimeter-high steps. The surface profiles of the test structures were captured by a WYKO NT100 Optical profiler, shown in Figure 5.25. WYKO surface profiler systems use two technologies to measure a wide range of surface heights, the Phase Shifting Interferometry (PSI) mode and Vertical Scanning Interferometry (VSI) mode. The PSI mode has a vertical resolution up to 0.3nm. Since the expected deflection, as obtained from FEM simulation, is very small, the PSI mode was used for the test. This technique for resolving surface heights is reliable when the fringe pattern is sufficiently sampled.

The test was done in ambient air environment using microprobes while viewing the PolyMUMPs® test device under an optical profiler. The test device is wire bonded for easy access to DC voltage and secured to a stable circuit board while the test was conducted. First, the optical profiler was used to measure the thickness and other dimensions of the test structure (Poly 0, Poly 2, and gold). The measured thickness and length values were used to simulate the analytical, numerical and FEM models, instead of the original design values.

Figure 5.25: WYKO NT100 optical profiler used to characterise the test device

5.6.2 Film Thickness and Deflection Measurements

Initial visual inspection from the profiler indicate that the test device has bent down at the middle of the microplate due to the CTE mismatch between the gold and Polysilicon during fabrication. This deflection was measured to be around 20nm and was located at the middle of the microplate. When a bias voltage was applied, the test device deflected further down to the substrate, as shown in Figure 5.26. From the figure, the deflection can be seen visually with the change in colour from orange (Figure 5.26 (a)) to cyan (Figure 5.26 (b)) across the deflected device. The deflection can also be observed in the leg structure tapering down as it approaches the microplate following a 10V application as seen in Figure 5.26 (b). This result is consistent with the FEM simulation as presented in the previous sections and shown in Figure 5.27. Since gold has a higher thermal expansion value than Polysilicon, it expands more than Polysilicon, leading to a downward deflection in the leg structure which causes the entire plate to move down as the temperature increases with the applied current. The magnitude of the deflection increased as the applied voltage increased from 0 to 12V.

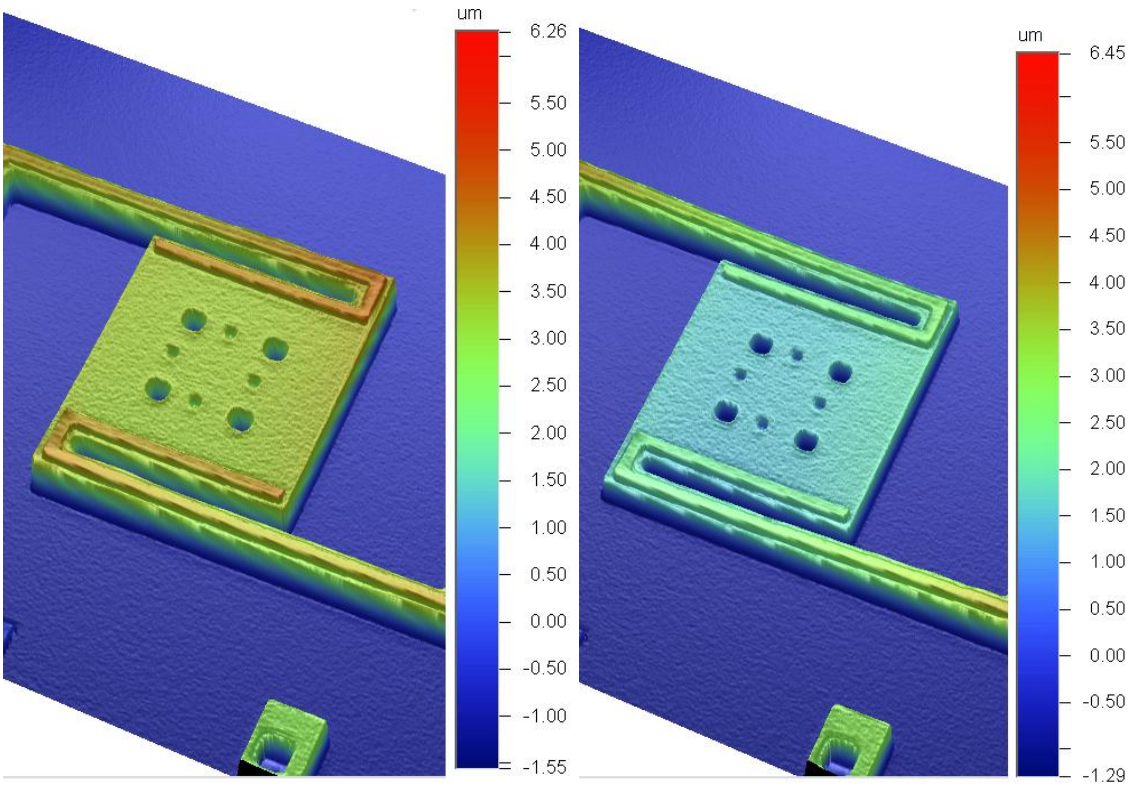

(a) (b)

Figure 5.26: PolyMUMPs® test device 3D image created by WYKO NT100 Optical Profiler (a) unactuated (at 0V) state (b) actuated (at 10 V) applied across the legs

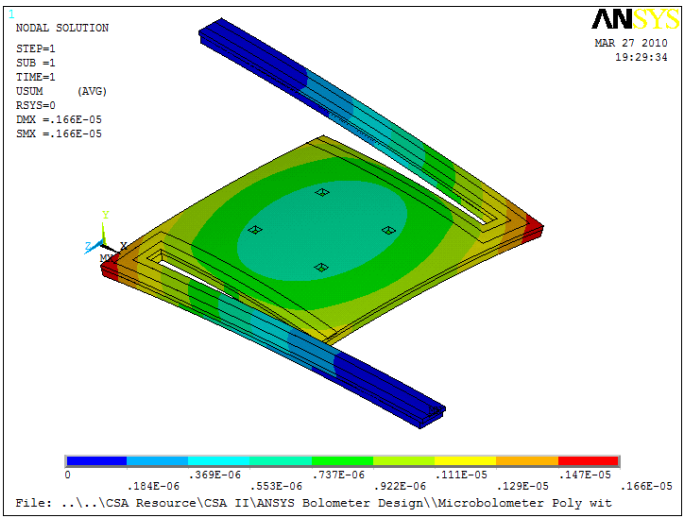

Figure 5.27: PolyMUMPs® test device deflection to the substrate due to higher gold CTE value

As the device deflect when applied with a bias voltage, the air gap between the substrate and the microplate decreases. In order to measure the deflection of the test device the air gap at each voltage load has been observed. The air gap between the microplate and substrate and the film thickness measurements were made by analyzing the *x* and *y* profile measurement of the unactuated state. The *x* and *y* directions profile of the unactuated (0 V) PolyMUMPs® test device can be seen in the 2D profile images in Figure 5.28 (b). The average vertical distance between the top of the microplate and the top of the silicon nitride layer was measured as 4.6 μm, as shown in Figure 5.28 (b) . This distance is equal to the summation of the layers thickness, which includes Poly0, Poly2 and the air gap.

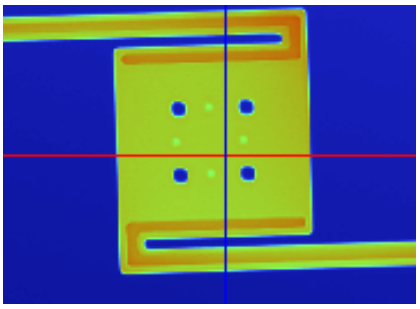

(a)

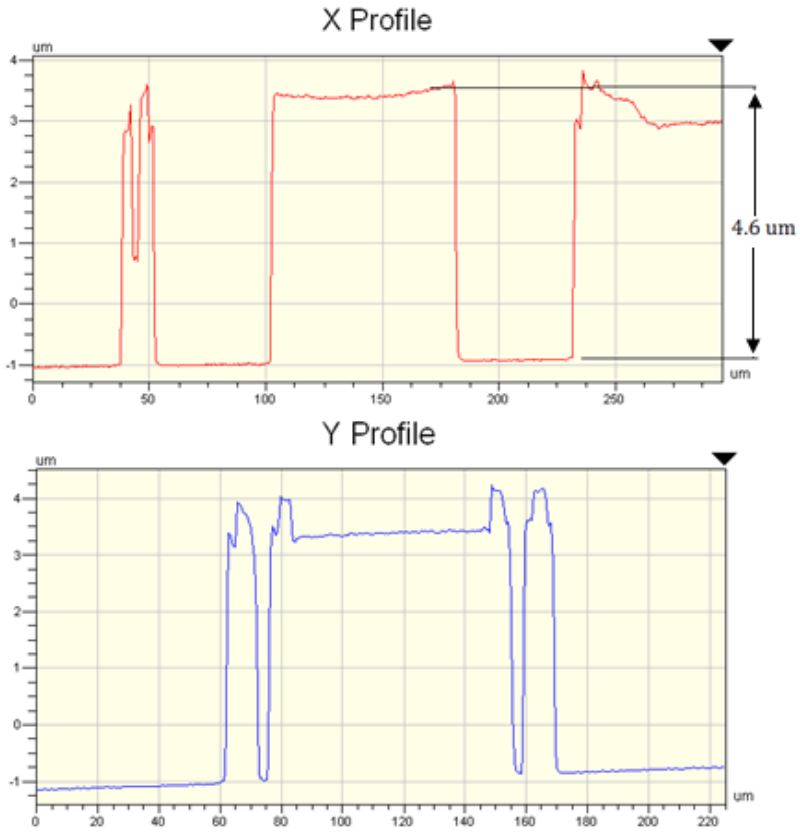

(b)

Figure 5.28: Profile of the test PolyMUMPs® test device in unactuated state: (a) shows the actual location in the microplate where the X and Y profile is measured and (b) measurement of the X and Y profile in the microplate

$$t_{total\_@0} = t_{Poly0} + g_{airgap\_@0V} + t_{Poly2} \quad (5.1)$$

= 4.6 μm (measured)

where $t_{total\_@0}$ is the total thickness at 0 voltage (unactuated condition)

t_{Poly0}, Poly 0 thickness (base plate),

$g_{airgap\_@0V}$ the air gap between the microplate and substrate at un-actuated condition

t_{Poly2} Poly 2 thickness (microplate)

The Poly 0 and Poly 2 thicknesses are measured as 0.6 μm and 1.3μm, which make the air gap (g_0) about 2.7 μm at unactuated condition. Following the structural examination at the unactuated state the device is applied with a range of DC voltages across the microplate. The deflection of the test device was investigated at two different locations. First the microplate deflection at the center, which happens to be the maximum, was observed. These deflections were compared with the ANSYS® simulated results. The leg deflection was also analyzed with the analytical and ANSYS® simulated results. In both locations, the deflection was similar to the one observed in FEM simulations as shown in Figure 5.27.

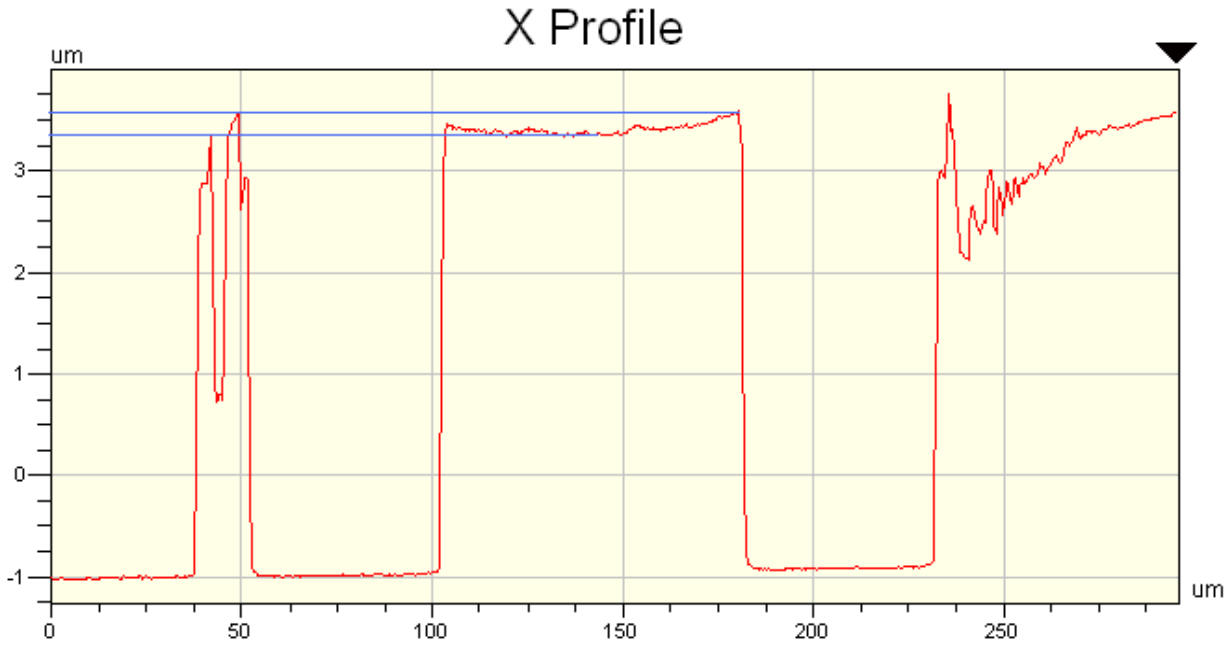

Figure 5.29: The PolyMUMPs® test device in the actuated state when 1 V applied

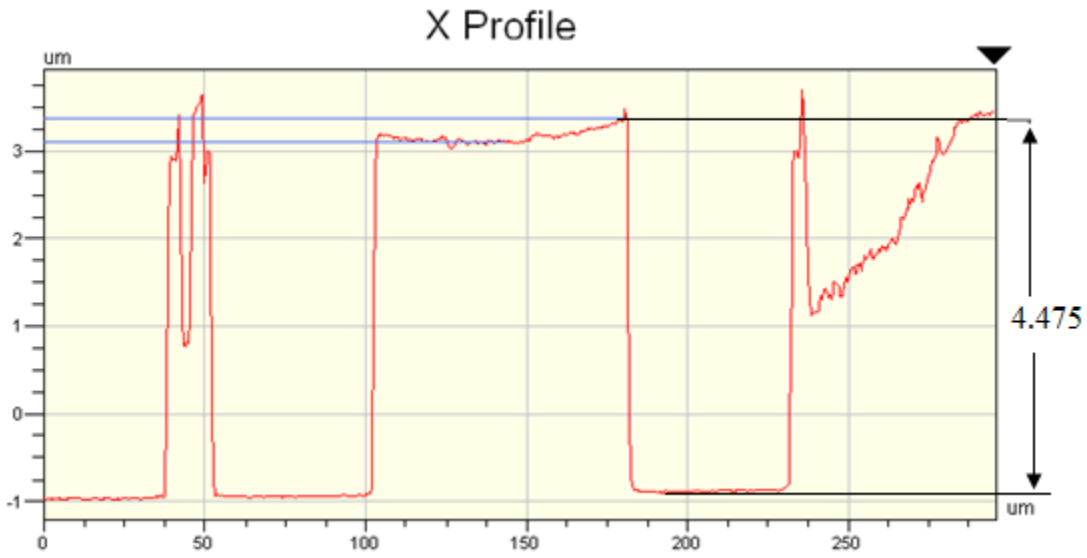

Figure 5.30: The PolyMUMPs® test device in the actuated state when 5V applied

In Figure 5.29 and 5.30 the *x* profile of the experimental results for the PolyMUMPs® test device is plotted when 1V and 5V are applied across the microplate. The gap difference between the microplate and the substrate was shorter than the previous unactuated measurement. For a 5V load the total height measured to be 4.475 μm and, similarly to Eq. (5.1), this height difference is equal to the summation of all the layers composing the test device structure:

$$t_{total\_@5V} = t_{Poly0} + g_{airgap\_@5V} + t_{Poly2} \qquad (5.2)$$

$$= 4.475\ \mu m \text{ (measured) at 5 V}$$

The overall height of the microplate decreased from its original unactuated height of 4.6μm to the new height 4.475 μm when the 5V current was applied. This indicates that the air gap decreased by 0.125 μm (125 nm), which further indicates that the microplate deflected this distance toward the substrate. The deflection is computed by

$$\text{Deflection} = ((g_0)_{\text{unactuated}} - (g_0)_{\text{at 5V}}) = (4.6\mu m - 4.475\ \mu m) = 125 \text{ nm}$$

As the actuation voltage is increased further, the air gap does decrease significantly (from 4.6μm in the unactuated state to 4.4 μm at 10 V). Figure 5.31 shows a comparative plot of the

deflections obtained from the experiment and FEA simulations at various current loads, ranging from 1 μA to 10 μA.

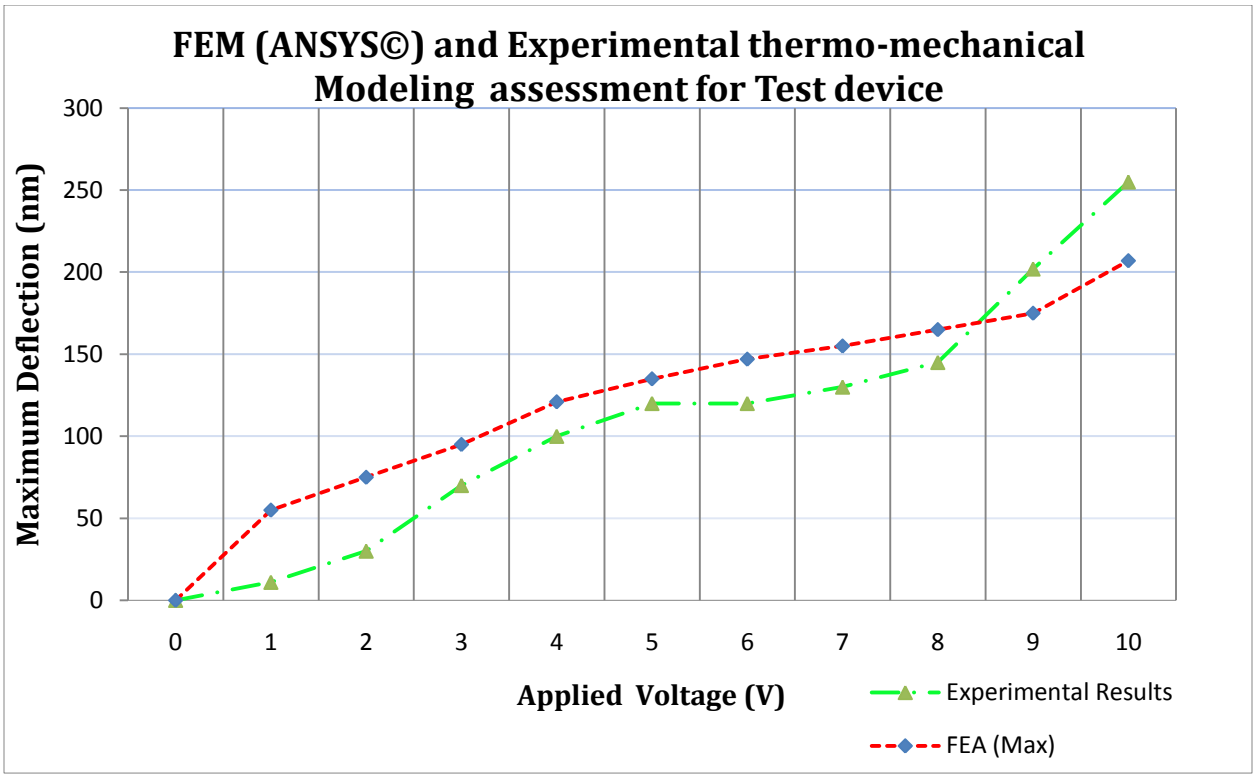

Figure 5.31: The maximum deflection result from the experiment and FEM simulation of the microplate.

As can be seen from the graph, deflection results for the PolyMUMPs® test device show a close agreement with the FEM simulation results up to 8 V but then start to diverge afterwards. The discrepancies may be induced by the contact resistance between the probe tip and the contact pads. This effect was not considered in any of the modeling results presented earlier. This result cannot be used to directly infer the temperature distribution which the electro-thermal analytical and numerical model predicts. Therefore, the temperature result obtained from the FEM simulation can be used to relate the experimental result with the modeling results discussed above.

5.6.3 PolyMUMPs® Test Device Leg Deflection

The thermo-mechanical model for the test device was difficult to develop analytical model due to the geometric features, non linear thermal distribution and material properties of the structures. Therefore, only the leg section was modeled with the analytical method for comparison to the experimental and FEM simulations. The arm profile in the unactuated state and in the actuated (contact) state is shown in Figure 5.32. Similar to the microplate part, the arm bent down at the middle, roughly 75 nm, at the unactuated condition. As the voltage across the microplate increases the leg starts to bend down where it makes contact with the microplate, as shown in Figure 5.32. The deflection of the leg tips, at the contact point with the microplate was recorded as voltage increased from the unactuated states.

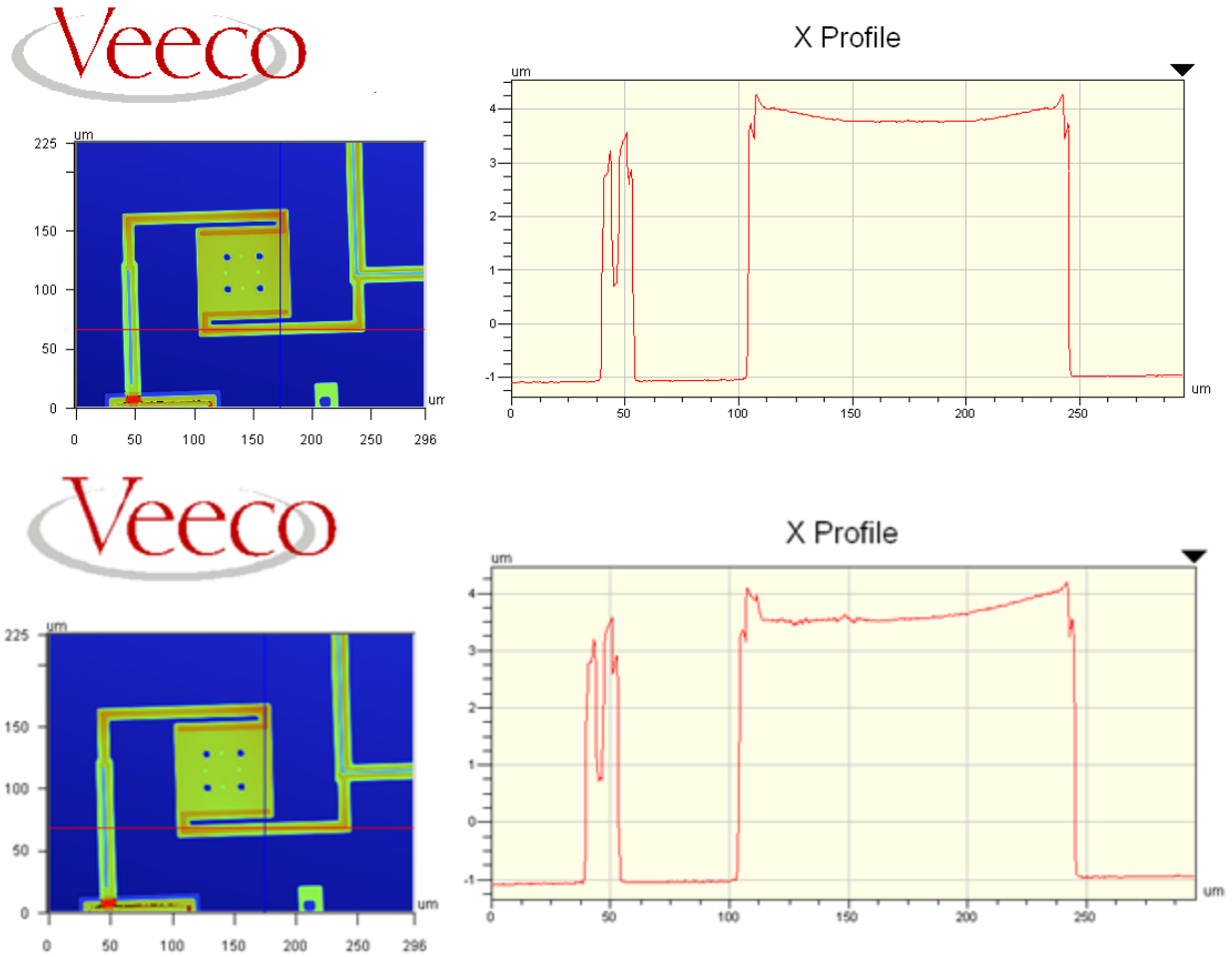

Figure 5.32: Test device leg profile (a) unactuated and (b) actuated with 1 V profile in the X direction

The analytical thermo-mechanical model computes the deflection of the leg with uniform temperature increase. However, as presented in the previous section, the electro-thermal simulation results produced a non-linear temperature gradient in the leg for the Thin Single Stage microbolometer and PolyMUMPs® test device. As presented in Figure 5.5 the temperature distribution varies from the anchors constant temperature of 300 K, set as a heat sink, to a maximum of 452 K at the contact point between the microplate and the leg when 0.8V was applied across the pad. Using the average values of this temperature the deflection for the leg has been computed using Eq. (3.88). For instance, the average temperature increase for 1V is computed to be 79.8 K and using the device geometry and material properties for the test device in Eq. (3.88) the tip of the leg deflects 18 nm. As can be seen in Figure 5.33, the assumption of an average constant temperature produces significant differences between the analytical deflection results and the FEM simulation and experimental results. The FEM simulation results have been found in very close agreement with the experimental results with maximum error difference of 21% at 4V.

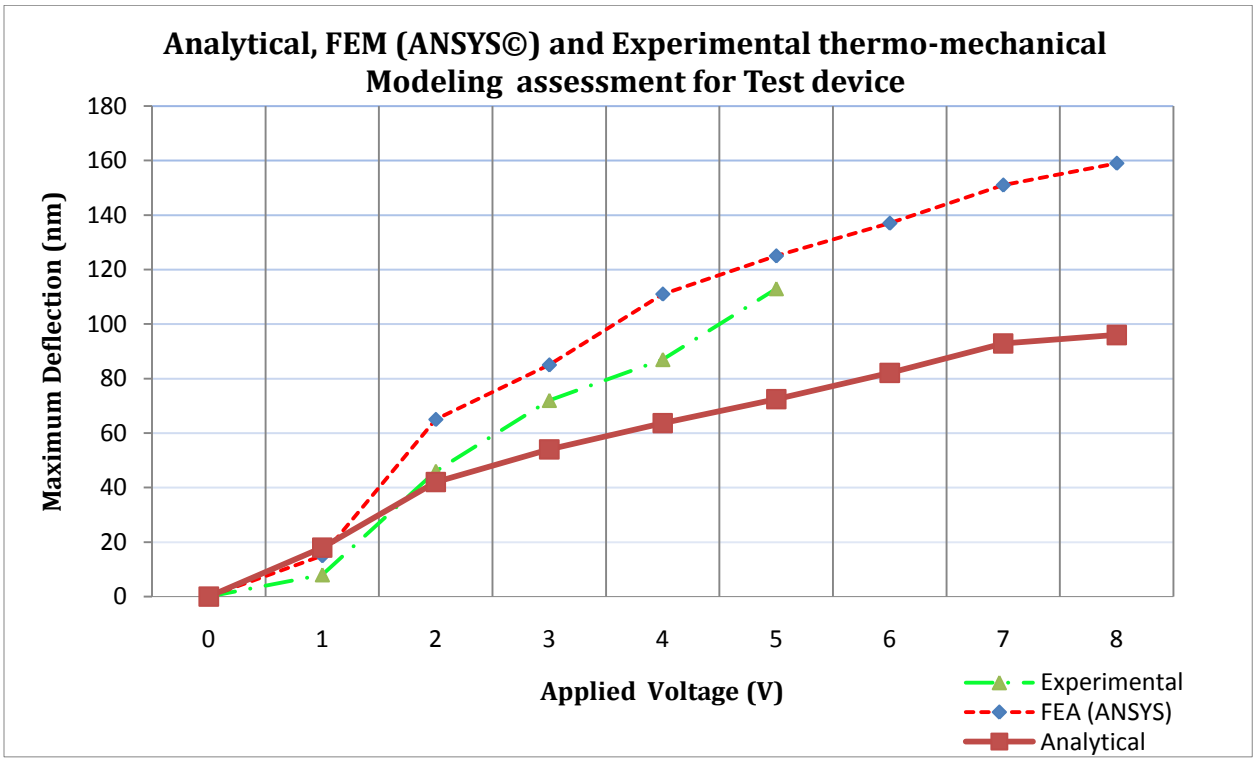

Figure 5.33: Test device leg tip deflection result for the experimental and simulations results.

5.6.4 Deflection versus Temperature

In order to relate the deflection results to the temperature distribution of the test device, deflection was recorded at different voltages (0V to 10V) in the experiment and FEM analysis. As presented in the previous sections, the experimental deflection at the middle of the microplate region is in close agreement with FEM simulation. Therefore, it is possible to relate the temperature of the pixel structure with the deflection results from the FEM simulation. This can be done after measuring the deflection of the test device; the temperature of the test device can be estimated using the FEA simulation results as shown in Figure 5.34. For instance when a 5V load is applied, the test device deflects about 127 nm and this deflection infers a temperature of 270 K as shown in the Figure 5.34. This plot is quite useful, as it allows for the approximation of average device temperatures from observed test deflections without running the simulation.

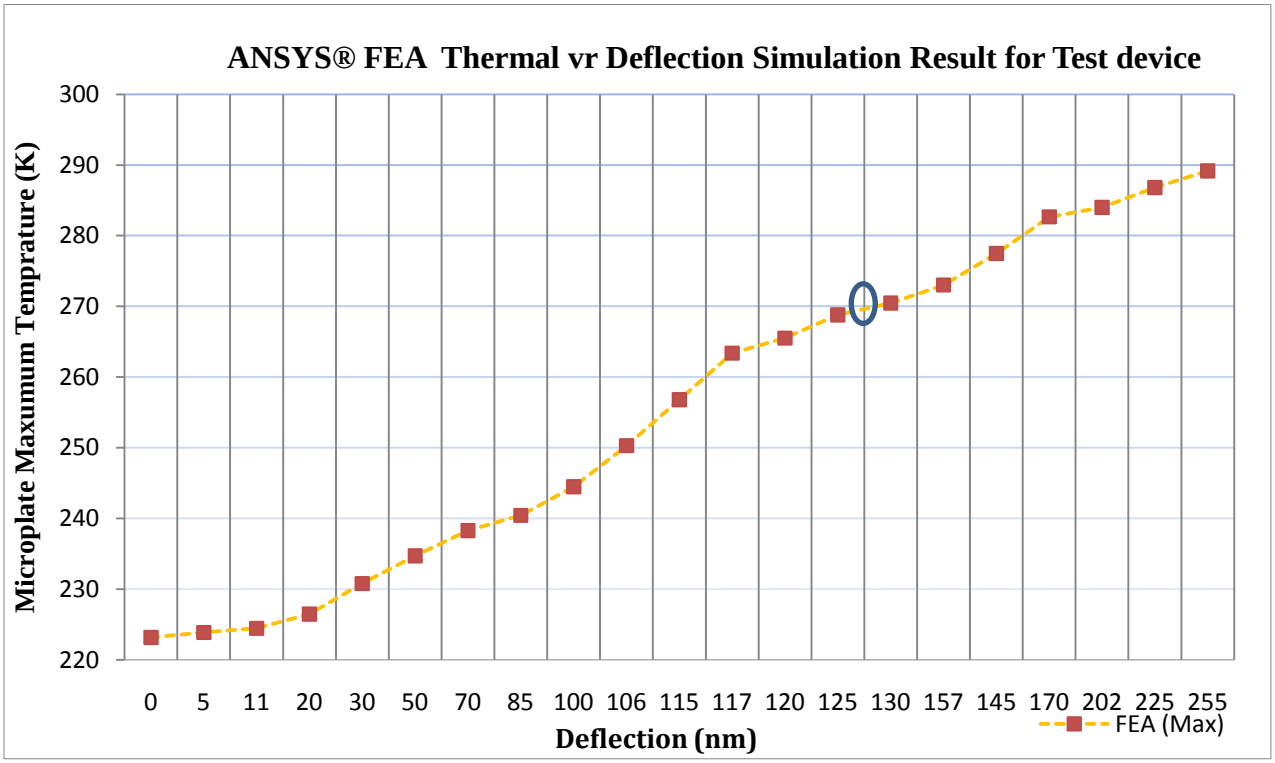

Figure 5.34: The ANSYS® electro-thermo mechanical simulation result for relating the deflection.

Chapter Six

Summary and Conclusions

In this thesis, both analytical and numerical modeling, as well as FEA simulation results were presented for the study of temperature distributions generated by joule heating and incoming IR energy in uncooled microbolometer pixels. The electro-thermal models were developed as a foundation for the analysis of the performance and reliability of uncooled microbolometer pixels in space applications. A one-dimensional steady-state electro-thermal analytical model for a Thin Single Stage uncooled microbolometer was developed. The analytical model relates the temperature distribution to applied DC current. The thin film geometrical features and other environmental conditions were taken into consideration. To include the effects of the radiation, the IR energy source, and the temperature dependent material properties in the electro-thermal model, a numerical method was also used. To assess the functionality of the models, two devices were considered, namely the Thin Single Stage microbolometer and the PolyMUMPs® test device.

Matlab® software was used to solve the coupled electro-thermal analytical and numerical equations in both vacuum and air ambient conditions. Nominal dimensions were used for the models and material property values were taken from CSA and literature sources. The Thin Single Stage microbolometer design was also simulated to compute the thermo-mechanical induced deflections, as well as stress and temperature distributions using ANSYS® Multiphysics.

The electro-thermal simulations results of the analytical and numerical models were compared; they match each other within 1.6 % of accuracy. For a range of applied currents, the numerical model can be used to predict two dimensional thermal distributions within a reasonable degree of accuracy compared to the most accurate analytical model. The best evidence that both models provide accurate methods of predicting device behaviour is their agreement with the FEM simulations. The analytical models simulation comparisons for both the Thin Single Stage and

PolyMUMPs® test device and the model shows 2.3 % difference from the FEM simulations for Thin Single Stage.

In order to verify the modeling results against experimental data, FEM simulations of deflection caused by joule heating across a PolyMUMPs® test device were developed. The comparison of the FEM simulations to the experimental data, for the microplate area, showed agreement with a maximum of 18.8 % at 10V when investigated from 0 V to 10 V. However, many assumptions had to be made to compare the analytical models for the test device leg deflection to the experimental results, hence more research must be conducted to verify the current findings.

From the analytical and numerical simulation results, it can be concluded that the maximum temperature achieved depends highly on specific properties of the fabrication materials, mainly resistivity and thermal conductivity. In addition, evaluations of the model have shown that the temperature changes as the device dimensions changes, which suggests further investigation is required to determine the exact relevance of these dimensional changes in the microbolometer performance. It was also demonstrated, using both analytical and numerical models, and FEM simulation, that the maximum temperature for a microbolometer operating under vacuum conditions happens at the center of the plate. However, the current load affects the position of the maximum temperature in the microbolometer pixel depending on whether it is operating in air or vacuum conditions and at high current loads, it shifts towards the legs. From the results obtained, we have demonstrated that the self-heating effect in the temperature distribution is far from negligible when trying to characterize a microbolometer pixel. We have also shown that the size of the electrode (vanadium) on the leg has a significant effect on the maximum temperature computed from the simulations.

The thermo-mechanical model demonstrated that the amount of deflection is a direct function of the applied DC bias current load. It was also proven that the displacement contour and out of plane plots exhibit the expected upward out-of-plane deflection corresponding to a higher coefficient of thermal expansion for the Vanadium oxide compared to silicon nitride. For the case of Thin Single Stage microbolometer, the maximum deformation occurs at the middle of the

bridge. In addition, simulated stresses are in the order of 2000 MPa, which is an order of magnitude below typical yield strengths of the materials used in the fabrication of the uncooled microbolometers studied here and are not of concern.

The analytical analysis was also performed using the PolyMUMPs© test device manufactured with Polysilicon, a material which has good mechanical properties and much lower resistivity compared to Vanadium oxide. Due to the lower resistivity values and large cross sectional area of the test device, the joule heating effect was significantly reduced for the same electric current. After comparing the experimental results to the simulations presented in this thesis, one of the major conclusions is that joule heating cannot cause failure of a Thin Single Stage microbolometer applied with a 10 μA current load because predicted temperatures only reach 256 K at this load. The simulation also demonstrates that small changes in dimension or material properties significantly change the temperature distributions significantly. For example when the vanadium electrode thickness across the leg changed from 100 nm to 75 nm, the temperature of the device simulated to be 512 K for vacuum environment.

The primary importance of the developed models is their application to design optimization and reliability analysis, particularly with respect to thermally induced deflection and stress. The equations that describe the general behaviour of the device can be used to determine parameters to maximize desirable device performance. However, uncooled microbolometers may fail due to other operational, environmental and/or degradation mechanisms. In addition to the joule heating effect, which was studied here, other possible failure mechanisms need to be investigated. A greater understanding of thermal cycling, for example, will be very important to future microbolometer reliability research as it can be caused by both thermal transient and electrical loads.

6.1 Recommendations and Future Work

The analytical and numerical models provide a basic understanding of the thermal distribution in a Thin Single Stage microbolometer pixel as a function of the device geometry and material properties at a given operating condition. Temperature dependent material properties are not available at this time. Since the knowledge of these properties is crucial for the accuracy of the

models, future work should include the determination of temperature dependent material properties of the structural layers used in the fabrication of the microbolometer. As discussed in Chapter three, in addition to the joule heating effect, the application of current in a multilayered MEMS structure will have further electro-thermal effects. Some of these effects are the Seebeck effect, the Peltier effect, and the Thomson effect. These phenomena have not been included in the present study due to the material properties limitation related to these effects.

Accurate material properties are critical in achieving an accurate model solution. A better understanding of the various material properties affecting model accuracy is therefore important. This is also important because material properties of a MEMS structure can vary depending on the fabrication process used for the specific device setup. Although current values documented in the literature provide good insight into material properties they cannot reflect the actual material properties of a given MEMS device. Therefore, future work must include more actual and accurate material properties characterization, particularly with respect to resistivity and thermal conductivity. Future studies would also benefit from further investigations on the accuracy of fabricated device dimensions.

Finally, and most importantly, future work must be undertaken to improve methods for experimental verification of analytical and numerical models. The indirect method used to verify the models is not the best approach to determine the temperature of the microstructures. There is an effective method of measuring the temperature directly from the test device using InfraScope II. During this study we were not able to gain access to this testing device; however, future studies should utilize such direct temperature measurement instruments. The experimental results could also be improved by eliminating possible heat transfer mechanisms that could potentially affect the overall results, such as convection and air conduction to the substrate. The effect of convection on the device behaviour is not well understood at this point. In our simulation the convection film coefficient was taken from the literature, as presented in Chapter three. Convection and air conduction from the microplate to the substrate effects can be eliminated during experimentation by characterizing the device in a vacuum environment.

References

[1] D. Effa, M. Shavezipur, P. Nieva "Modeling for Lifetime Prediction of Microbolometer Sensors" Technical Report, Vol 1, March 31, 2009.

[2] N. Topaloglu, P. Nieva, M. Yavuz, J. Huissoon "A Novel Method for Estimating the Thermal Conductance of Uncooled Microbolometer Pixels" Proceedings of the ISIE 2007 - IEEE International Symposium on Industrial Electronics, Vigo, Spain, pp 1554 – 1558, 2007.

[3] J. Carter, A. Cowen, B. Hardy, R. Mahadevan, M. Stoneeld, and S. Wilcenski "POLYMUMPs Design Handbook" Revision v11.0, 2005.

[4] C.D. Lott, T.W. McLain, J.N. Harb, and L.L. Howell "Modeling the Thermal Behaviour of a Surface-Micromachined Linear-Displacement Thermo-Mechanical Microactuator" Journal of Sensors and Actuators A 101, pp 239-250, 2002.

[5] D. Yan, A. Khajepour, and R. Mansour "Design and Modeling of a MEMS Bidirectional Vertical Thermal Actuator" Journal of Micromechanics and MicroEngineering 14, pp 841-850, 2004.

[6] L. Lin and M. Chiao "Electrothermal Response of Lineshape Microstructures" Journal of Sensors Actuators A 55, pp 35–41, 1996.

[7] L. Liew, A. Tuantranont, and V. M. Bright "Modeling of Thermal Actuation in a Bulk-Micromachined CMOS Micromirror" Microelectronics Journal 31, pp 791-801, 2000.

[8] Q. Huang and N. Lee "Analysis and Design of Polysilicon Thermal Flexture Actuator" Journal of MicroEngineering. 9, pp 64-70. London, UK, 1999.

[9] G. Lammel, S. Schweizer, and P. Renaud "Optical Microscanners and Microspectrometers Using Thermal Bimorph Actuators" Kluwer Academic, Boston, 2002.

[10] M. Baker, R. Plass, T. Headley, and J. Walraven "Compliant Thermo-Mechanical MEMS Actuator" Final Report, LDRD #52553, SAND Report SAND2004-6633. Sandia National Laboratories.

[11] G. Li, N. Yuan, J. Li, and X. Chenc "Thermal Simulation of Micromachined Bridge and Self-heating" Journal of Sensors and Actuators A 126, pp 430–435, 2006.

[12] A. Villarceau "Recherches sur le Mouvement et la Compensation des Chronometers" Annales de l'Observatoire Imperial de Paris, 1863.

[13] S. Grannan, P. L. Richards, and M. K. Hase "Numerical Optimization of Bolometric Infrared Detectors Including Optical Loading, Amplifier Noise, and Electrical Nonlinearities" International Journal of Infrared and Millimeter Waves, Vol. 18, No. 2, 1997.

[14] J. Puigcorbe, A. Vila, J. Cerda, A. Cirera, I. Gracia, C. Cane, and J.R. Morante "Thermo-Mechanical Analysis of Micro-drop Coated Gas Sensors" Sensors and Actuators A 97-98, pp 379-385, 2002.

[15] J. Bühler, J. Funk, O. Paul, F.-P. Steiner, and H. Baltes "Thermally Actuated CMOS Micromirrors" Journal of Sensors and Actuators A 46-47, pp 572-573, 1995.

[16] P. Neuzil and T. Mei "A Method of Suppressing Self-Heating Signal of Bolometers" IEEE Sensors Journal, Vol. 4, No. 2, 2004.

[17] J. Romagnan, J. Noiray, and J. Laheurte "The Effect of Self-Heating on the Measurement of a Temperature Change Using a Bolometric Detector" Journal of Low Temperature Physics, Vol. 115, Nos 5/6, 1999.

[18] A. Çengel "Heat Transfer a Practical Approach" McGraw-Hill Boston, Massachusetts, 1998.

[19] W. Rohsenow, J. Hartnett, and Y. Cho "Handbook of Heat Transfer" McGraw-Hill, New York, 1998.

[20] S. Grannan, P. Richards, and M. Hase "Numerical Optimization of Bolometric Detectors Including Optical Loading, Amplifier Noise, and Electrical Nonlinearities" International Journal of Infrared and Millimeter Waves, Vol. 18, No. 2, 1997.

[21] M. Liger "Uncooled Carbon Microbolometer Imager" Ph.D. Thesis, California Institute of Technology, Pasadena, California

[22] H. Shea "Reliability of MEMS for Space Applications" Proceedings of the ISIE Vol. 6111, pp 61110A, San Jose, CA, 2006.

[23] B. Stark "MEMS Reliability Assurance Guidelines for Space Applications" Jet Propulsion Laboratory, Pasadena, California, JPL Publication 99-1, 1999.

[24] S. Paradis, P. Laou, and D. Alain "Doped vanadium dioxide with enhanced infrared modulation" Defence R&D Canada – Valcartier, Technical Memorandum, DRDC Valcartier TM 2007-002, September 2007.

[25] W. Song and J. Talghader "Design and characterization of adaptive microbolometers" Journal of Micromechanics and Microengineering 16, pp 1073–1079, 2006.

[26] X. Gu, G. Karunasiri, J. Yu, G. Chen, U. Sridhar, and W.J. Zeng "On-chip compensation of self-heating effects in microbolometer infrared detector arrays" Journal of Sensors and Actuators A 69, pp 92-96, 1998.

[27] H. Guckel, J.Klein, T. Christenson, K. Skrobis, M. Laudon, and E.G. Lovell "Thermo-Magnetic Metal Flexture Actuators" Proceeding of the Fifth IEEE solid-state Sensor and Actuator Workshop, Technical Digest, 22-25, pp 73-75, 1992.

[28] J. Comtois, V. Bright, and M. Phipps "Thermal Microactuators for Surface-Micromachining Processes" Proceedings of the ISIE 2642, pp 10-21, 1995.

[29] N. Mankame and G. Ananthasuresh "Comprehensive Thermal Modeling and Characterization of an Electro-thermal-compliant Microactuator" Journal of Micromech. and Microeng. 11, pp 452-462, 2001.

[30] L. Que, J. Park, and Y. Gianchiandani "Bent-Beam Electrothermal Actuators: Part I. Single beam and cascaded devices" Journal of Microelectromech system. 63 (5), pp 247-254, 2001.

[31] J. Park, L. Chu, A. Oliver, and Y. Gianchiandani "Bent-Beam Electrothermal Actuators: Part II Linear and Rotary microengines" Journal of Microelectromech. System 63 (5), pp 255-262, 2001.

[32] T. Moulton and G. Ananthasuresh "Micromechanical Devices with Embedded Electro-Thermal Compliant Actuation" Journal of Sensors and Actuators A 90, pp 38-48, 2001.

[33] A. Yaradanakul and P. Butler, Zeynep Çelik-Butler "Uncooled Infrared Microbolometers on a Flexible Substrate" IEEE Transactions on Electron Devices, Vol. 49, No. 5, 2002.

[34] K. Wachutku "Rigorous Thermodynamic Treatment of Heat Generation and Conduction in Semiconductor Device Modeling" IEEE Transactions on Computer-Aided Design, Vol. 9, No. II , 1990.

[35] A. Mahmood, P. Butler, and Zeynep C "Micromachined Bolometers on Polyimide" Journal of Sensors and Actuators A 132, pp 452–459, 2006.

[36] L. Kuzmin, D. Chouvaev, M. Tarasov, P. Sundquist, M. Willander, and T. Claeson "On the Concept of a Normal Metal Hot-Electron Microbolometer for Space Applications" IEEE Transactions on Applied Superconductivity, Vol. 9, No. 2, 1999.

[37] S. Schweizer, S. Calmes, M. Laudon, and P. Renaud "Thermally Actuated Optical Microscanner with Large Angle and Low Consumption" Sensors and Actuators A 76, pp 470-477, 1999.

[38] R. Manginell, J. Smith, A. Ricco, R. Hughes, D. Moreno, and R. Huber "Electro-thermal Modeling of a Microbridge Gas Sensor" SPIE Symposium on Micromachining and Microfabrication, pp 360-371, Austin, TX, 1997.

[39] R. Manginell "A Polysilicon Microbridge Gas Sensor" Ph.D. Thesis, University of New Mexico, 1997.

[40] W. Peng, Z. Xiao, and K. R. Farmer "Optimization of Thermally Actuated Bimorph Cantilevers for Maximum Deflection" Nanotech 1, pp 376-379, 2003.

[41] G. Lammel, S. Schweizer, and P. Renaud "Optical Microscanners and Microspectrometers Using Thermal Bimorph Actuators" Kluwer Academic, Boston, 2002.

[42] S. Sedky, P. Fiorini, M. Caymax, C. Baert, L. Hermans, and R. Mertens "Characterization of Bolometers Based on Polycrystalline Silicon Germanium Alloys" IEEE Electron Device Letters, Vol. 19, NO. 10, 1998.

[43] J. Allen "Micro Electro Mechanical System Design" CRC Press, Taylor and Francis Group, Boca Raton Fl, 2005.

[44] H. Shea "Reliability of MEMS for Space Applications" Proceedings of SPIE Vol. 6111, pp 61110A, San Jose, CA, 2006.

[45] B. Stark "MEMS Reliability Assurance Guidelines for Space Applications" Jet Propulsion Laboratory, Pasadena, California, JPL Publication 99-1, 1999.

[46] H. Shea "Effects of Electrical Leakage Currents on MEMS Reliability and Performance" IEEE Transactions on Device and Materials Reliability 4(2), pp 198, 2004.

[47] J. Korvink, E. Rudnyi, and A. Greiner, Z. Liu "MEMS and NEMS Simulation: A Practical Guide to Design, Analysis, and Applications" Noyes Publications, 2005.

[48] Y. Ju and K. Goodson "Microscale Heat Conduction in Integrated Circuits and Their Constituent Films" Kluwer Academic Publishers, 1999.

[49] N. Mankame and G. Ananthasuresh "Comprehensive Thermal Modeling and Characterization of an Electro-Thermal-Compliant Microactuator" Journal of MicroEngineering 11, pp 452-462, 2001.

[50] H. Guckel and J.Klein, T. Christenson, K. Skrobis, M. Laudon, E.G. Lovell "Thermo-Magnetic Metal Flexture Actuators" Proceeding of the Fifth IEEE solid-state Sensor and Actuator Workshop, Technical Digest, 22-25, pp 73-73, 1992.

[51] L. Que, J.-S. Park, and Y.B. Gianchiandani "Bent-Beam Electro-thermal Actuators" Part I. Single Beam and Cascaded Devices, Journal of Microelectromech. Syst. 63 (5), pp 247-254, 2001.

Appendices

Appendix A – Electro-thermal Matlab® Code

Due to the confidentially of the electro-thermal Matlab® Code it's not presented in this section. However interested party can reach Prof. Patricia Nieva (pnieva@uwaterloo.ca) at the University of Waterloo for more information.

Appendix B – Infrared absorption model matlab code

```
clear all;

% Define constants:
j = sqrt(-1);
c = 299792458;                                  % speed of light
permittivity_o = 8.8541878176e-12;              % permittivity of free space
permeability _o = 4*pi*1e-7;                    % permeability of free space
eta0 = 1/sqrt(permeability _0/permittivity _0);     % Characteristic impedance of free space

% The thickness vector t.
 % t is the thickness vector for Region II and IV and t2 is the thickness vector for regions III
% the vector element for t2  (silicon nitride, vanadium oxide, silicon nitride, aluminum, silicon)
% the vector element for t  (silicon nitride, silicon nitride, silicon nitride, aluminum, silicon)

   t = [200e-9;100e-9;300e-9;2.5e-8;100e-9;50e-6];
   t2 = [200e-9;100e-9;300e-9;2.5e-8;100e-9;50e-6];

% The resistivity vector:
% The vector element contents the same layer as indicated for the thickness vector

    %ohm = [30e-6;1/0;15e-6;1e13;0.01];
    ohm  = [1e13;3e-2;1e13;1/0;2.6e-6;1e-3];
    ohm 2 = [1e13;1e13;1e13;1/0;2.6e-6;1e-3];
% Note: the resistivity of the cavity is taken as infinite.

% The relative permittivity vector:
   %permittivity _r = [11.2;1;11.2;4;11.2];
   %permittivity _r = [11.2;4;11.2;1;2;11.68];
   permittivity _r = [11.2;4;11.2;1;2;11.68];
   permittivity _r2 = [11.2;11.2;11.2;1;2;11.68];

% Z vector, of the distance from the top surface as given in the model calculated from t vector:
```

```
    %Z = [t(1);t(1)+t(2);t(1)+t(2)+t(3);t(1)+t(2)+t(3)+t(4); ...
    %t(1)+t(2)+t(3)+t(4)+t(5)];

    Z = [t(1);t(1)+t(2);t(1)+t(2)+t(3);t(1)+t(2)+t(3)+t(4); ...
    t(1)+t(2)+t(3)+t(4)+t(5);t(1)+t(2)+t(3)+t(4)+t(5)+t(6)];
    Z2 = [t(1);t(1)+t(2);t(1)+t(2)+t(3);t(1)+t(2)+t(3)+t(4); ...
    t(1)+t(2)+t(3)+t(4)+t(5);t(1)+t(2)+t(3)+t(4)+t(5)+t(6)];

% The wavelength range of interest:
        h = 4:0.01:14;

    for C  = 1:span(h)
        w = 2*pi*c/( h (C )*1e-6);              % the angular frequency of the signal

    for i = 1:span(permittivity _r)

permittivity (i) = permittivity _0*(permittivity _r(i)-j/(w*ohm (i)*permittivity _0));

% The characteristic impedance (eta) of each medium is calculated:
        eta(i) = 1/sqrt(permeability _0/permittivity (i));
            % The propagation constant (k) of each medium is calculated:
        k(i) = w*sqrt(permeability _0*permittivity (i));

    end

        r = zeros(span(permittivity _r),1); % Reflection coeff. vector initialized
        t = zeros(span(permittivity _r),1); % Transmission coeff. vector initialized

% The last boundary condition (at the mirror surface):
        r(span(permittivity _r)) = 0.1; % Taken arbitrarily, doesn't affect the result.
        t(span(permittivity _r)) = -r(span(permittivity _r))*exp(2*j*k(span(permittivity _r))* ...
        Z(span(permittivity _r)));
```

```
% By using a backwards iteration, t and r vectors are found:
    for i = span(permittivity _r)-1:-1:1
      t(i)=(1/(2*exp(-j*k(i)*Z(i))))* ...
      ((t(i+1)*exp(-j*k(i+1)*Z(i))*((eta(i+1)/eta(i))+1)) + ...
      (r(i+1)*exp(j*k(i+1)*Z(i))*(-(eta(i+1)/eta(i))+1)));
      r(i)=(1/(2*exp(j*k(i)*Z(i))))* ...
      ((t(i+1)*exp(-j*k(i+1)*Z(i))*((-eta(i+1)/eta(i))+1)) + ...
      (r(i+1)*exp(j*k(i+1)*Z(i))*((eta(i+1)/eta(i))+1)));
    end

      R = 2/(t(1)+r(1)+(eta(1)/eta0)*(t(1)-r(1))); % Normalization factor
    for i = 1:1:span(permittivity _r)
      t(i)=t(i)*R;
      r(i)=r(i)*R;
    end

% t0 and r0 are calculated from r1 and t1.
    t0 = 0.5*(t(1)*(1+eta(1)/eta0)+r(1)*(1-eta(1)/eta0));
    r0 = t(1)+r(1)-t0;
    E1 = t(1)+r(1); % The E field at boundary Z = 0
    H1 = eta(1)*(t(1)-r(1)); % The H field at boundary Z = 0

% The E and H field at boundary Z = Z(1):
    E2 = t(2)*exp(-j*k(2)*Z(1)) + r(2)*exp(j*k(2)*Z(1));
    H2 = eta(2)*t(2)*exp(-j*k(2)*Z(1)) - eta(2)*r(2)*exp(j*k(2)*Z(1));

% The E and H field of the incident field:
    Ein = t0;
    Hin = eta0*t0;

    % To find eta when there is no substrate absorption:
```

```
    % To find eta when substrate absorption is present,
    % the Poynting Vector is calculated.
    % Power at Boundary 1 - Power at Boundary 5 =
    % Absorbed power between 1 and 5
    % Absorbed power / input power = eta_prime

    eta_prime(C ) =(real(E1*conj(H1)) - real(E2*conj(H2)))/real(Ein*conj(Hin));
    % Note: eta_prime gives more accurate results
    % than eta for the test structures.

  for i = 1:span(permittivity _r2)

    permittivity 2(i) = permittivity _0*(permittivity _r2(i)-j/(w*ohm 2(i)*permittivity _0));
       % The characteristic impedance (eta) of each medium is calculated:
    eta2(i) = 1/sqrt(permeability _0/permittivity 2(i));
       % The propagation constant (k) of each medium is calculated:
    k2(i) = w*sqrt(permeability _0*permittivity 2(i));

  end

    r2 = zeros(span(permittivity _r2),1); % Reflection coeff. vector initialized
    t2 = zeros(span(permittivity _r2),1); % Transmission coeff. vector initialized

% The last boundary condition (at the mirror surface):
    r2(span(permittivity _r2)) = 0.1; % Taken arbitrarily, doesn't affect the result.
    t2(span(permittivity _r2)) = -r2(span(permittivity _r2))*exp(2*j*k2(span(permittivity _r2))* ...
    Z2(span(permittivity _r2)));

% By using a backwards iteration, t and r vectors are found:
    for i = span(permittivity _r2)-1:-1:1
       t2(i)=(1/(2*exp(-j*k2(i)*Z2(i))))* ...
       ((t2(i+1)*exp(-j*k2(i+1)*Z2(i))*((eta2(i+1)/eta2(i))+1)) + ...
       (r2(i+1)*exp(j*k2(i+1)*Z2(i))*(-(eta2(i+1)/eta2(i))+1)));
```

```
    r2(i)=(1/(2*exp(j*k2(i)*Z2(i))))* ...
    ((t2(i+1)*exp(-j*k2(i+1)*Z2(i))*((-eta2(i+1)/eta2(i))+1)) + ...
    (r2(i+1)*exp(j*k2(i+1)*Z2(i))*((eta2(i+1)/eta2(i))+1)));
  end

    R2 = 2/(t2(1)+r2(1)+(eta2(1)/eta0)*(t2(1)-r2(1))); % Normalization factor
  for i = 1:1:span(permittivity _r2)
    t2(i)=t2(i)*R2;
    r2(i)=r2(i)*R2;
  end

% t0 and r0 are calculated from r1 and t1.
  t02 = 0.5*(t2(1)*(1+eta2(1)/eta0)+r2(1)*(1-eta2(1)/eta0));
  r02 = t2(1)+r2(1)-t0;
  E12 = t2(1)+r2(1); % The E field at boundary Z = 0
  H12 = eta2(1)*(t2(1)-r2(1)); % The H field at boundary Z = 0

% The E and H field at boundary Z = Z(1):
  E22 = t2(2)*exp(-j*k2(2)*Z2(1)) + r2(2)*exp(j*k2(2)*Z2(1));
  H22 = eta2(2)*t(2)*exp(-j*k2(2)*Z2(1)) - eta2(2)*r2(2)*exp(j*k2(2)*Z2(1));

% The E and H field of the incident field:
  Ein2 = t02;
  Hin2 = eta0*t02;

  eta(C )=((abs(t0))^2-(abs(r0))^2)/((abs(t0))^2)*100;
  % To find eta when there is no substrate absorption:
  eta2(C )=((abs(t02))^2-(abs(r02))^2)/((abs(t02))^2)*100;

  eta3(C )=0.65* eta(C ) + 0.35*eta2(C );
  % To find eta when substrate absorption is present,
  % the Poynting Vector is calculated.
  % Power at Boundary 1 - Power at Boundary 5 =
```

```
    % Absorbed power between 1 and 5
    % Absorbed power / input power = eta_prime

            eta_prime2(C ) =(real(E12*conj(H12)) - real(E22*conj(H22)))/real(Ein2*conj(Hin2));
    % Note: eta_prime gives more accurate results
    % than eta for the test structures.

end % Loop ends

    Figure (1)

    %plot(h,eta,'-.r*');
    %hold on
    %plot(h,eta2,'--mo');
    %plot(h,eta2,':bs');

    plot(h,eta2,'-r', h,eta,'-.b', h,eta3,'--m')
    h = legend('Region I','Region II','Total Absorption',4);
    set(h,'Interpreter','none')

    ylabel('Absorption (%)');
    xlabel('Wavespan (um)');
    title('Absorption Spectrum for Gap Distace 2.5 um');
    grid on;
```

Appendix C- Unit conversion table between the MKS and µMKS Systems

Mechanical Conversion Factors for MKS to µMKSV

Mechanical Parameter	MKS Unit	Dimension	Multiply by This Number	To Obtain µMKSv Unit	Dimension
Length	m	m	10^{6}	µm	µm
Mass	kg	kg	1	kg	kg
Density	$kg/(m)^3$	$kg/(m)^3$	10^{-18}	$kg/(\mu m)^3$	$kg/(\mu m)^3$
Stress	Pa	$kg/(m)(s)^2$	10^{-6}	MPa	$kg/(\mu m)(s)^2$
Young's Modulus	Pa	$kg/(m)(s)^2$	10^{-6}	MPa	$kg/(\mu m)(s)^2$

Thermal Conversion Factors for MKS to µMKSV

Thermal Parameter	MKS Unit	Dimension	Multiply by This Number	To Obtain µMKSv Unit	Dimension
Conductivity	W/m . K	$(kg)(m)/(K)(s)^3$	10^{6}	pW/(µm) (K)	$(kg)(\mu m)/(K)(s)^3$
Specific Heat	J/(kg) (K)	$(m)^2/(K)(s)^2$	10^{12}	pJ/(kg) (K)	$(\mu m)^2/(K)(s)^2$
Convection Coefficient	W/m^2 . K	$kg/(s)^2$	1	$pW/(\mu m)^2$	$kg/(s)^2$

Electrical Conversion Factors for MKS to µMKSV

Electrical Parameter	MKS Unit	Dimension	Multiply by This Number	To Obtain µMKSv Unit	Dimension
Current	A	A	10^{12}	pA	pA
Voltage	V	$(kg)(m)^2/(A)(s)^3$	1	V	$(kg)(\mu m)^2/(pA)(s)^3$
Conductivity	S/m	$(A)^2(s)^3/(kg)(m)^3$	10^{6}	pS/µm	$(pA)^2(s)^3/(kg)(\mu m)^3$
Resistivity	Ω .m	$(kg)(m^3/(A)^2(s)^3$	10^{-6}	T Ω µm	$(kg)(\mu m)^3/(pA)^2(s)^3$
Permittivity	F/m	$(A)^2(s)^4/(kg)(m)^3$	10^{6}	pF/µm	$(pA)^2(s)^2/(kg)(\mu m)^3$
Energy	J	$(kg)(m)^2/(s)^2$	10^{12}	pJ	$(kg)(\mu m)^2/(s)^2$